Modeling Gamma-ray Signatures of Cosmic Ray Transport

vorgelegt von

Julien Dörner
aus Hagen STT Hohenlimburg

Bochum, January 2025

DEDICATED TO MY WIFE NELE

Acknowledgements

First of all, I want to thank my Supervisors Horst Fichtner and Julia Tjus. In all of the years working on my thesis it was never a question who is my first or second supervisor. You both distributed equally but in total different manners to the succeed of this project. Julia, you encouraged me to stick into my topic as much as possible, to get the best results and the deepest understanding. Horst, you helped me understanding the greater picture and setting my research into context and accepting to set a final point. But in all of this times you both have been a good partner for discussions not only on the scientific but also on the personal site and I am grateful for this experience.

Also I want to thank all the members of the TP 4 group who accompanied me on this journey. There are so many of you and I fear that I would forget some names if I try to list you all here. You all made the university to home in which I enjoyed to be, not only for work.

Furthermore I would like to thank my colleagues from the CRPropa developers who helped me to find my place in your group and discussed so many technical details of implementation and scientific use-cases. Without your help I would not know how to address all these questions.

Own Publications

This work is based on the following peer-reviewed articles:

- R. Alves Batista, J. Becker Tjus, **J. Dörner** et al.: *CRPropa 3.2 – an advanced framework for high-energy particle propagation in extragalactic and galactic spaces.* in Journal of Cosmology and Astroparticle Physics **09** (2022) 035

- **J. Dörner**, J. Becker Tjus, P.S. Blomenkamp, H. Fichtner, A. Franckowiak, E.M. Zaninger: *Impact of Anisotropic Cosmic-Ray Transport on the Gamma-Ray Signatures in the Galactic Center* in The Astrophysical Journal **965** (2024) 180

- **J. Dörner**, L. Morejon, K.-H. Kampert, J. Becker Tjus, *Uncertainties in astrophysical gamma-ray and neutrino fluxes from proton-proton cross-sections in the GeV to PeV range*, arXiv:2501.16967, submitted

It is stated at the beginning of a chapter or section when this part has already been published.

In addition, the following articles and conference proceedings are published by the author:

- **J. Dörner**, P. Reichherzer, L. Merten, J. Becker Tjus, H. Fichtner, M.J. Pueschel, E.G. Zweibel: *Implications of turbulence dependent diffusion on cosmic ray spectra* in Proceedings of Science (EPS-HEP 2021) 090

- P. Reichherzer, L. Merten, **J. Dörner**, J. Becker Tjus, M.J. Pueschel, E.G. Zweibel: *Regimes of cosmic-ray diffusion in Galactic turbulence* in SN Applied Sciences, volume 4, article number 15, (2022)

- **J. Dörner**, P. Reichherzer, J. Becker Tjus, V. Heesen: *Cosmic-ray electron transport in the galaxy M 51* in Astronomy & Astrophysics 669, A111 (2023)

- S. Aerdker, ..., **J. Dörner** et al.: *CRPropa 3.2: a public framework for high-energy astroparticle simulations* in Proceedings of Science (ICRC 2023) 1471

- **J. Dörner**, P. Reichherzer, J. Becker Tjus, V. Heesen: *Cosmic Ray Electron transport in the external galaxy M51* in Proceedings of Science (ICRC 2023) 231

- **J. Dörner**, J. Becker Tjus, P.S. Blomenkamp, H. Fichtner, A. Franckowiak, M.R. Hörbe, E.M. Zaninger: *Implications from 3-dimensional modeling of gamma-ray signatures in the Galactic Center* in Proceedings of Science (ICRC 2023) 584

- Further publications within the CTA collaboration.

Contents

List of Figures

List of Tables

Chapter 1

Motivation and Key Science Question

Cosmic rays (CRs) have been discovered more than a century ago. Nevertheless, the origin of these high-energetic particles is still under debate. The main difficulty in identifying the CR sources is the back-pointing of the observed CRs. The accelerated charged particles leaving the source region are deflected in the magnetic field of the Milky Way. Owing to this, substantial differences arise in the arrival direction of the CRs at Earth and the position of the accelerator in the sky. This problem is exacerbated by the turbulent component of the Milky Way's magnetic field. The diffusive motion of the particles adds a stochastic part to the arrival direction and nearly all information about heir sources gets lost.

A schematic picture of this propagation of CRs from a source to the Earth is summarized in Figure 1.1. Besides the propagation of the charged particles (blue trajectory), other non-thermal emission signatures are shown. Inside the source region, the CRs can interact with the ambient plasma and photon fields producing radiation in multiple wavelengths as well as neutrinos. One chance to identify the acceleration sites is the measurement of these secondary messengers, which are uncharged and therefore point back to their origin.

Additional to the non-thermal emission from CRs within the source region is the diffuse emission caused by interactions of CRs within the Milky Way. This radiation can be emitted when charged particles are deflected in the Galactic Magnetic Field (synchrotron radiation), scatter on the ambient photon field (e.g. Inverse Compton Scattering) or interact with the ambient gas (hadronic interaction). In this thesis we focus on the latter with an special focus on the secondary gamma rays emitted within these interactions.

As the interactions happen within the Milky Way the emission signatures are sensitive to the CR transport between the source and the point of interaction. The science in this thesis is based on the four central scientific questions:

(Q 1) How can the interactions of CR protons with the ambient gas be modeled in an efficient way?

(Q 2) Can we use diffuse gamma-ray observations to constrain the sources of CRs?
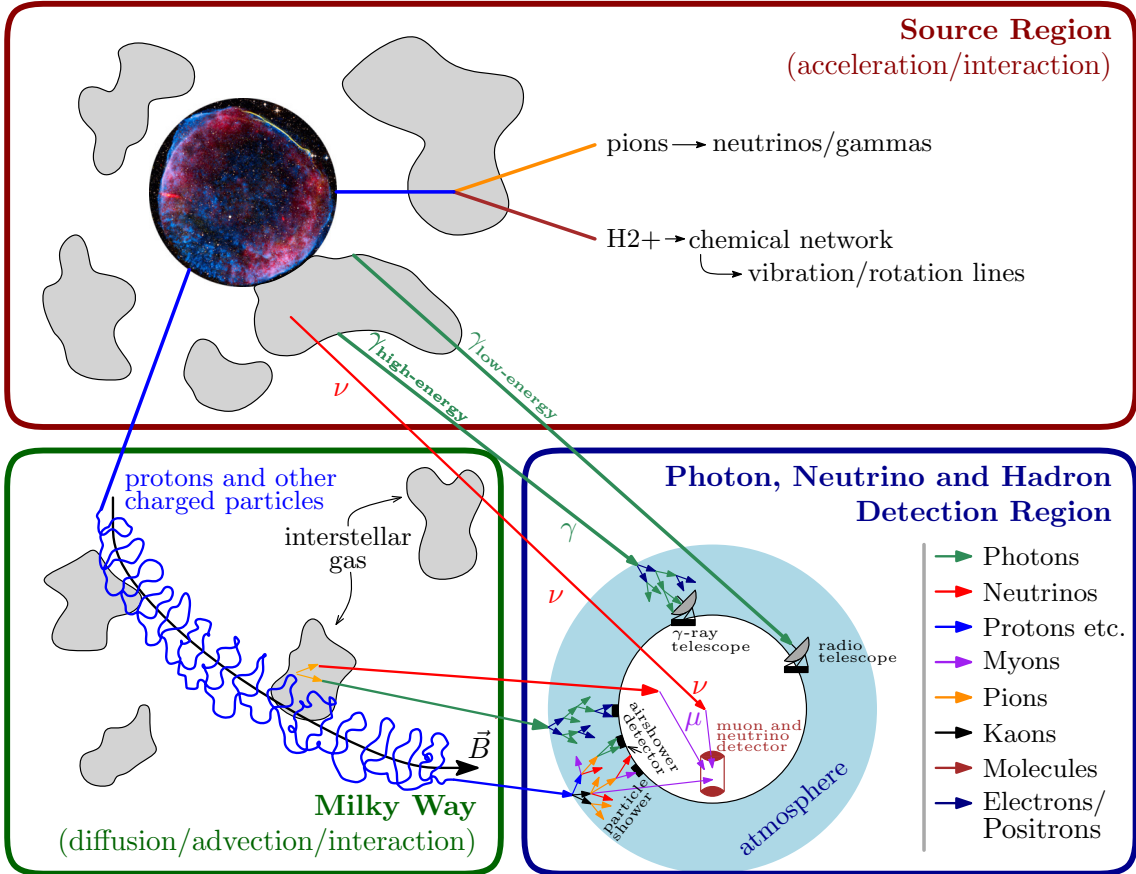
Figure 1.1. Schematic picture of the multi-messenger emission from Galactic Cosmic Rays. Figure modified after [34].

(Q 3) Which information of the CR transport properties, like the diffusion coefficient, its energy scaling or the anisotropy, can be inferred from the diffuse gamma-ray observations?

(Q 4) What is the influence of the environment (plasma density, magnetic field configuration, etc.) in which the CRs propagate on the gamma-ray signatures? Is it possible to constrain the environment from the gamma-ray observations?

To investigate this questions an introduction to the relevant theory background is given in chapter 2. Then we discuss the CRPropa framework including a new module therein to incorporate hadronic interactions in chapter 3, **Q 1**. Afterwards these interaction module is applied to the Central Molecular Zone (CMZ) of the Milky Way as a compact region close to the sources (chapter 4, **Q 2 + 3**). In the next step we follow those CRs through the Milky Way and estimate the all-sky gamma-ray emission (chapter 5, **Q 1 + 3 + 4**). And finally we follow the CRs through the heliosphere until they reach the atmosphere of the Sun and interact there (chapter 6, **Q 4**). This thesis is concluded with a final discussion in chapter 7.

Chapter 2

Cosmic Rays

The transport of Cosmic Rays (CRs) is typically described by the transport equation

$$\frac{\partial n_s}{\partial t} = \nabla\left[(\hat{\kappa}\nabla)n_s\right] - \nabla(\vec{u}\cdot n_s) + \frac{\partial}{\partial p}\left[p^2\, D_{pp}\frac{\partial}{\partial p}\left(\frac{n_s}{p^2}\right)\right] - \frac{\partial}{\partial p}\left[\dot{p}n_s - \frac{p}{3}(\nabla\vec{u})n_s\right]$$

$$+ \sum_j \frac{v_s}{c}n_0\int \mathrm{d}p'\,\sigma_{j\to s}(p,p')n_j(p') - \frac{n_s}{\tau} + Q_s(p,\vec{r},t) \tag{2.1}$$

for the differential number density n_s of the species s ($e^{\pm}$, p, He, ...). Here, the CR distribution is assumed to be isotropic in momentum-phase space. The terms on the right-hand side describe the *spatial diffusion*, described by the diffusion tensor $\hat{\kappa}$, the *spatial advection* based on the flow velocity $\vec{u}$ of the background plasma, the *momentum diffusion* described by the scalar momentum diffusion coefficient D_{pp}, the energy changes due to *continuous loss or gain* and the *momentum advection*, the *catastrophic losses* with and without the production of other CR species and the *sources and sinks* in the system, described by the source term Q_s. A detailed review of each term can be found in [34].

In the following the theory for the *spatial diffusion* is discussed in section 2.1, and for the *continuous and catastrophic energy loss* in section 2.2

2.1 Transport of Cosmic Rays in Turbulent Magnetic Fields

Magnetic fields $\vec{B}$ in astrophysical systems typically consist of ordered background component $\vec{B}_0 = \langle\vec{B}\rangle$ and a turbulent one $\delta\vec{B}$. Interactions of the CRs with these fluctuations cause scattering parallel and perpendicular to $\vec{B}_0$ leading to diffusion [116]. The power spectrum of these fluctuations determines the behavior of the diffusion tensor.

2.1.1 Astrophysical Turbulence

The origin of the magnetic fields in the universe is still under debate. Two main scenarios for their generation are discussed: The evolution of primordial fields under the influence of structure formation or the astrophysical generation [see e.g. 63].

The turbulent magnetic field is typically described as uniform and isotropic in the Galactic context. Two properties characterize it:

(i) The average magnetic field strength, expressed by the root mean square $\delta B_{\mathrm{rms}} = \sqrt{\langle \delta B^2 \rangle}$ and

(ii) The energy distribution $w(k)$ in Fourier space.

The latter is believed to follow a power-law $w(k) \sim k^{-m}$ in an 'inertial' range between the minimal and maximal wave number k_{min} and k_{max}.

Several theories have been developed to estimate the spectral index of the wave spectrum. The most prominent ones are the *Kolmogorov* [79] and the *Kraichnan* [81] turbulence predicting a slope of $m = 5/3$ and $m = 3/2$, respectively. Current observations do not show a clear preference for one model. In Figure 2.1 current data are compared to the predictions from both models. The shown lines do not represent a fit but should help the eye estimate the slope.

2.1.2 Diffusion Tensor in Quasi Linear Theory

In weakly turbulent fields ($\eta = |\delta B/B_0| \ll 1$), the diffusion coefficient parallel to the background field direction can be estimated from the scattering rate of particles $\nu_\parallel$. The scattering rate defines the characteristic time scale $\tau_\parallel = \nu_\parallel^{-1} = \lambda_\parallel/v$ and the diffusion coefficient can be expressed as [see e.g. 116]

$$D_\parallel = \frac{v^2}{2} \int_{-1}^{1} \mathrm{d}\mu \, \frac{1-\mu^2}{2\nu_\parallel} \quad , \tag{2.2}$$

where $\mu = \cos\theta$ is the cosine of the pitch-angle θ. In the quasi-linear theory (QLT) the scattering rate is approximated as [35]

$$\nu_\parallel \approx 2\pi \, \omega_g \frac{k_{\mathrm{res}} w(k_{\mathrm{res}})}{B_0^2} \quad . \tag{2.3}$$

The scattering happens for a gyration frequency $\omega_g \propto k_{\mathrm{res}}$ with the resonant fluctuation $k_{\mathrm{res}} \approx (|\mu| r_g)^{-1}$, where $r_g = E/q B_0 c$ is the gyro-radius in the ultra-relativistic limit. Using the power-law spectrum described above $w(k) \propto k^{-m}$ the parallel diffusion coefficient scales as

$$D_\parallel \propto r_g^{2-m} \eta^{-2} \quad . \tag{2.4}$$

Assuming ultra-relativistic particles and the index of the wave spectrum in the range $5/3 \leq m \leq 3/2$ one expects an energy scaling of the diffusion coefficient between $\sim E^{1/3}$ (*Kolmogorov*) and $\sim E^{1/2}$ (*Kraichnan*).

In the case of weak turbulences, the parallel diffusion ($D_\parallel$) is greater than the perpendicular one ($D_\perp$) [104]. Assuming an isotropic three-dimensional turbulence the classical scattering relation (CSR) within standard kinetic theory yields

$$\frac{D_\perp}{D_\parallel} = \frac{1}{1 + \lambda_\parallel^2/r_g^2} \quad , \tag{2.5}$$
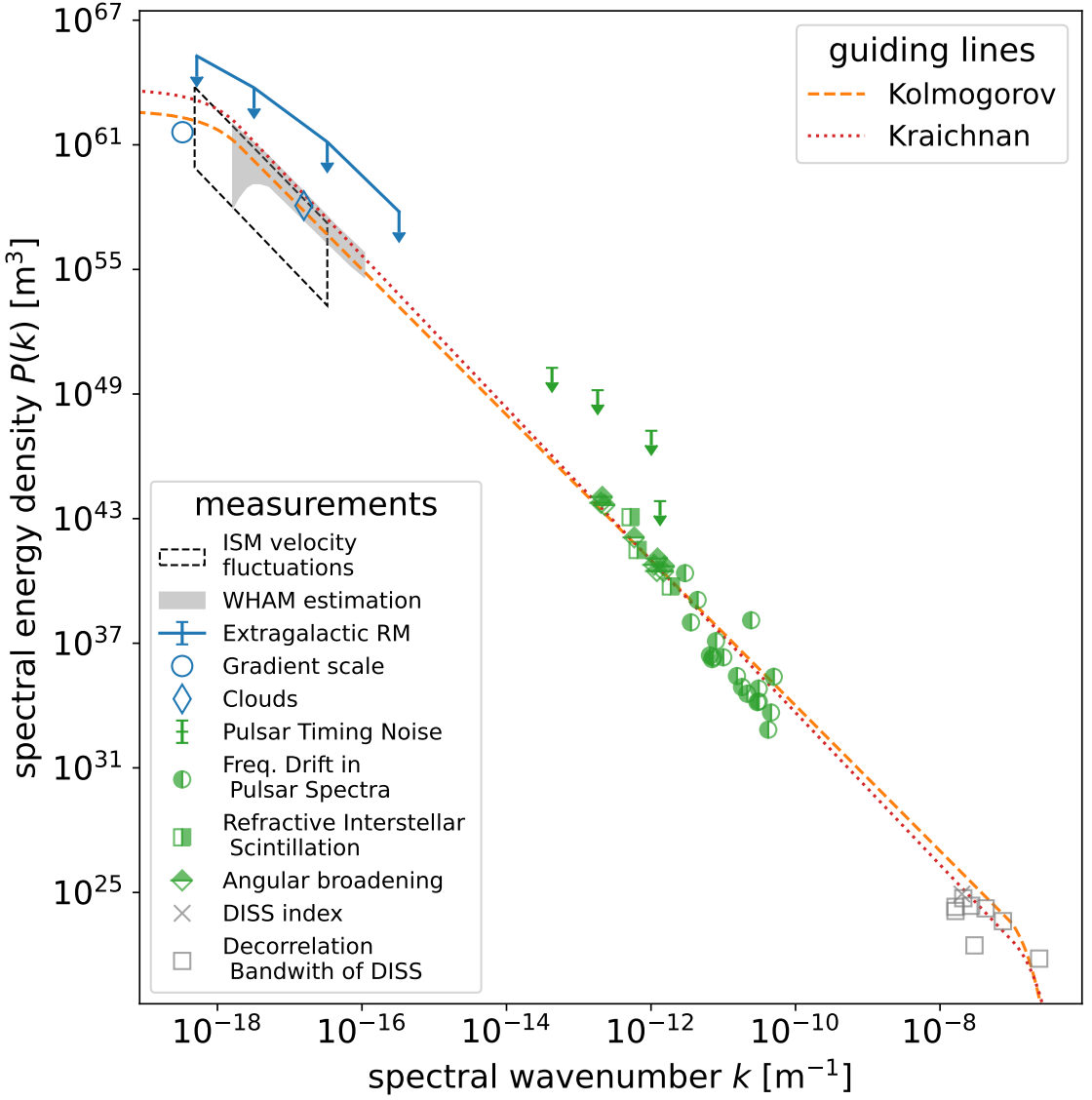
Figure 2.1. Spectrum of the energy density in magnetic fluctuations in the Milky Way. The lines for the Kolmogorov and Kraichnan spectra are simple lines to guide the eye and do not represent any fit to the data. Based on Figure 25 from [34].

where $\lambda_\parallel$ is the mean free path in parallel direction. Assuming QLT again this ratio scales with the turbulence level $D_\perp/D_\parallel \propto \eta^{-4}$ and thus the perpendicular diffusion scales as

$$D_\perp \propto r_g^{2-m} \eta^2 \quad , \tag{2.6}$$

where the energy scaling is taken from the parallel diffusion coefficient in relation 2.4.

The anisotropy of the diffusion depends on the local magnetic turbulence, which is often not known for astrophysical systems. In most cases, it is even not possible to derive a global turbulence level. Therefore, it is often useful to quantify the anisotropy of the diffusion tensor by a single value $\epsilon = D_\perp/D_\parallel$, which covers the information about the turbulence. Although this value can be position-dependent, it is assumed to be spatially constant within this work.

2.2 Energy Loss Processes for Cosmic Rays

High-energy CRs can interact with ambient gas or photon fields and lose energy in the presence of magnetic fields. Different processes are possible if one considers CR electrons (Section 2.2.1) as primaries or protons and higher nuclei (Section 2.2.2). All these interactions produce secondary emissions, which can be used to understand the nature of the underlying transport process of CRs (see e.g. [34] for a review).

2.2.1 Cosmic Ray Electrons

The main energy loss for energetic electrons and positrons is caused by synchrotron radiation (Section 2.2.1.1), inverse Compton scattering (IC, Section 2.2.1.3) and relativistic bremsstrahlung (Section 2.2.1.2).

2.2.1.1 Synchrotron Radiation

Highly energetic, charged particles, gyrate in the presence of a magnetic field. These gyrations cause the emission of low-energy photons, the so-called synchrotron radiation. The emission of a single electron $dI/d\omega$ is peaked at the critical frequency $\omega_c = 3/2\,\gamma^3 w_B (1-\mu^2)^{1/2}$, where $\gamma = E_e/(mc^2)$ is the Lorentz factor, ω_B is the gyro-frequency and $\mu = \cos\theta$ is the cosine of the pitch-angle. If one now assumes a power-law spectrum, $\mathrm{d}N_e/\mathrm{d}E_e \propto E_e^{-\alpha}$ for the CR electron distribution, the total frequency spectrum emitted due to synchrotron radiation can be approximated as

$$\left.\frac{\mathrm{d}I}{\mathrm{d}\omega}\right|_{\mathrm{tot}} \propto \omega^{-\frac{\alpha-1}{2}} \quad . \tag{2.7}$$

The index $(\alpha-1)/2$ is often called the synchrotron index.

Averaging the individual energy loss over the pitch-angle leads to the total emitted power

$$P_{\mathrm{synch}} := -\frac{\mathrm{d}E}{\mathrm{d}t} = \frac{4}{9}\frac{q^4}{m^4\,c^7}E^2 B^2 \quad , \tag{2.8}$$

where a particle with charge q is assumed. Synchrotron emission can occur for all charged particles but as the emission scales with m^4 contributions from protons are

suppressed by $(m_e/m_p)^4 \approx 10^{-13}$ for particles with the same energy. Therefore, the synchrotron energy loss for protons can be neglected in this work.

2.2.1.2 Relativistic Bremsstrahlung

In the presence of ambient matter, relativistic electrons are deflected in the electric field close to the nucleus. Due to this deflection, the so-called bremsstrahlung is emitted. This effect can happen in neutral and ionized targets. Following [113] the differential cross-section to create a photon with energy ϵ by an electron with initial energy E_i and final energy $E_f = E_i - \epsilon$ is given by

$$\frac{\mathrm{d}\sigma}{\mathrm{d}\epsilon} = \frac{\alpha r_0^2}{\epsilon E_i^2} \left[\left(E_i^2 + E_f^2 \right) \phi_1 - \frac{2}{3} E_i E_f \phi_2 \right] \quad . \tag{2.9}$$

Here, r_0 is the Bohr radius and α is the fine-structure constant. The function ϕ_i depends on the nature of the Coulomb field and is typically expressed in dependence of $\Delta = \epsilon \, mc^2/(2E_iE_f)$. For unshielded charges Ze and $\Delta > 2$, the functions become $\phi_1 = \phi_2 = Z^2 \phi_u$ with

$$\phi_u = 4 \left(\ln[1/(2\alpha\Delta)] - \frac{1}{2} \right) \quad . \tag{2.10}$$

The values for more complex scenarios can be found in [113, see table 4.1]. The largest energy loss can be found for the strong shielding case in [39]. The total emitted power follows as [113]

$$P_{\mathrm{brems}} = \frac{3.9\alpha c\sigma_T}{8\pi}\phi_1(\Delta) \left[n_{HI}(\vec{r}) + 2n_{H_2}(\vec{r}) \right] E_e \quad . \tag{2.11}$$

Here, $\sigma_T = 8\pi/3 \, r_0^2$ denotes the Thomson cross section. In contrast to the synchrotron radiation and the IC scattering the energy loss for bremsstrahlung scales linearly with the electron energy ($P \propto E_e^2$ for the other processes). Therefore, it is only expected to be relevant for lower energies.

2.2.1.3 Inverse Compton Scattering

In the presence of low-energy photon fields, the high-energy electrons can upscatter the photons. The exact energy transfer can be followed from quantum-mechanical calculations using the conservation of four-momentum. For the application in astrophysical scenarios two limits based on the dimensionless parameter

$$\Gamma = \frac{4\epsilon E_e}{m_e^2 c^4} \quad , \tag{2.12}$$

where E_e is the energy of the electron and ϵ is the energy of the low-energy photon, are discussed [34].

In the Thomson limit ($\Gamma \ll 1$) the total energy loss rate is given as

$$P_{\mathrm{IC}}^{\mathrm{Thomson}} = \frac{4}{3}\sigma_T c\beta^2\gamma^2 U_{\mathrm{ph}} \tag{2.13}$$

in a photon field with energy density U_{ph}. In the Klein-Nishina limit ($\Gamma \gg 1$) the total energy loss rate can be approximated as

$$P_{\text{IC}}^{\text{KN}} = \frac{4}{3}\sigma_T c^5 m_e^2 \int_0^\infty d\epsilon \, \frac{n_{\text{ph}}(\epsilon)}{\epsilon} \left(\ln(\Gamma) - \frac{11}{6} \right) \quad . \tag{2.14}$$

This loss rate scales with $P \propto \ln \Gamma \propto \ln E_e$.

Not only is the loss rate different in these regimes, but the maximal energy of the upscattered photons also differs. In the Thomson regime, the photon can get energies up to $E_{\text{max}}^{\text{Thomson}} = 4(E_e/(m_e c^2))^2 \epsilon_{\text{max}}$ depending on the maximal energy of the low-energy photon field ϵ_{max}. In the Klein-Nishina regime, the maximum photon energy is one-to-one the energy of the incoming energy $E_{\text{max}}^{\text{KN}} = E_{e,\text{max}}$.

2.2.2   Hadronic Cosmic Rays

Hadronic CRs like protons and higher nuclei can interact with target matter and photon fields. A high center-of-mass energy is required for the latter, which makes this interaction negligible in the Galactic context. In the following the two main channels for interaction on matter targets are discussed, the inelastic hadron-hadron interaction (section 2.2.2.1) and the ionization of neutral matter (section 2.2.2.2).

2.2.2.1   Hadronic Interactions

Hadron-Hadron interactions are believed to be the dominant source of gamma rays above several GeV [121]. These interactions produce multiple pions ($\pi^{\pm,0}$) and other mesons that subsequently decay. The neutral pions produce gamma rays ($\pi^0 \rightarrow \gamma\gamma$) while the charged pions produce electrons, positrons, and neutrinos ($\pi^+ \rightarrow e^+ \, \nu_e \, \bar{\nu}_\mu \, \nu_\mu$ and $\pi^- \rightarrow e^- \, \bar{\nu}_e \, \nu_\mu \, \bar{\nu}_\mu$).

Implementing these hadronic interactions in astrophysical modeling relies on the knowledge of cross-sections, the multiplicity of secondary species, and branching ratios. Most measurements and models for the cross-section describe the proton-proton interaction. Cross-sections for processes involving heavier nuclei are typically scaled by the mass A of the nucleus $\sigma_{A-p} = A^\alpha \, \sigma_{p-p}$.

The total inelastic cross-section has been measured at various energies (see [128] for a review). These data have been fitted by several authors [72, 73, 75]. The fit from Kafexhiu et. al. [72] matches best the data points at the highest energies. The parameterization is given by

$$\sigma_{\text{inel}}(T_p) = \left[30.7 - 0.96 \log(r) + 0.18 \log^2(r) \right] \cdot \left[1 - r^{-1.9} \right]^3 \text{ mb} \quad , \tag{2.15}$$

using $r = T_p/T_p^{\text{th}}$ and the threshold energy $T_p^{\text{th}} = 2m_\pi + m_\pi^2/2m_p \approx 0.2797$ GeV. In Figure 2.2 the comparison of the different models to the measurements compiled by the Particle Data Group [128] is given.

Besides the total inelastic cross-section, the differential one ($d\sigma/d\epsilon$, with ϵ as the energy of the secondary particle) is needed to properly model the signatures from hadronic interactions. In early works, the so-called *delta-approximation* was used to simplify the calculation. In this approximation, one assumes that all secondaries of a species are produced with the average secondary energy. In this case, the problem
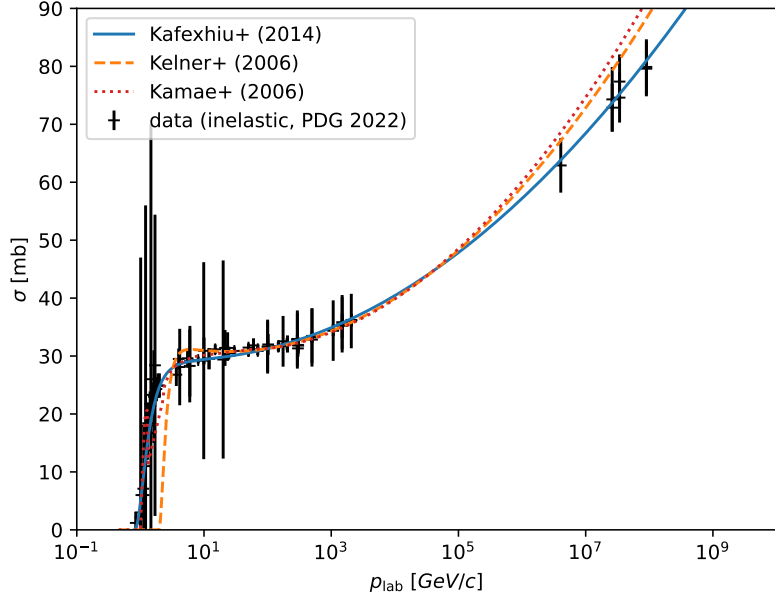
Figure 2.2. Measurement of the inelastic cross-section of the p-p interaction with theoretical models by Kamae et al. [73], Kelner et al. [75] and Kafexhiu et al. [72].

is reduced to two parameters: the average multiplicity ξ_s and the energy $\langle E_s \rangle$ (see [34] for a review). To go beyond this, several authors fitted the differential cross section as a function of the primary and secondary kinetic energy. In the following, the most frequently used distributions are discussed:

Kelner et al. (2006) This model [75] describes the spectra F_s of secondary species, s in two steps. First, the intermediate distribution of pions ($\pi^{\pm,0}$) is derived. Afterwards, the distribution of the decay products like the gamma rays, electrons[1] and the electron and muon neutrinos are calculated. For the latter, two different distributions are assumed to differentiate whether they originate from the decay of the pion or the secondary muon. It is based on simple analytical approximations, which are fitted to simulations from proton-proton interactions with SIBYLL [57]. The model is based on sampled interactions with kinetic energy T_p in the range of $0.1 - 10^5$ TeV and is fitted for the ratio between the secondary and primary energy $x = \epsilon/T_p \gtrsim 10^{-3}$.

For the lower energy extension ($T_p \leq 100$ GeV) the authors refer to the *delta-approximation*. The parameters for ξ_s and $\langle E_s \rangle$ are based on the assumption of the continuity of the spectrum at 100 GeV. Therefore, this approach can not be used in the description of a single particle interaction, as the spectral slope is not known beforehand.

Using the inelastic cross-section σ_{inel} as given in equation 2.15, the differential cross-section for the species (s) can be derived as

$$\frac{\mathrm{d}\sigma^{(s)}}{\mathrm{d}\epsilon}(T_p, \epsilon) = \frac{\sigma_{\text{inel}}(T_p)}{T_p} F_{(s)}(T_p, x) \quad . \tag{2.16}$$

---

[1]Kelner et al. assume the electron and positron distribution to be the same.

Kafexhiu et al. (2014)   In this work, the authors focus on lowering the energy boundary of the fitting approach. Here, only secondary gamma rays are accounted for. Besides the fits of Monte Carlo generators, published data are also considered for interactions with kinetic energy below 2 GeV. At the lowest energies ($T_p < 3$ GeV) the production of secondary gamma rays is dominated by resonances like the $\Delta(1232)$ baryon. They also include the decay of π^0 and η mesons. The parametrizations are fitted for a primary energy range $T_p^{\text{th}} \leq T_p \leq 1\,\text{PeV}$, starting at the kinematic threshold of the p-p interaction $T_p^{\text{th}} \approx 0.2797$ GeV.

To account for the systematic difference between Monte Carlo generators the authors provide different fit parameters for these. In this work, fit values based on the data are taken at the lowest energies ($T_p \leq 1\,\text{GeV}$), based on GEANT [20] in the intermediate energy range ($1 \leq T_p/\text{GeV} \leq 50$) and for PYTHIA 8.1 [117] in the highest energies ($T_p > 50\,\text{GeV}$).

AAfrag   This model by Kachelrieß et al. [71] is based on the Monte Carlo generator QGSJET-II-04m [98]. It is the first work, that considers not only light secondaries as electrons (e^-), positrons (e^+), gamma rays (γ), and, neutrinos (ν_e, ν_μ) but also secondary nucleons like protons (p), anti-protons ($\bar{p}$), neutrons (n) and anti-neutrons ($\bar{n}$). Additionally, the authors include the interactions between different projectiles and targets to go beyond the scaling approach for higher nuclei. The energy bound of this model is between $T_p = 5$ GeV [2] and $T_p = 10^{20}$ GeV, which also allows to investigate of the interaction of Ultra High Energy Cosmic Rays (UHECRs).

ODDK   The model by Orusa et al. investigates the fluxes of electrons and positrons [96] and gamma rays [97] from GCRs. This work is focused on all production channels that contribute to the secondary multiplicity with at least 0.5% of the total yield. The cross-sections are provided on machine-readable tables, where the secondary energy covers a range of $10^{-2} \leq \epsilon/\text{GeV} \leq 10^4$ ($\leq 10^5$ for gamma rays) and the kinetic energy of $10^{-1} \leq T_p/\text{GeV} \leq 10^6$ ($\leq 10^7$ for gamma rays). Additionally, the authors also cover helium as an alternative target and different projectiles up to ^{16}O.

2.2.2.2   Ionization

Low-energy CRs can ionize the neutral interstellar medium and trigger different chemical reactions in molecular clouds and the ionization rate of these clouds can help to learn about the underlying CR distribution. The CR protons can ionize the molecular hydrogen in different processes [99]:

$$p_{\text{CR}} + H_2 \rightarrow p_{\text{CR}} + H_2^+ + e \qquad \text{(ionization)}$$
$$p_{\text{CR}} + H_2 \rightarrow H + H_2^+ \qquad \text{(electron capture)}$$
$$p_{\text{CR}} + H_2 \rightarrow p_{\text{CR}} + H + H^+ + e \qquad \text{(dissociative ionization)}$$
$$p_{\text{CR}} + H_2 \rightarrow p_{\text{CR}} + 2H^+ + 2e \qquad \text{(double ionization)}$$

---
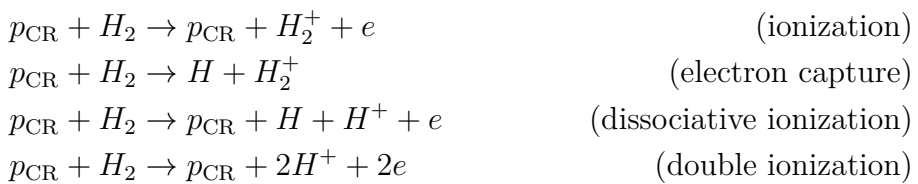
[2]This value refers to the proton case. For higher nuclei projectiles the lower energy boundary is higher to ensure the same kinetic energy per nucleon.

At energies above 100 keV, only the first process (ionization) becomes relevant and is in good agreement with the prediction from Bethe [36]. For energies above $T_0 = 49\,\mathrm{keV}$ the energy loss in ionization can be approximated as (see [113] for a review)

$$P_{\mathrm{ion}} = -\frac{\mathrm{d}T_p}{\mathrm{d}t} = 3.56 \cdot 10^{-13}\,\frac{\mathrm{eV}}{\mathrm{s}}\,\frac{m_e c^2}{\beta}\,n(\vec{r}) \begin{cases} 1 + 0.0185\ln\beta & ; \ T_p \leq 918 m_p c^2 \\ 1.315 & ; \ T_p > 918 m_p c^2 \end{cases}. \quad (2.17)$$

Here, β denotes the particle speed in units of c and $n(\vec{r}) = n_{HI} + n_{H_2}$ is the total number density of neutral hydrogen.

Chapter 3

The CRPropa Framework

The transport equation of cosmic rays in realistically modeled astrophysical environments can often not be solved analytically and a numerical description is needed. In many cases, special tools for the description of the CR transport in a specified setup have been developed, like GALPROP [103], DRAGON [52] and PICARD [76].

Section 3.1 discusses the propagation tool CRPropa [23]. Afterwards in section 3.2 the implementation of hadronic interactions (HI) into the CRPropa framework is presented. Test scenarios for the HI follow in section 3.2.3 and an application to a Giant Molecular Cloud in section 3.2.4.

3.1   CRPropa 3.2

In contrast to the above-mentioned highly specialized codes, the CRPropa framework has been developed as a general, flexible, and modular tool. The original development was focused on the transport of Ultra High Energy Cosmic Rays (UHECRs) in extragalactic space [74].

With the major version 3.0 [24], CRPropa became a modular tool, allowing customization of the physical processes involved in the simulation. This is achieved by the general structure of a `moduleList`, which is a container for all modules that are taken into account for a simulation. Most of the modules in a `moduleList` describe independent physical processes, like the deflection of charged particles in magnetic fields or interaction processes such as inverse Compton scattering, photopion production, and many others. Besides the physics modules, the `moduleList` should contain modules for the observation of particles and the boundary conditions of the simulation. Besides the modules inside the `moduleList` a CRPropa simulation requires a source, describing the particles which are simulated. Here the user has multiple options, on how to describe it. The most fundamental way is defining all starting properties of the (pseudo-)particles (the object containing the information is called `Candidate` in CRPropa) and collecting them in a so-called `CandidateVector`. In principle, the simulation can also be run with a single `Candidate`, which might be useful for testing purposes. The workflow of this process is shown in Figure 3.1.
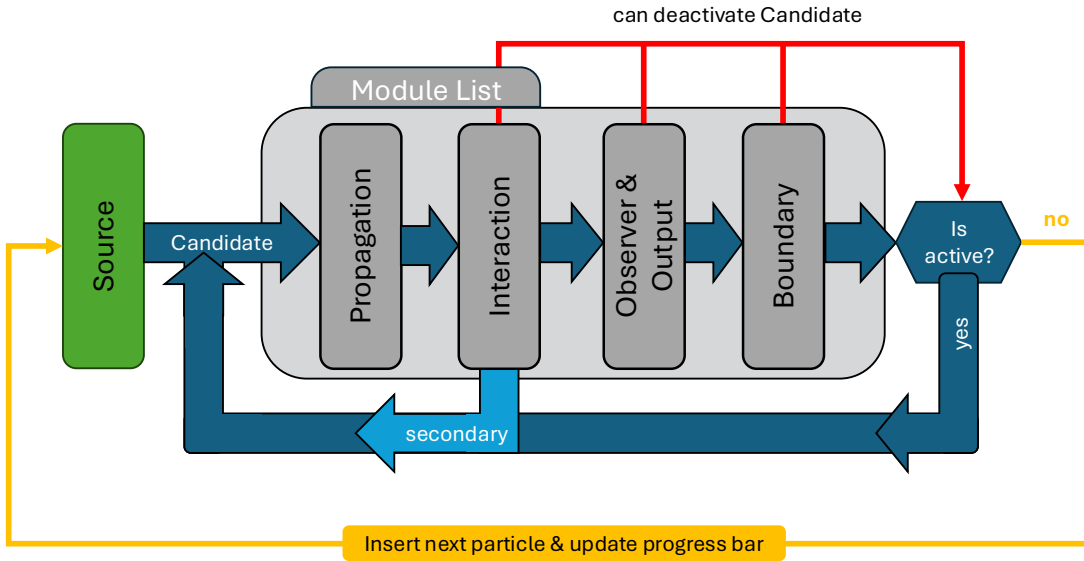
Figure 3.1. Schematic view of the process chain in a CRPropa simulation. The grey box describes the `moduleList`, which contains all physical modules as well as the boundary conditions and the observer. `Candidates` are injected by the source and iterated through the `moduleList` as long as they are active.

3.1.1   Propagation

In version 3.0 CRPropa describes the movement of particles by the deflection from magnetic fields. The code offers a set of different possibilities to describe these magnetic fields, covering general field types (uniform, grid-based, turbulent). The deflection is integrated length steps ds. Where the change of unit direction $\vec{u} = \vec{v}/|\vec{v}|$ can be written as

$$\frac{d\vec{u}}{dt} = \frac{q\,c^2}{E}\left(\vec{u} \times \vec{B}\right) \tag{3.1}$$

given the charge q, Energy E and the magnetic field $\vec{B}$ at the position of the particle. The integration can be done using the Cash-Karp algorithm [43] or Boris Push method [41] (since version 3.2 [23]). In astrophysical systems large scale electric fields can not exist and are therefore not implemented in CRPropa.

In version 3.1 [88] an additional way to describe the motion of pseudo-particles was introduced. Based on the method of Stochastic Differential Equations (SDEs) the diffusive motion can be described. In this case the transport equation [see e.g. 34]

$$\frac{\partial}{\partial t}n = \nabla\left(\hat{\kappa}\nabla n - \vec{u}n\right) + \frac{\partial}{\partial p}\left[p^2 D_{pp}\frac{\partial}{\partial p}\left(\frac{n}{p^2}\right) + \frac{p}{3}(\nabla\vec{u})n\right] + Q(\vec{r}, p, t) \tag{3.2}$$

for the differential particle number density $n = n(\vec{r}, p, t)$ is solved. Here, $\hat{\kappa}$ is the spatial diffusion tensor, $\vec{u}$ is the advection velocity, D_{pp} is the momentum diffusion coefficient, and Q describes the sources and sinks.

3.1.2 Observer and Output

The CRPropa framework allows the user to choose different types of observations and outputs for the simulated `Candidates` .

First, the `Oberserver` is used to decide in each loop of the `ModuleList` if a `Candidate` is output or not. For this decision, a list of `ObserverFeatures` can be used in the observer module. The most used ones in this work are

(1) the `ObserverSurface` , which defines a surface like a sphere or a rectangular box, and all particles crossing the surface are detected.

(2) the `ObserverTimeEvolution` , which detects all particles at a given simulation time. This feature allows for multiple detection at different times, to trace the temporal evolution of the CR distribution. In this case, the user has to set the flag `Observer.SetDeactivateOnDetection(False)` , to prevent deactivating the `Candidate` after the first detection.

(3) the `ObserverDetectAll` , which detects all particles at any time. This feature should only be used in combination with different veto options of the observer, to only detect some secondary species, or on a limited number of particles, for which the full trajectories should be followed. Otherwise the total output can easily reach several Petabyte for a realistic simulation.

After the decision on a detection, the `Candidate` is given to the output module. CRPropa offers the output in three different data formats: (1) directly streamed to the standard output, which is the terminal in most cases, (2) a plain text file, and (3) an HDF5 binary format. In all output modules, the user can decide which properties of the `Candidate` are stored. This is an important way to reduce the total memory output.

3.1.3 Boundary and Break Conditions

Boundary conditions are needed in any kind of CRPropa simulation to restrict the simulation volume or ensure the desired energy range. Without any boundary condition a CRPropa simulation would run into an infinite loop. CRPropa allows for various boundary conditions. The user can decide between a periodic or reflective repetition of the simulation volume, to mimic an infinite volume, or a free escape boundary, where all particles reaching it are lost. Here, a spherical, an ellipsoidal, a cylindrical, and a cubic boundary are available, but the user can extend it by custom shapes.

Besides the restriction of the simulation volume, a set of different break conditions is provided in the package. These can be used for a maximum trajectory length (or maximum residence time) of the particles or restrict the minimum energy, rigidity, or redshift for different particle types.

3.1.4 Interactions

In CRPropa various interaction processes are implemented. Figure 3.2 summarized these processes based on the primary particle, which is interacting. The neutrinos
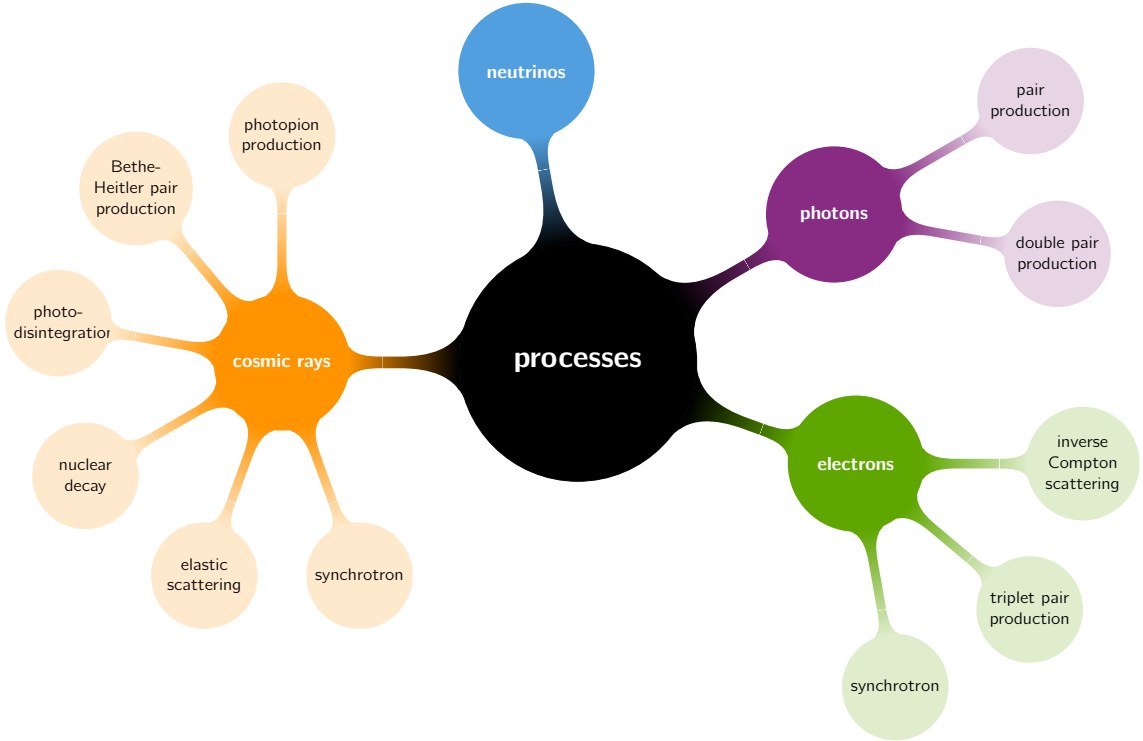
Figure 3.2. Interaction processes implemented in CRPropa 3.2. Figure taken from [23].

have no interaction channel, and therefore, only propagate on straight lines. The synchrotron radiation is implemented for both electrons and hadronic CRs (called cosmic rays in the figure) and depends on the provided magnetic field. Beside the nuclear decay of CR nuclei, all other processes describe the interaction with an photon field. The photon fields available cover the Cosmic Microwave Background (CMB) and several models for the extragalactic background light (EBL) and the Universal Radio Background (URB). Additional photonfields (like the interstellar radiation field of the Milky Way) can be implemented by the user[1]. All secondary particles that are created in these interactions can be followed on.

In the current public version CRPropa misses all interaction channels with the ambient matter. In the next section the implementation of the inelastic interactions is presented. In future work the implementation of relativistic bremsstrahlung and ionization losses for CR electrons and protons will become necessary.

3.2   Implementing Hadronic Interaction

Parts of the following chapter are based on the work:
    J. Dörner *et al.* (2025), arXiv:2501.16967, submitted, [49]

---

[1]A detailed description about the implementation has been developed in the scope of this work and can be found at https://crpropa.github.io/CRPropa3/pages/example_notebooks/custom_photonfield/custom-photon-field.html

The implementation of hadronic interactions into the CRPropa framework is based on the plug-in template[2]. This allows the implementation of additional modules in C++ and the same Python steering of the simulation as CRPropa. The final plug-in will become publicly available.

3.2.1 Pre-calculation of Data

Monte Carlo codes like CRPropa need a description of the energy distribution of the secondaries of each interaction. In the case of the Hadronic Interaction, this quantity can be derived from the differential inclusive cross-section. In this work, the models summarised in section 2.2.2.1 are implemented. Drawing secondaries from a distribution (probability distribution function, PDF) is often done with the Monte-Carlo rejection sampling or the inverse CDF (cumulative distribution function) sampling.

The rejection sampling randomly chooses points in a predefined area. All points that are above the PDF function are rejected, the other points are accepted. In Figure 3.3 an illustration of the rejection sampling is given. Here 300 random points are shown in the pre-defined sample area (black square). The PDF which should be reproduced by the sampling is shown in blue. The points in the red area above the curve (red crosses) will be rejected. Only the points in the green area (green circles) are accepted. This method leads to a high fraction of attempts that do not belong to the distribution function. The fraction can be calculated as

$$
f_{\text{accept}} = \frac{\int\limits_a^b \text{PDF}(x) \, \mathrm{d}x}{(b-a) \max\limits_{x \in [a,b]} \text{PDF}(x)} \quad , \tag{3.3}
$$

where $a \leq x \leq b$ denotes the sample range. In the example of Figure 3.3, this leads to an acceptance of 64.1 %. In the application of the energy distribution of secondaries, this fraction can go down to sub percent level, as the distribution function is often a power law, but the sampling of the points is done linearly. Therefore, this method would require too much computation time.

The alternative method is the inverse CDF sampling. Here the cumulative distribution function

$$
\text{CDF}(x) = \int\limits_{-\infty}^x \text{PDF}(x') \, \mathrm{d}x' \tag{3.4}
$$

is used. For the sampling method, this CDF has to be inverted, but as this is not possible analytically for all secondary distributions, a tabulated CDF function is used. As this table is strictly increasing, it can be easily inverted. By choosing a random value of the CDF y and applying the inverted CDF table, the bin, and the corresponding bin edges $x_0 \leq \text{CDF}^{-1}(y) \leq x_1$ can be estimated. In the second step, the position in the bin is chosen randomly.

In the case of the secondary energy of the particles a two-dimensional CDF table, depending on the primary kinetic energy T_p and the secondary energy ϵ is calculated

---

[2]`https://github.com/CRPropa/CRPropa3/tree/master/plugin-template`
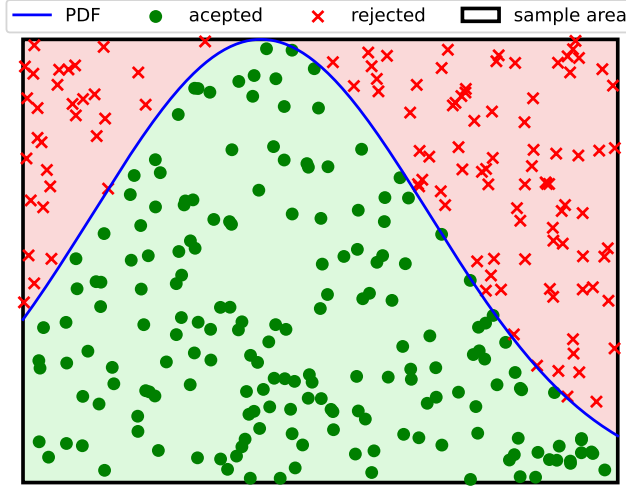
Figure 3.3. Illustration of the rejection sampling method. 300 points are randomly
chosen in the sampling area (black rectangle) and compared to the PDF function
(blue line). All points below the PDF line are accepted to be part of the distribution
(green circles). The other points are rejected (red crosses).

as

$$\text{CDF}(T_p, \epsilon) = \int\limits_0^\epsilon \frac{\mathrm{d}\sigma}{\mathrm{d}\epsilon}(T_p, \epsilon') \, \mathrm{d}\epsilon' \quad . \tag{3.5}$$

For all models described in section 2.2.2.1 and all secondary species a table is pre-
calculated, using a resolution of 25 (15) bins per decade in kinetic primary (sec-
ondary) energy T_p (ϵ) in the range 10^{-2} GeV $\leq T_p, \epsilon \leq 10^{10}$ GeV [3].

3.2.2   Runtime Calculation

The main design of the module is analogous to the existing interaction modules in
CPRropa. The computation is split into two main functions. The `process` function
is called in every propagation step. Its main purpose is to decide if an interaction
should happen in this step or not. Therefore, the interaction probability

$$p = n_{\text{nucl}}(\vec{r}) \, \sigma_{\text{inel}}(T_p) \, \Delta s \tag{3.6}$$

is calculated, based on the total inelastic cross section σ_{inel}, the current step length
Δs and the nucleon density $n_{\text{nucl}} = n_{\text{HI}} + n_{\text{HII}} + 2n_{\text{H}_2}$ at the current position of the
`Candidate`. In this model the parametrization by Kafexhiu *et al.* [72] is used. The
gas density can be chosen by the user. A large variety of models for the Galactic
diffuse gas is already implemented in CRPropa and other models for the gas density
can easily be added.

This calculation of the probability is only valid for small steps. The first limita-
tion, requiring a small step is density fluctuation. The module assumes no density

---

[3]Not all of the models described in section 2.2.2.1 cover the full energy range. The user of the
plug-in has to ensure that models are only applied in the covered energy ranges.
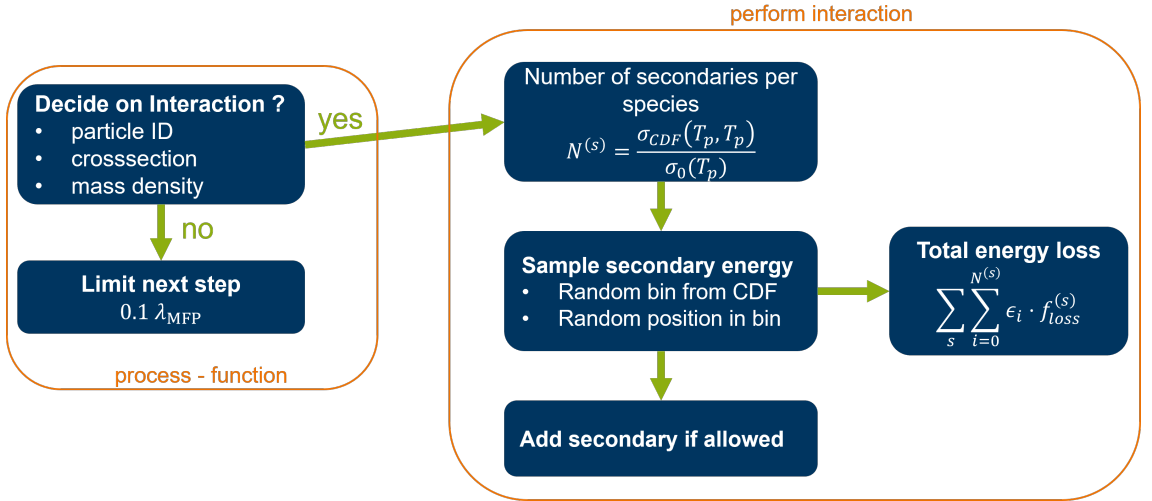
Figure 3.4. Workflow design for the hadronic interaction module.

changes along the propagation step. Therefore, the user has to ensure steps that are smaller than the changes in the density. The second limitation of the step length is the linear approximation of the optical depth $\tau = n\sigma_{\text{inel}}l$. The probability of a particle interacting within the length $l = \Delta s$ is given by

$$p = 1 - \exp\{-\tau\} \approx \tau + \mathcal{O}(\tau^2) \quad , \tag{3.7}$$

where the last approximation results in an error [4] of less than 5% for $\tau \leq 0.1$. The module automatically limits the propagation step to $\tau = 0.1$, but this value can be changed by the user. The decision if an interaction is happening in the step is done by drawing a random probability $p_0 \in [0, 1]$ from the CRPropa in-build random number generator (RNG). If the drawn probability is lower than the calculated interaction probability the interaction will occur. If not, the length of the next propagation step will be limited and the `process` function ends.

The interaction itself is computed in the `performInteraction` function. This separation into two parts of the code allows easier testing of the interactions without spending computation time on the propagation and decision of an interaction. The separation into the two functions and the main steps in each function call is summarized in Figure 3.4.

The calculation of the `performInteraction` function is looped over all secondary species (s), which are included. In most cases, this corresponds to $s = \gamma, \nu_e, \nu_\mu, e^\pm$, but also secondary (anti-) nucleons are included in some models. For each species the total number of secondaries $N^{(s)}$ is calculated as

$$N^{(s)} = \int_{T_{p,th}}^{T_p} \frac{1}{\sigma_{\text{inel}}(T_p)} \frac{d\sigma}{d\epsilon}(T_p, \epsilon) \, d\epsilon = \frac{\text{CDF}(T_p, T_p)}{\sigma_{\text{inel}}(T_p)} \quad , \tag{3.8}$$

---

[4]The error δp of the first-order Taylor Series can be estimated by the Lagrange error bound. In this case, it holds $\delta p \leq 0.5p$. It should be noted, that the Lagrange error bound describes the worst-case scenario for the Taylor approximation [78].

where in the last step the precalculated CDF table is used. Knowing the total number of secondaries, the energies of these are sampled from the CDF table, as described in the section before. For each secondary species, the user has the choice to add the sampled secondaries into the simulation, allowing those secondaries to travel further and trigger other interactions.

To calculate the total energy loss of the primary particle the energies of all secondaries are summed up, and multiplied by a correction factor $f_{\text{loss}}^{(s)}$. This factor can be set by the user to take missing secondary species into account. As one example, the ODDK model [96, 97] can be mentioned. This model only contains secondary gamma rays (γ) and leptons ($e^\pm$), while no description for the production of neutrinos is provided. Here the user can decide to combine the ODDK tables with the neutrino description from other models or set an energy loss correction factor. The default behavior is, multiplying the energy loss of the leptons by 4, using the ratio 1 : 3 between leptons and neutrinos in the decay of charged pions. While the ODDK model also includes secondaries from other channels than pions, this approximation for the energy loss is dominated by the pions. The accuracy of this energy loss can be seen in section 3.2.3.3. This correction factor is only applicable to the total energy loss of the primary but does not allow to compute the flux of secondary neutrinos. If the user is interested in this, a different description of the inclusive differential cross-section has to be used.

3.2.3   Test Scenarios for Hadronic Interactions

In this section a collection of tests for the mean free path (section 3.2.3.1), the secondary yields (section 3.2.3.2), and the total energy loss of the primary (section 3.2.3.3) is given. In the application to an astrophysical source (section 3.2.4), the impact of the choice of different models for the differential cross-section is shown.

3.2.3.1   Testing the Mean Free Path

The first test considers the mean free path (MFP) of the CRs in a background gas with a constant density $n_{HI} = 10^8$ m^{-3}. In this case the MFP can be calculated as $\lambda_{\text{mfp}} = (n_{HI}\,\sigma_{\text{inel}})^{-1}$. To test the MFP 10^4 protons are propagated in steps of 100 pc until the first interaction happens, and the average distance is computed. The result is shown in Figure 3.5. The minor differences between the predicted MFP and the sampled one are based on the Monte-Carlo nature of the module.

3.2.3.2   Testing the Secondary Yield

The second step of testing the module is the yield of secondaries in the interaction. At this point only the results for the test using the AAfrag [71] model of the cross-section are shown. The same kind of test has been performed for all models and the agreement is on the same level. Results from the other models are presented in the appendix of [49].

The test for the secondary yield is performed at four different primary energies $T_p \in \{10^1, 10^3, 10^5, 10^7\}$ GeV. At each energy, the secondaries of 500 interactions
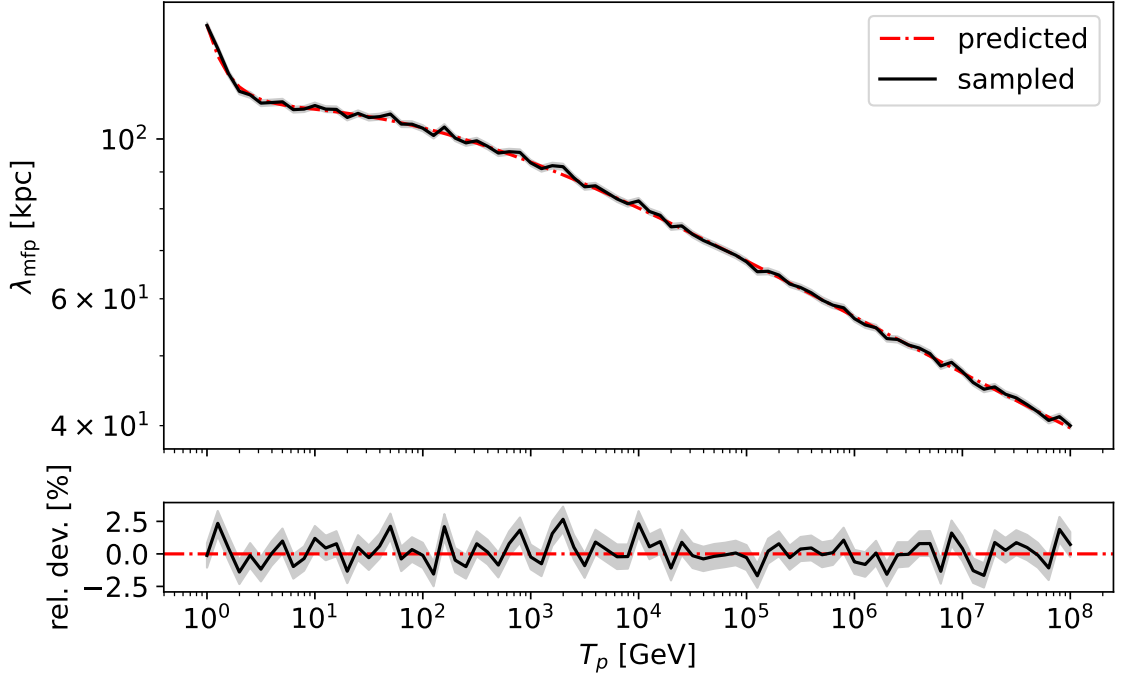
Figure 3.5. Comparing the analytical MFP with the average propagation distance to the first interaction.

are collected and the spectral energy distribution (SED) is computed and shown in Figure 3.6. Additionally the expected yield from the differential cross-section

$$\frac{\mathrm{d}N}{\mathrm{d}E_{\text{sec}}} = \frac{1}{\sigma_{\text{inel}}} \frac{\mathrm{d}\sigma}{\mathrm{d}\epsilon} \tag{3.9}$$

is shown as a line. At this point, the focus is on the spectral shape and not the overall normalization of the curve. Therefore the prediction line is normalized to the sampled data at $E_{\text{sec}} = 0.01 T_p$, indicated by the dotted grey line in Figure 3.6.

For $T_p = 10\,\text{GeV}$ the statistical fluctuations are the strongest. This is expected as the total multiplicity increases with the kinetic energy of the primary and the uncertainty scales with $\propto N^{-0.5}$. Nevertheless, the spectral shape is in good agreement with the prediction. Only at the highest energies ($E_{\text{sec}} \sim T_p$) the sampled data are missing. This can be explained by the low statistics of this test and the relative rareness of those events.

In the higher energies ($T_p \geq 10^3\,\text{GeV}$) the statistical fluctuations become less significant. Also, the agreement at the highest energies is better due to the higher total multiplicity of the secondaries. Overall this test shows the good reproduction of the expected secondary yield and validates the choices of resolution for the CDF tables.
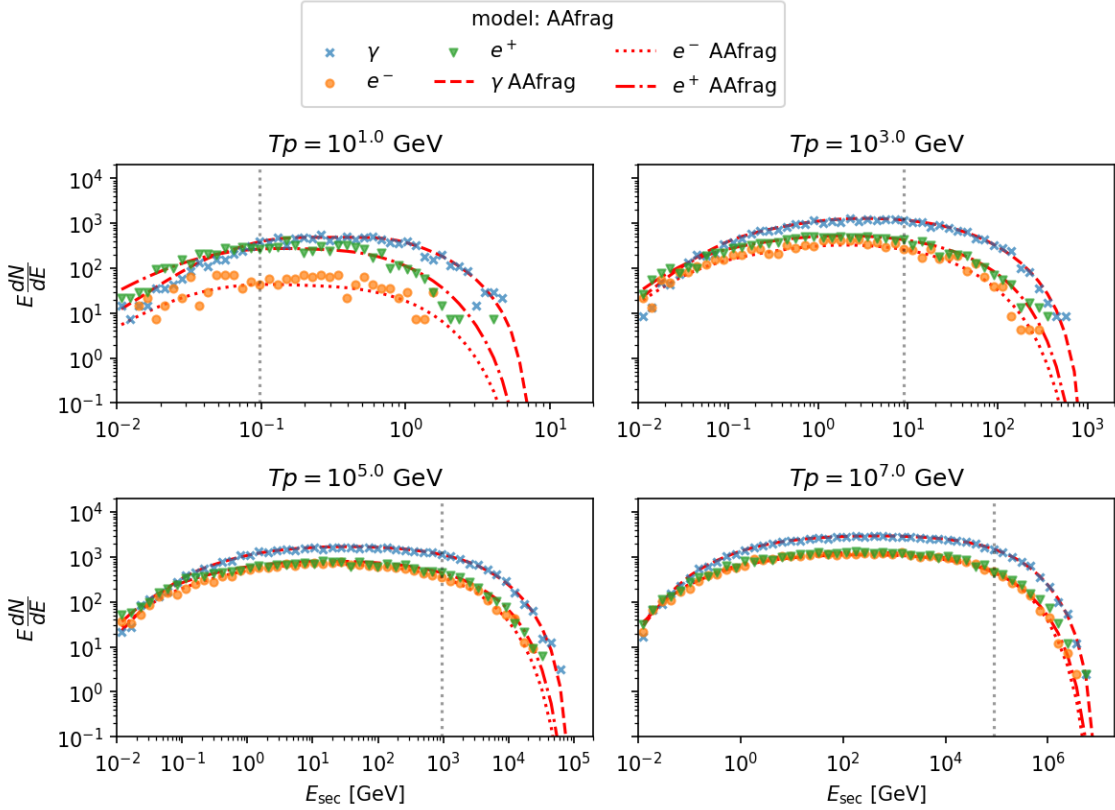
Figure 3.6. Secondary yields using the AAfrag model [71] for the inclusive cross section. The prediction from the model is normed at $E_{\mathrm{sec}} = 0.01T_p$ to the sampled data.

3.2.3.3   Testing the Energy Loss

The final test is the average energy loss in one interaction. For a given differential cross section $\mathrm{d}\sigma/\mathrm{d}\epsilon$ the total energy loss per time can be calculated as [82]

$$-\frac{\mathrm{d}E}{\mathrm{d}t} = \sum_s \int_0^{T_p} \mathrm{d}\epsilon\, v\epsilon n\frac{\mathrm{d}\sigma_s}{\mathrm{d}\epsilon}(T_p, \epsilon) \quad , \tag{3.10}$$

using the velocity v of the primary and the target density n.

In the case of the production of pions from the Kelner model [75], Krakau and Schlickeiser [82] followed an analytical approximation for the total energy loss

$$\frac{\mathrm{d}E}{\mathrm{d}t} \approx -3.85 \cdot 10^{-16}\, \frac{n}{1\,\mathrm{cm}^{-3}}\, E_{\mathrm{GeV}}^{1.28} + (E_{\mathrm{GeV}} + 200)^{-0.2}\, \frac{\mathrm{GeV}}{\mathrm{s}} \tag{3.11}$$

where E_{GeV} is the energy in GeV units. In this test, this approximation is used as a baseline scenario for comparison.

The energy loss is tested in a homogeneous density with $n_{HI} = 10^8\,\mathrm{m}^{-3}$. For each kinetic primary energy T_p $N_{\mathrm{sim}} = 10^6$ particles are propagated for one step with $\Delta s = 0.01\lambda_{\mathrm{mfp}}$. The small step size, compared to the mean free path, is used to ensure the first-order approximation of the module. Here, only one step is used,

as multiple steps would allow multiple interactions at different kinetic energies. In this case, the sampled energy loss would be an integrated quantity over the energy losses. The module is tested for the cross section models Kelner [75], AAfrag [71], ODDK [96, 97] and Kafexhiu [72]. The AAfrag model is tested in two ways. Once the full model is used including all secondary species included by the authors. In the other case, only light particles (γ, $e^\pm$, ν) are included. This model is more similar to the others as they do not include secondary nucleons. In the ODDK model a correction factor $f_{\text{loss}}^{e^\pm} = 4$ for the electrons and positrons is used. This factor corrects the missing energy loss into neutrinos as they are not included in the model. The model by Kafexhiu et al. only contains secondary gamma rays. As the ratio between the energy loss into gamma rays and other particles is not constant in energy, the application of an energy loss correction factor is not possible. Therefore, the total energy loss is not expected to be reproduced correctly.

In Figure 3.7 the energy loss timescale $\tau_{\text{loss}} = E/|\mathrm{d}E/\mathrm{d}t|$ is shown. The sampled data from the module is shown as scatter points. The approximation from Krakau and Schlickeiser (eq. 3.11) is shown as a solid black line. The sampled loss time from the Kelner model (blue cross) agrees well with the prediction, as they are both followed by the same parametrization. The prediction covers a larger energy range, as they can use the delta approximation at lower energies, which is impossible for single-particle interactions. Here only the energies with $T_p > 100\,\text{GeV}$ are shown. The energy loss time in the ODDK model agrees with the approximation, but in the lowest energies strong fluctuations, due to the energy loss scaling factor $f_{\text{loss}}^{e^\pm}$, are visible. The loss timescale in the Kafexhiu model is much larger than all other models, as it only contains secondary gamma rays, and therefore a significant fraction of the total energy loss is missing. The AAfrag model is in agreement with the approximation for the higher energies ($E > 10^2\,\text{GeV}$) but for the lower energies the timescale is shorter, meaning a more efficient energy loss. This shows the impact of secondary nucleons, which are only included in this model. The impact of these nucleons can also be seen by comparing the AAfrag loss times with the *AAfragLight* model, which neglects the secondary nucleons. In this case, the total timescale is higher in the high energy regime and the difference becomes larger at the lower energies.

Additionally to the comparison with the approximation by Krakau and Schlickeiser, the sampled energy loss timescale can be compared directly to the expected energy loss following equation (3.10). The relative difference between sampled and calculated energy loss is shown in Figure 3.8. The models Kelner and ODDK are only shown for the energy ranges covered by the authors. The agreement in the Kelner model is the best. Here the difference is less than 10 %. In the AAfrag model using only light secondaries (green triangle) the agreement at the higher energies ($T_p > 50\,\text{GeV}$) is in the same order as for the Kelner model. At lower energies, the test is dominated by single interactions as the cross-section is quite low. Therefore a stronger fluctuation is expected. The full AAfrag model shows higher deviations as more particle species are included. Especially the nucleons have a low cross section and are only sampled in rare cases[5]. In all of these four nucleon channels (p, $\bar{p}$, n, $\bar{n}$) a discrete number of secondaries is sampled. This causes the jumps in the sampled

---

[5]The average multiplicity for a proton at $T_p = 10^3\,\text{GeV}$ is $N \approx 0.14$.
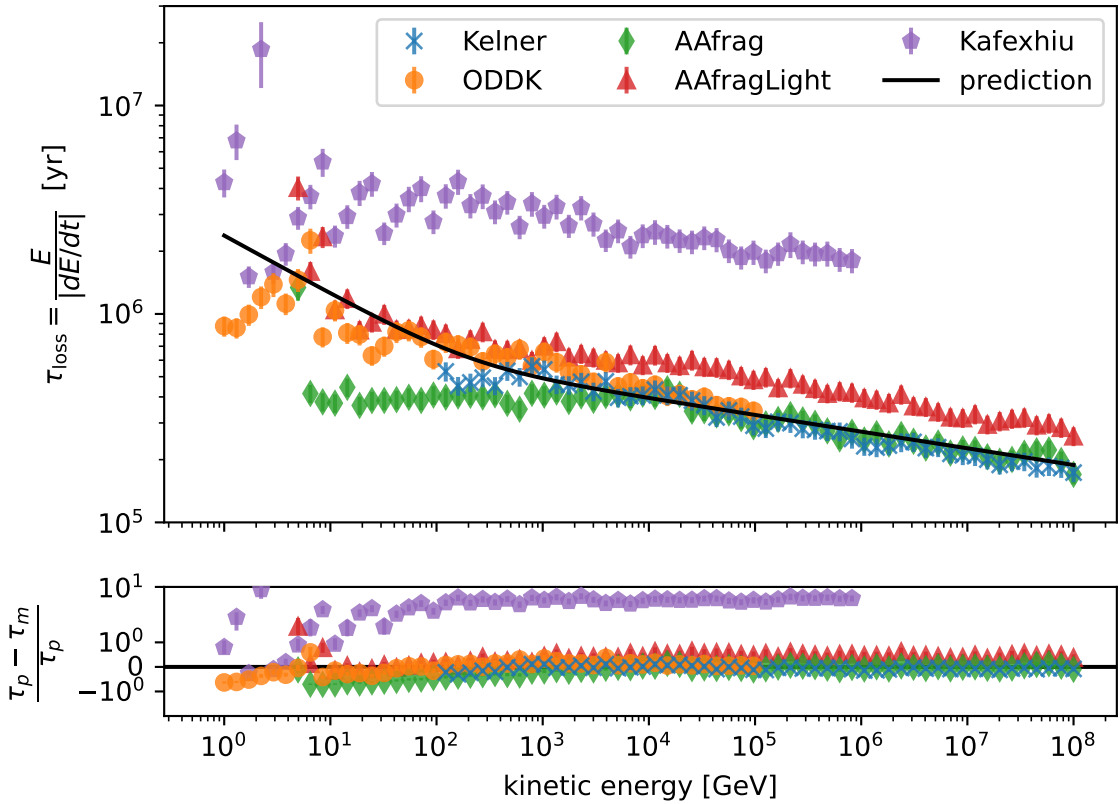
Figure 3.7. Sampled energy loss time for different models of the differential cross-section. The errorbars showing the statistical uncertainty $\sim \sqrt{n}$, are in most cases smaller than the marker size. The lower panel shows the relative deviation between the prediction τ_p from [82] and the sampled loss time in the modules τ_m.

energy loss and the slight underestimation of the total energy loss corresponding to a larger loss timescale. The ODDK model (red circle) has stronger fluctuations compared to the Kelner model, but this is somehow expected, as the correction factor is used, which also increases the statistical uncertainties. However no general trend can be observed, and the usage of a correction factor seems valid. Although the Kafexhiu model shows a significantly lower energy loss (see Figure 3.7) the relative deviation (see Figure 3.8) agrees well. The fluctuation in this model is higher compared to those with more secondary species, as the total number of secondaries in one interaction becomes less. But the overall error is less than 20 % in an acceptable range.

All tests of the absolute energy loss per unit time and the relative difference to the analytical prediction show a good agreement. In all cases, the relative error is below 20 % and in most astrophysical applications the uncertainty on the other input parameters is much higher. Nevertheless one has to notice that the energy loss can not be explained by the Kafexhiu model alone. To use this model in a real application, it should be combined with other secondary species from other models, which can be done easily using the CRPropa module.
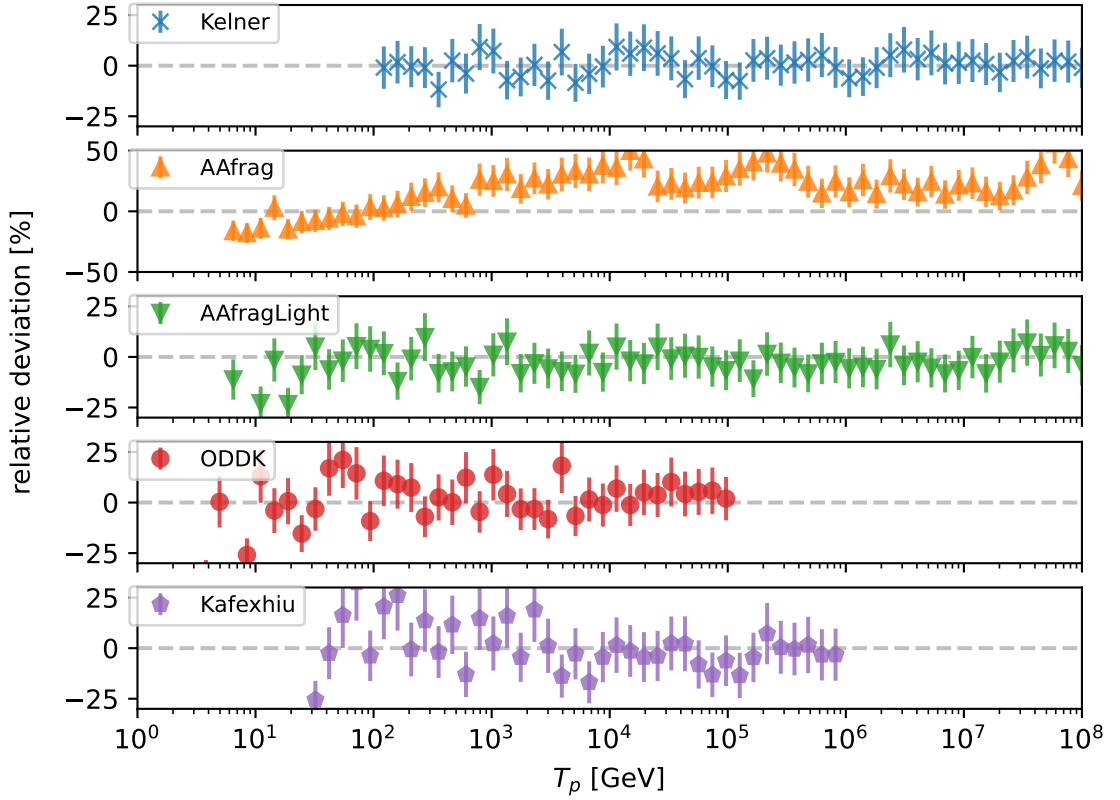
Figure 3.8. Relative difference between the sampled energy loss timescale and the analytical prediction $\tau = E/(\mathrm{d}E/\mathrm{d}t)$. The energy loss is calculated following equation (3.10). Data are only shown in the applicable energy ranges of the model.

3.2.4 Application to a Local Giant Molecular Cloud

In this section the gamma-ray emission from a simplified giant molecular cloud (GMC) is investigated, to illustrate the capability of the module and the impact on the choice of a hadronic interaction model. The cloud is modeled as a sphere with a given radius $R_{\mathrm{GMC}} = 10\,\mathrm{pc}$ and a density profile

$$n(r) = \frac{10^3\,\mathrm{cm}^{-3}}{1 + \frac{r}{0.5\,\mathrm{pc}}} \quad . \tag{3.12}$$

The resulting profile is shown in Figure 3.9.

3.2.4.1 Simulation Setup

CRs from the Local Interstellar Spectrum (LIS) are propagated from the surface of the cloud into it. Here $N_{\mathrm{sim}} = 10^8$ protons are simulated for each hadronic interaction model. The propagation is done on straight lines using the `SimplePropagation` module from CRPropa to simplify the analysis and neglect effects from the diffusion of CRs inside the cloud. The simulation is performed with a flat energy distribution ($\mathrm{d}N/\mathrm{d}\log(E) = const.$) in the range between $10^{-1}\,\mathrm{GeV}$ and $10^7\,\mathrm{GeV}$.
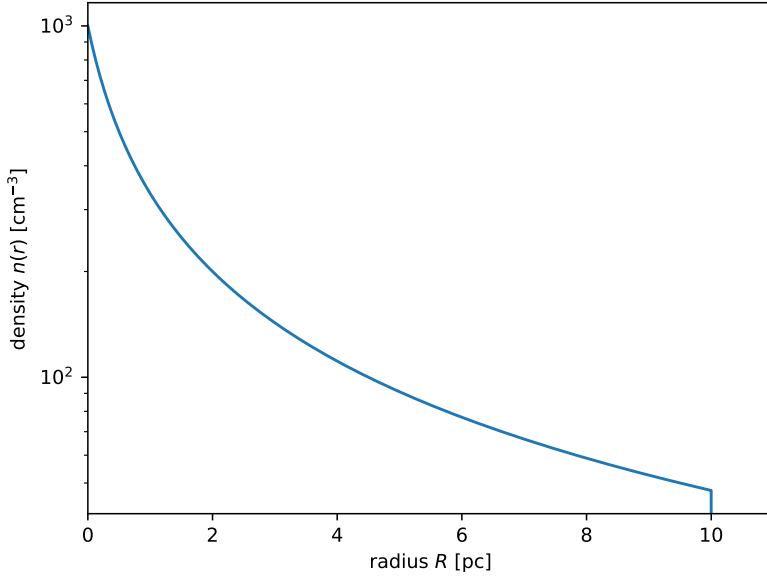
Figure 3.9. Density profile of the simplified GMC.

After the simulation, the detected gamma rays are reweighted to the LIS by assigning a weight

$$w_i = \frac{j_p(E_0)}{E_0^{-1} \, N_{\text{sim}}} \tag{3.13}$$

to each `Candidate`, where E_0 is the particle energy at the source and j_p is the LIS for protons parametrized as

$$j_p(E_p) = 2.7 \, E_p^{1.12} \, \beta^{-2} \left(\frac{E_p + 0.67}{1.67} \right)^{-3.93} \left[10^{-3}/(\text{GeV} \, \text{m}^2 \, \text{s} \, \text{sr}) \right] , \tag{3.14}$$

where E_p is the proton energy in GeV. The detailed simulation setup and used CRPropa modules are summarized in table 3.1.

3.2.4.2   Total Gamma Ray Flux

In Figure 3.10 the resulting flux of gamma rays from the synthetic cloud is shown. All models show the same energy scaling in the intermediate energy range ($20 \leq E/\text{GeV} \leq 10^5$), but differ in the absolute normalisation[6]. In the lower panel of Figure 3.10 one can see that the difference in normalization in this regime is up to a factor ~ 2.

At the higher energies ($E > 10^5 \, \text{GeV}$) all applicable models show an exponential cut-off due to the maximum energy of protons in the simulation. In the lower energies ($E \leq 1 \, \text{GeV}$) a clear difference between the models can be seen. The models from Kafexhiu [72] and ODDK [96, 97] show a clear enhancement of gamma-ray flux around these energies compared to the AAfrag model [71].

---

[6]The lines for the Kelner model at $E_\gamma < 10 \, \text{GeV}$ and the ODDK model at $E_\gamma > 10^4 \, \text{GeV}$ are not shown, as these energies are not covered in the models. The argument about the agreement stays the same when extrapolating the curves.

module	Parameters
propagation	
SimplePropagation	$l_{\min} = 10^{-6}$ pc, $l_{\max} = 0.1$ pc
interaction	
HadronicInteraction	cross-section model, density profile
NuclearDecay ^{a}	havePhotons = True
observer & output	
TextOutput	Event3D
ObserverDetectAll	
ObserverNucleusVeto	
source	
SourceParticleType	$(A, Z) = (1, 1)$
SourcePowerLawSpectrum	$E_{\min} = 1\,\mathrm{GeV}$, $E_{\max} = 10^7\,\mathrm{GeV}$, $\alpha = -1$
SourceLambertDistribuionOnSphere	R_{GMC}, $\vec{r_0} = (0, 0, 0)$, inwards = True
boundary	
MinimumEnergy	$E_{\mathrm{br}} = 0.1$ GeV
MaximumTrajectoryLength	$D_{\max} = 2.4\,R_{\mathrm{GMC}}$

^{a} The nuclear decay is included for the AAfrag cross-section model, which also provides secondary neutrons, which can decay further.

Table 3.1

CRPropa Modules used for the simulation of the synthetic GMC.

Comparing the full AAfrag model (black solid line) with the AAfrag light model (red dash-dotted line), which only includes light secondaries, does not show any significant difference. This implies that the impact of multiple interactions in the cloud is negligible and the differences in the energy loss shown in section 3.2.3.3 do not affect the result.

3.3 Summary and Discussion

CRPropa is a powerful tool to model CRs and their interaction in various astrophysical applications. With its modular structure it can be easily adapted to the physical system of interests and the influence of individual processes can be highlighted. It allows a direct comparison between the diffusion approximation using the Stochastic Differential Equations and real particle trajectories in turbulent magnetic field. In the public version a lot of interactions processes for the CRs and gamma rays are implemented, that are relevant for the propagation of CRs in local source environments and for Ultra High Energy Cosmic Rays traveling through the extragalactic space.

The implementation of hadronic interaction from p-p collisions as presented
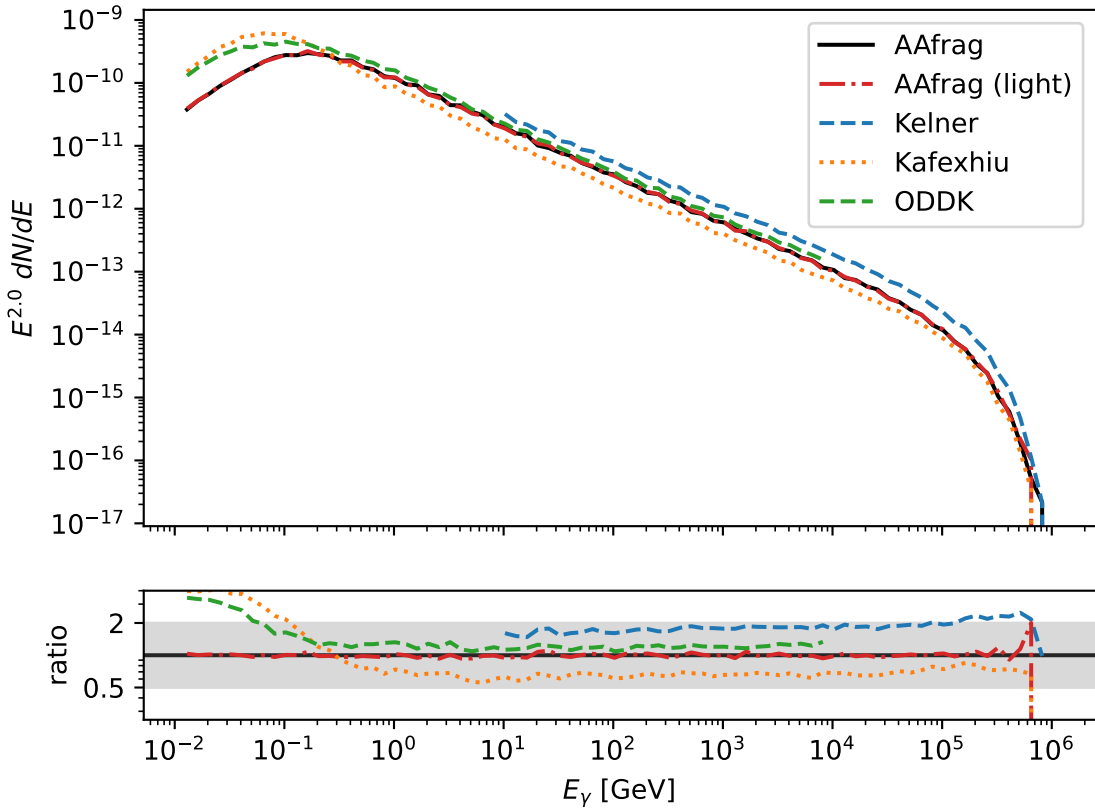
Figure 3.10. *Upper panel:* Gamma ray flux from the interaction of CR protons from the LIS in the synthetic GMC based on different cross-section models. *Lower panel:* Ratio between the different flux predictions. Here, the AAfrag model is used as a baseline. The gray band indicates a difference of a factor 2.

above, allows the usage of the CRPropa framework for Galactic cosmic rays and detailed studies of their non-thermal emission signatures. In the Milky Way these inelastic collisions are expected to be the main energy loss. The implementation as an additional plug-in into the CRPropa code allows easy combination with all existing features of the framework. It is designed in the style of CRPropa allowing for the maximal flexibility from the user side, including a free choice of the parametrization for the secondary production cross-section.

The example application of different cross section parametrizations and tables in a synthetic giant local molecular cloud reveals a difference of a factor ~ 2 between different models. Largest differences are between the model from Kelner [75] and Kafexhiu [72]. It shows the need for a tool in which these uncertainties can be tested systematically and more refined measurements and theoretical descriptions for the proton proton interactions.

In the following chapters it will be demonstrated how the gamma-ray production of the CRs can be modeled in realistic astrophysical systems and how it gamma rays can help to identify the transport process of GCRs.

Chapter 4

Cosmic Ray Transport in the Galactic Center

The Central Molecular Zone (CMZ) surrounding the gravitational center of the Milky Way (Galactic Center; GC) is one of the most extreme and close-by astrophysical environments. In previous approaches, the very high energy emission (VHE) has been modeled in 1D or used a simplified isotropic diffusion. Here, the impact of a realistic 3D magnetic field configuration and gas distribution on the VHE gamma-ray signatures is studied.

This chapter is structured as follows: In section 4.1 the observations of the CMZ in VHE gamma-ray are summarized. In section 4.2 the details of the environmental model and the corresponding observations are shown. In section 4.3 the details of the simulation setup are given. The final analysis and results are given in section 4.4 and a summary and discussion follow in section 4.5.

4.1 Observations of the GC

The observation of VHE gamma rays with the High Energy Stereoscopic System (HESS) originating from the CMZ is one of the first hints for a Galactic *PeVatron*, a source of CRs which can accelerate protons up to PeV energies [8]. The central source J1745 – 290 is only observed up to 19 TeV, which is consistent with an exponential cut-off at $E_{\gamma,\text{cut}} = 10.7\,\text{TeV}$ [8] or a broken power-law [17, 92]. While the exponential cut-off is motivated by the maximal energy of the acceleration, the break in the SED can be motivated by a change of transport behavior, i.e. the change from diffusion in the resonant scattering regime to the quasi-ballistic regime [92].

As the maximum gamma-ray energy of the central point source is not high enough to identify a *PeVatron*, this association is done using the diffuse emission of the CMZ, which exceeds the maximum energies of several 10 TeV. The analysis by HESS does not show any significant cut-offs for proton energies $E_{\text{p,cut}} \leq 1$ PeV. The observed spectrum is hard, with a spectral index $\Gamma = 2.32 \pm 0.16$, favoring a diffusion of CRs within a Kolmogorov-like turbulence.

In the first HESS analysis, the diffuse gamma rays have been considered in a
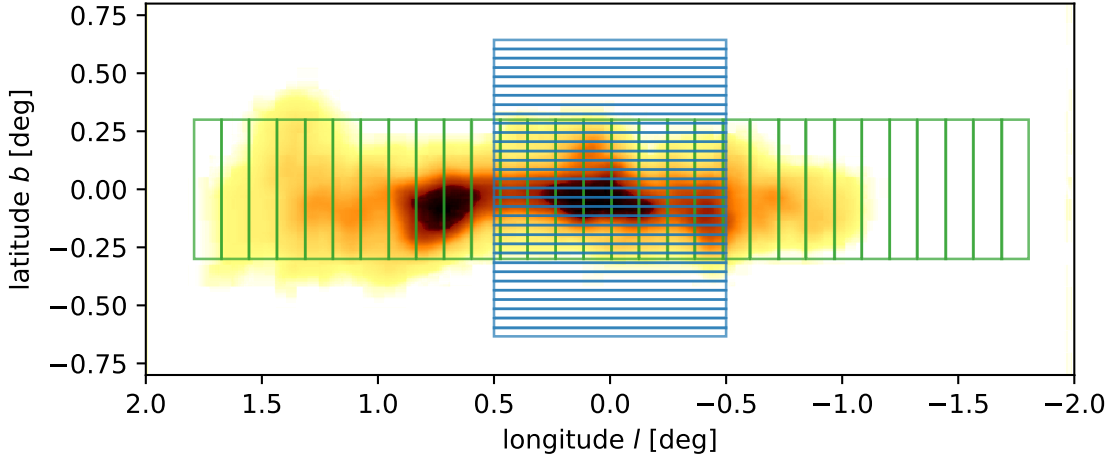
Figure 4.1. Integration windows for the longitudinal (green) and latitudinal (blue) profiles. The background map is the dense gas component template used in the HESS analysis [5]. Note that the background map shown is not the total gamma-ray excess used for the profiles, but it describes its spatial extent quite well.

ring between $0.15°$ and $0.45°$ around the GC[1]. In the second analysis [5] HESS also provided spatial profiles for the VHE diffuse emission. To only account for the diffuse emission the contributions from two point sources HESS J145 − 290 and G0.9+0.1, as well as the normalized background map have been subtracted. To calculate the longitudinal (latitudinal) profile the gamma-ray counts have been integrated in the range $-0.3° \leq b \leq 0.3°$ ($-0.5° \leq l \leq 0.5°$). The spatial data are binned with $\Delta l = 0.12°$ ($\Delta b = 0.04°$). Figure 4.1 shows the integration windows in front of the dense gas component, which has been fitted to the residual gamma ray counts in [5]. The dense gas is the main contributor to the gamma-ray excess. The corresponding integration windows cover most of the gas regions.

The VHE gamma-ray emission from the GC has also been observed with MAGIC [9] and VERITAS [13]. In the high energy range, the emission from the CMZ has been detected by the FermiLAT. This emission at GeV energies shows deviations from the typical expectation of CR transport [11] and dark matter has been proposed to be a possible contributor at this energies [46, 60].

In the ultra-high energy band (> 100 TeV) HAWC reported the first detection of gamma rays from the GC [19]. At the highest energies, the emission is softer with a power law index $\gamma = -2.88 \pm 0.25$ but does not show an exponential cut-off.

4.2   Modeling the CMZ

To model the CR transport and the gamma-ray production inside the CMZ three main ingredients are needed: (1) the gas distribution, (2) the magnetic field configuration, and, (3) the CR sources. If one wants to include the anisotropy of the spatial diffusion, a three-dimensional model for the magnetic field and consequently

---

[1]Some parts of the ring have been excluded to avoid contamination by the point source HESS J1746 − 285

the gas distribution is needed.

4.2.1 Gas Distribution

Creating a three-dimensional gas map from the observed column density is a complicated task. While on Galactic scales information from the Doppler shift combined with some assumptions on the Galactic rotation can be used to infer the position along the line of sight (LOS), this is not possible for the CMZ. The typical assumption of circular motion around the GC breaks at small radii. The measurement of proper motion by tracing masers is only available for some individual sources/clouds within the CMZ but has not resulted in a global kinematic model yet [107].

In this work, the simplified model from [54] for the inner Galaxy is applied. It is based on the assumption of an ellipsoidal shape of the CMZ with an inner cavity. The density distribution can be parametrized as

$$n(\vec{r}) = n_0 \exp\left\{ -\left(\frac{\sqrt{X^2 + (2.5Y)^2} - X_c}{L_c} \right)^4 - \left(\frac{z}{H_c} \right)^2 \right\} \quad , \qquad (4.1)$$

where X and Y are the coordinates along the major and minor axes of the ellipsoid in the Galactic plane, and z is the height above it. The parameters for the shift of the center X_c, the extent in the plane L_c, and the scale height H_c are fitted to the observed column density data. The normalization of the gas density is chosen to match the observed total mass of the CMZ. The model contains both, the atomic (HI) and the molecular (H_2) gas, where the latter one is the dominant.

In Figure 4.2 the latitudinal extent of the diffuse gamma-ray emission (black squares) and the gas distribution as parametrized by [54] (green solid line), is shown. The observed gamma-ray emission shows a much larger scale height than the gas model predicts. As the gas distribution determines the largest possible extent of the gamma ray distribution, a larger scale height is needed here. In the following the scale height parameter is adjusted to $H_c = 30$ pc, which is near the upper limit of the observational uncertainties (orange dashed line in Figure 4.2).

4.2.2 Magnetic Field Configuration

The three-dimensional structure of the magnetic field can not be measured directly, therefore we rely on models based on different observations: In this work, the model from [62]. Guenduez *et al.* solve for the magnetic field as a superposition of individual (small-scale) components and a large-scale diffuse inter-cloud magnetic field based on model C from [56]. The localized structure can be grouped into three different categories: (1) molecular clouds, (2) non-thermal filaments, and (3) the inner 10 pc around SgrA*.

The magnetic field in the molecular clouds is mainly horizontal and the absolute strength is based on equipartition arguments of the magnetic field and the gas pressure. The only free parameter is the ratio $\eta = B_r/B_\phi$ between the radial and azimuthal magnetic field components. As suggested by Guenduez *et al.* [62] the value is set to $\eta = 0.5$.
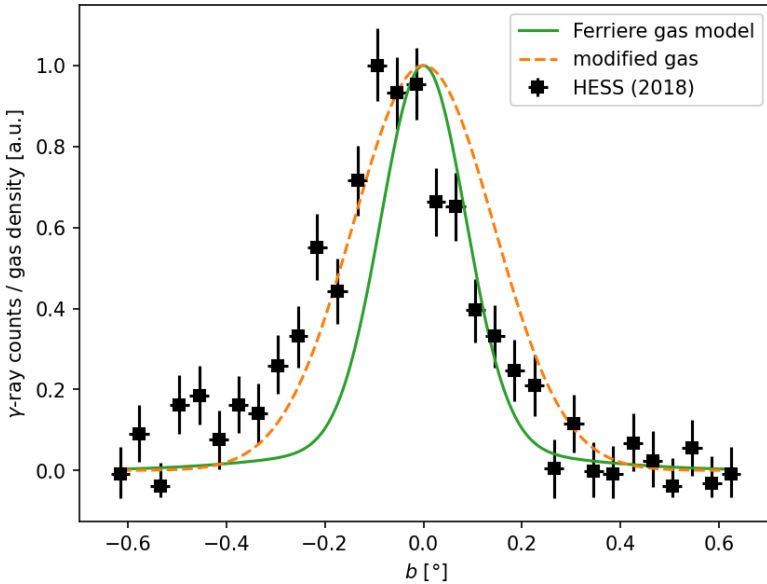
Figure 4.2. Latitudinal profile of the observed diffuse gamma-ray and the gas density in relative units. The gas model is shown for two different parameters of the scale height.

In the case of non-thermal filaments the magnetic field structure is mainly poloidal. All filaments have nearly vertical magnetic fields, except for the *Pelican* filament, which is rotated by 90°. All parameters for the field line opening and the magnetic field strength are following from the radio observations. The structure of the inner 10 pc around SgrA* is based on the work by [55] for the gas structure. It consists of a set of different molecular clouds in different shapes, for which the magnetic field is modeled analog to the molecular clouds discussed before. Additionally, Guenduez *et al.* introduce a magnetic field component with a purely poloidal shape.

For all these structures Guenduez *et al.* do not provide information about their position on the line of sight (LOS). For some of these clouds, different theories about their position and dynamics exist but are still under debate [65]. For simplification, we assume all structures to be in the plane perpendicular to the LOS centered in SgrA*, which is assumed to have a distance of $d_{SgrA*} = 8\,\mathrm{kpc}$ from Earth.

In the simulation, the most important small-scale structures for the confinement of CRs are molecular cloud SgrB2, the field in the inner 10 pc, and the non-thermal filament radio arc. Figure 4.3 shows their position with respect to the observed gamma-ray flux (background color map) and the source positions discussed below. In figure 4.4 example field lines starting at random positions of the outer boundary.

4.2.3   Cosmic Ray Sources

The origin of CR sources is still under debate. Therefore, two different scenarios for the source of CRs are considered here:

(i) The first scenario (**3sr**) is based on the observation of gamma-ray point sources. HESS has observed three point sources in the CMZ: SgrA*, the supernova
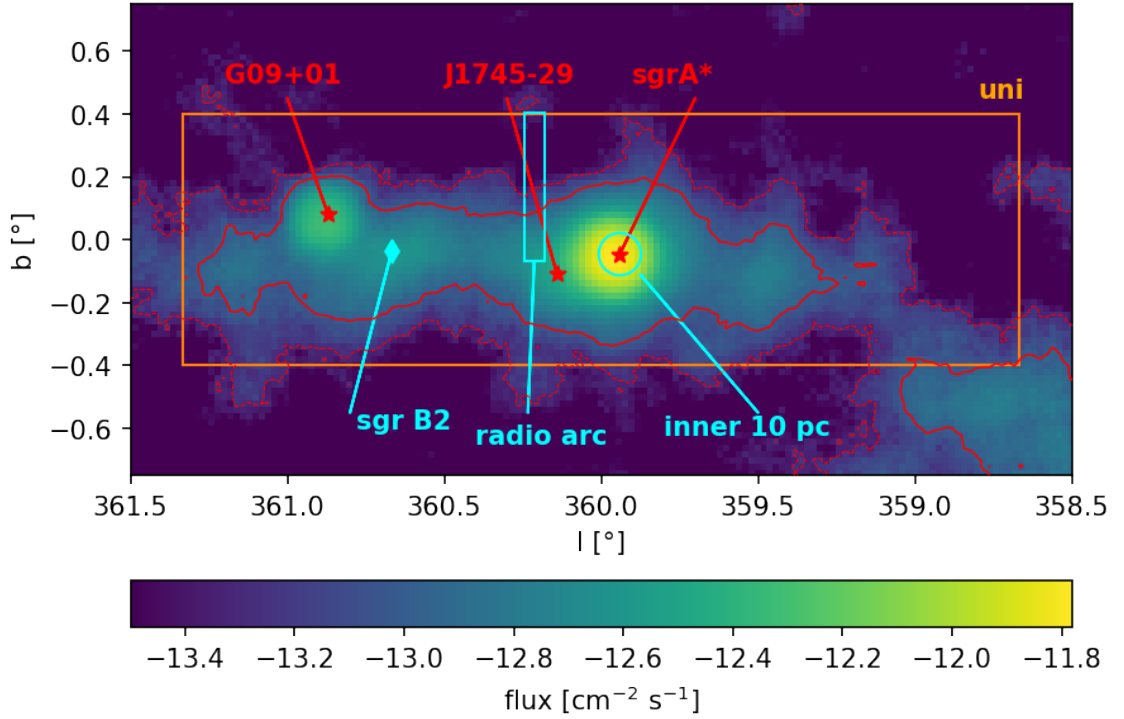
Figure 4.3. Observed gamma ray flux from the Central Molecular Zone. Here all flux before the reduction of the point sources is shown. Additionally, the two source types, point sources (red stars) and uniform box (orange rectangle), as well as the most important magnetic field structures (cyan) are indicated.

remnant G0.9+0.1, and HESS J1745-29. The contribution of each source to the total CR emission is based on their gamma-ray luminosity. The relevant parameters for the three sources are given in table 4.1.

(ii) The second scenario (**uni**) explored here, is based on acceleration sites outside the CMZ. The CRs from the Galactic Plane feed a sea of CRs which will fill up the full CMZ homogeneously.

name	identifier	longitude $l/°$	latitude $b/°$	rel. contribution
SgrA*	HESS J1745-290	-0.06	-0.046	$f_{\mathrm{sgrA}} = 0.72$
SNR-G	G0.9+0.1	0.87	0.08	$f_{G09} = 0.22$
Arc	HESS J1746-285	0.14	-0.11	$f_{\mathrm{J1746}} = 0.06$

Table 4.1

CR point sources in the CMZ.

The position of the sources is shown in Figure 4.3.

While the point sources in this work are focused on the observed gamma-ray sources, Scherer *et al.* [110, 111] focus on the emission from star clusters (i.e. the Nuclear Star Cluster [NSC], the Arches Cluster [AC], and the Quintuplet Cluster
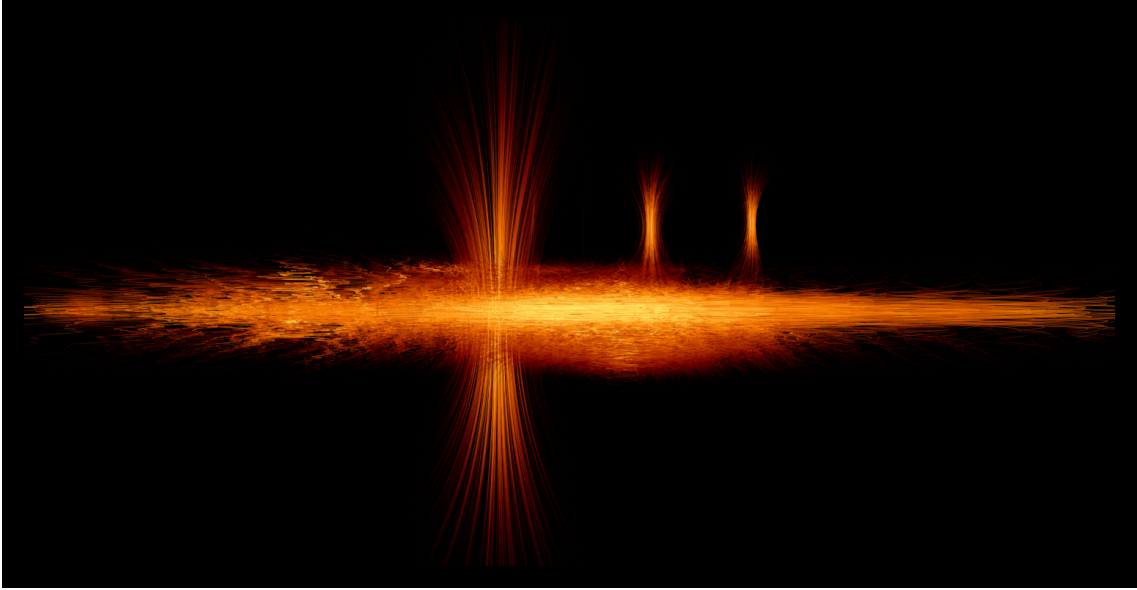
Figure 4.4. Field lines of the CMZ magnetic field model. Here the view of the y-z-plane is shown.

[QC]). Besides the NSC, they introduce an impulsive source sgrA East. For both sources the distance to SgrA* is much shorter than the resolution of H.E.S.S. Therefore, no difference in the choice of the source location is expected. The AC and the QC lay close to the observed gamma-ray source HESS J1746-285. It is not clear whether the HESS source is a site of CR acceleration or is illuminated by CRs accelerated at the clusters. In the outer CMZ, Scherer *et al.* discuss three different G-objects as possible sources (G1.1-0.1, G1.0-0.2, G0.9+0.1). They arbitrarily choose the middle one, while here, the only observed gamma-ray source G0.9+0.1 is used.

To simplify the simulation and minimize the number of free parameters, the injection of all CR sources follows the same power law

$$\frac{\mathrm{d}N}{\mathrm{d}E}\bigg|_{\text{source}} \propto E^{-\alpha_s} \quad , \tag{4.2}$$

where α_s is the injection index, which is kept as a free parameter.

4.3   Simulation Setup

The simulation of the CR transport in the CMZ is done with CRPropa 3.2 [23] (see chapter 3.1 for a summary) in two steps. In the first step, CRPropa is used to obtain the gamma-ray distribution for the simulated proton spectrum. In the second step, called post-processing, the simulated spectrum is reweighted to the assumed injection spectrum, and quantities in physically meaningful units are calculated.

4.3.1 CRPropa Simulation

In this work the effect of momentum diffusion and advection is neglected within the CMZ. The transport equation 3.2 simplifies to

$$\partial_t n = \nabla(\hat{\kappa}\nabla n) - \partial_p \left[\frac{\mathrm{d}p}{\mathrm{d}t} n \right] + Q \,. \tag{4.3}$$

Here, the diffusion tensor $\hat{\kappa}$ is anisotropic with respect to the background magnetic field. To quantify the anisotropy, the ratio $\epsilon = \kappa_\perp / \kappa_\parallel$ of the diffusion coefficient perpendicular ($\kappa_\perp$) and parallel ($\kappa_\parallel$) to the local magnetic field line is used. As the diffusion coefficient affects the motion of a pseudo-particle in the CRPropa simulation, it is not possible to use a re-weighting technique for the anisotropy. Therefore, only a limited number of values can be tested. To cover to possible range of the anisotropy, the values $\epsilon = 10^{-3}, 10^{-2}, 0.1, 0.3, 1$, ranging from strongly anisotropic to isotropic diffusion, are probed. The energy scaling of the diffusion tensor is taken from quasi-linear theory, and the normalization is based on the observed value at the Solar system. With this, the diffusion tensor reads

$$\hat{\kappa}(E, \vec{r}) = 6.1 \times 10^{24} \frac{\mathrm{m}^2}{\mathrm{s}} \cdot \left(\frac{E}{4\,\mathrm{GeV}} \right)^{\frac{1}{3}} \cdot \mathrm{diag}(\epsilon, \epsilon, 1) \tag{4.4}$$

in the coordinate system $x = B_{\perp,1}, y = B_{\perp,2}, z = B_\parallel$. Here E denotes the particle energy and diag is the diagonal matrix. The solution of the transport equation is calculated with the `DiffusionSDE` module (see [88] for details) using an adaptive step size between 10^{-3} and 10 pc with a precision of $P = 10^{-3}$.

The simulation volume is limited to a paraxial box of the size $200 \times 400 \times 120\,\mathrm{pc}^3$ centered on the GC. All particles reaching the boundary are lost into the Galaxy. The simulation is performed for protons in the energy range $1 \leq E/\mathrm{TeV} \leq 10^3$ with a simulated energy distribution $\mathrm{d}N/\mathrm{d}E|_\mathrm{sim} \propto E^{-1}$. This flat energy distribution allows for an equally small statistical error over the full energy range. The protons are propagated until they leave the simulation volume or a maximum time $T_\mathrm{max} = 500\,\mathrm{kpc}/c$ is reached. In all cases more than 99% of the particles have left the simulation volume after $t = 100\,\mathrm{kpc}/c$. Therefore, the choice of T_max is even more conservative.

For the interaction of the CRs with the ambient gas, the cross-section from Kelner *et al.* [75] (see section 2.2.2.1) is used. All gamma rays produced in the simulation are directly stored and no propagation and corresponding absorption of gamma rays is taken into account.

The simulation is performed in individual runs of $N_\mathrm{sim} = 10^5$ primary CRs. For all combinations of source distribution and anisotropy, at least 50 simulation runs were repeated[2]. A detailed list of the used CRPropa modules is given in table 4.2.

4.3.2 Post Processing

The output of the simulation is a list of the position and energy of all produced gamma rays including the information about the primary CR. In the first step, the

---

[2]For some parameter combinations additional runs have been performed to decrease the statistical noise.

module	parameter	value
magnetic field & propagation		
`CMZField`	sub-components	True
`DiffusionSDE`	precision	$P = 10^{-3}$
	minstep	$s_{\min} = 10^{-3}\,\mathrm{pc}$
	maxstep	$s_{\max} = 10\,\mathrm{pc}$
	anisotropy	$\epsilon \in \{10^{-3}, 10^{-2}, 0.1, 0.3, 1\}$
observer & output		
`HDF5Output`	enabled columns	TrajectoryLength
		position (source and current)
		energy (source and current)
		serial number
`Observer`	Particle veto	nucleus, electron, neutrino
	Observer feature	`ObserverDetectAll`
boundary & break condition		
`MaximumTrajectoryLength`	maximal time	$T_{\max} = 500\,\mathrm{kpc}/c$
`MinimumEnergy`	minimal energy	$E_{\min} = 1\,\mathrm{TeV}$
`ParaxialBox`	origin	$\vec{o} = (-100, -200, -60)\,\mathrm{pc}$
	size	$\vec{s} = (200, 400, 120)\,\mathrm{pc}$
`ObserverSurface`	surface	paraxial box as defined before
source		
`SourceParticleType`	particle id	proton (1000010010)
`SourceIsotropicEmission`		
`SourceMultiplePositions`	positions	SgrA* : $\vec{r} = (0, 8.9, -6.8)\,\mathrm{pc}$
		J1746: $\vec{r} = (0, -20.77, -16.32)\,\mathrm{pc}$
		G0.9+01: $\vec{r} = (0, -129.08, 11.87)\,\mathrm{pc}$
or `SourceUniformBox`	origin / size	$\vec{o}$ and $\vec{s}$ as above

Table 4.2

CRPropa modules used for the simulation and their input parameters. Module
parameters not mentioned are kept at their default values.

sky position of each gamma ray is calculated as

$$l = -\arctan\left(\frac{y}{x - r_E}\right) \quad \& \quad b = \arctan\left(\frac{z}{\sqrt{(x - r_E)^2 + y^2}}\right), \qquad (4.5)$$

where $\vec{r} = (x, y, z)$ is the position of the gamma ray and $r_E = 8.5$ kpc is the distance between Earth and SgrA*.

In the second step, the gamma rays are binned and reweighted according to their primary energy. For each particle a weight

$$w_i = \frac{E_i^{\alpha_s - 1}}{\sum_i E_i^{\alpha_s - 1}} \qquad (4.6)$$

is assigned, where α_s is the source index and E_i is the source energy of the primary CR. Here, the source injection with $1 \leq \alpha_s \leq 3$ with steps of $\Delta\alpha_s = 0.1$ is tested.

The gamma rays are binned in sky position and energy. The binning of the sky position is done with a resolution of $\Delta l = 0.016°$ and $\Delta b = 0.01°$, which is much finer than the resolution of the current generation imaging air Cherenkov telescopes (IACTs). The resolution effects of the observation are later taken into account when the results are compared to the measurements. The finer binning also allows comparisons with upcoming IACTs like the Cherenkov Telescope Array (CTA), which has an expected angular resolution of $0.03°$ [123]. The energy binning is done in the same ranges as the H.E.S.S. observation [5].

4.4 Model Results

4.4.1 Spectral Energy Distribution

For the CMZ several instruments measured the spectral energy distribution of the diffusive emission (see section 4.1). This analysis estimates the source injection following a single power-law $\mathrm{d}N/\mathrm{d}E|_s \propto E_0^{-\alpha_s}$ with the injection index α_s.

Analogously to the H.E.S.S. analysis [5] all gamma-rays in a ring centered in SgrA* with a radius $0.15° \leq r_{\mathrm{SgrA*}} \leq 0.45$ are collected. The distance to SgrA* is calculated as

$$r_{\mathrm{SgrA*}} = \sqrt{(l - l_{\mathrm{SgrA*}})^2 + (b - b_{\mathrm{SgrA*}})^2} \quad . \qquad (4.7)$$

The analysis for the MAGIC [9] and VERITAS [13] is done for slightly different areas, which might explain the differences in the measured fluxes (compare Figure 4.5). The results from the H.E.S.S. collaboration cover the largest energy range and have the smallest energy binning. Therefore, the sky region from this analysis is chosen.

To minimize the impact of statistical fluctuation in the simulation, the simulated SED is fitted either with a single power-law

$$\Phi = \frac{\mathrm{d}N}{\mathrm{d}E} = \Phi_0 \left(\frac{E}{1\,\mathrm{TeV}}\right)^{-\alpha} \quad , \qquad (4.8)$$
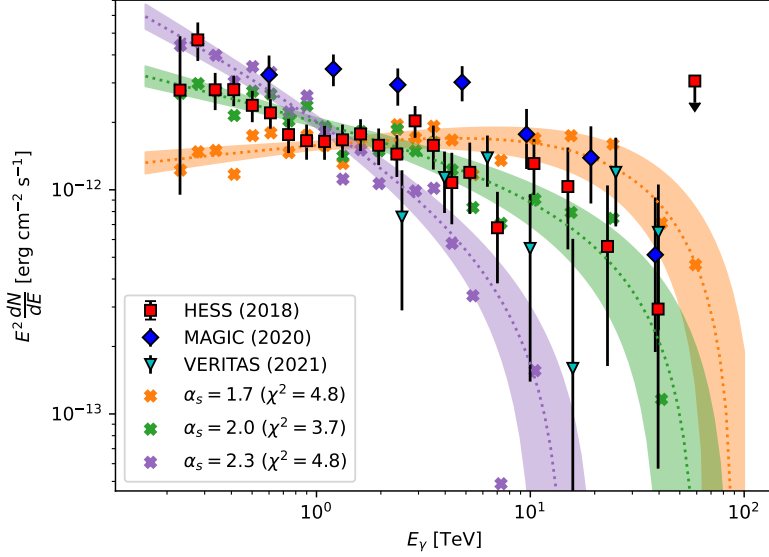
Figure 4.5. Example SED for different injection slopes and the fits following a power-law with exponential cut-off (see eq. 4.9) are shown. Here, the data for the **3sr** source scenario with an anisotropy of $\epsilon = 0.1$ is shown.

or a power-law with exponential cut-off

$$\Phi = \frac{\mathrm{d}N}{\mathrm{d}E} = \Phi_0 \left(\frac{E}{1\,\mathrm{TeV}} \right)^{-\alpha} \exp\left\{ -\frac{E}{E_c} \right\} \quad . \tag{4.9}$$

Here, Φ_0 is the flux normalization at 1 TeV, α denotes the spectral index, and E_c is the cut-off energy. The spectral index and the cut-off energy are directly taken from the simulated SED, while the normalization is chosen to minimize the reduced χ^2

$$\chi^2_{\mathrm{red}} = \frac{1}{n-1} \sum_{i=1}^{n} \frac{(c_i^{\mathrm{obs}} - c_i^{\mathrm{sim}})^2}{\sigma_i^2} \quad . \tag{4.10}$$

Here, c_i denotes the observed or simulated flux in the i-th energy bin and σ_i is the uncertainty from the observation. The simulated flux c_i^{sim} is calculated from the fit following equation 4.8 or 4.9. All data, shown in Figure 4.5 are considered. The optimal value for the source injection leading to the smallest χ^2 is given in table 4.3. The power-law fit leads to a slightly harder injection than the cut-off, but all values are close to the results from the diffusive shock acceleration (DSA, $\alpha_s = 2.0$). The absolute value, shown in Figure 4.6, does not differ strongly between different source scenarios or anisotropy parameters.

The gamma-ray production is based on hadronic interactions, therefore, also a neutrino component is expected. The all-flavor neutrino flux can be approximated from the gamma-ray flux [34] as

$$\Phi_{\nu,\mathrm{tot}}(E_\nu) = 6\,\Phi_\gamma \left(\frac{E_\nu}{2} \right) \quad . \tag{4.11}$$

Using this neutrino flux for all of the optimal source injection indices summarized in table 4.3 and the effective area A_{eff} of the Galactic Plane detection in neutrinos by

source	$\epsilon = 10^{-3}$	$\epsilon = 10^{-2}$	$\epsilon = 0.1$	$\epsilon = 0.3$	$\epsilon = 0.1$
	Power-law (eq. 4.8)				
3sr	1.9	1.9	1.9	1.9	1.9
uni	1.9	1.9	1.9	2.0	2.0
	Power-law with cut-off (eq. 4.9)				
3sr	1.9	2.0	2.0	2.0	2.0
uni	2.0	2.0	2.0	2.1	2.0

Table 4.3

Optimal source injection index α_s depending on the fitting function and the anisotropy.

IceCube [3] the expected number of neutrino events from the CMZ can be estimated as

$$N_\nu = \Delta t \int \Phi_\nu(E) A_{\text{eff}}(E) \, dE \quad . \tag{4.12}$$

Assuming a 10 year lifetime of the IceCube detector the expected number of events is between 0.015 and 0.019. This makes the observation of the CMZ as a point source in the Galactic Plane sample impossible.

4.4.2 Required Source Luminosity

In this section, the required energy budget from the point sources within the CMZ is calculated. For each anisotropy ϵ a smaller simulation with $N_{\text{prim}} = 10^4$ primaries is used. Additionally to the output described in section 4.3 all primary particles are stored before the propagation starts.

Eichmann and Kachelrieß [Appendix A in 51] introduce a weighting scheme based on the luminosity of the source and its distance to the observer r_{obs}. The ratio between the simulated flux J (in units particles/TeV) and the physical flux Φ is independent of the observed particle species. In this case, the normalization factor $f_\gamma = \Phi_\gamma(1\,\text{TeV})/J(1\,\text{TeV})$ can be calculated with the same fitting procedure as presented before.

Applying this conversion factor to the simulated proton spectrum J_p, the total CR luminosity is estimated as

$$L_p(E \geq 10\,\text{TeV}) = \int\limits_{10\,\text{TeV}}^{1\,\text{PeV}} 4\pi r_{\text{obs}}^2 \, E_p J_p(E_p) f_\gamma \, dE_p \quad . \tag{4.13}$$

The resulting source luminosity for the $\alpha_s = 2$ injection, depending on the anisotropy parameter is shown in Figure 4.7. Only a weak dependence on the anisotropy can be seen and all values are in the required acceleration rate of $10^{37} - 10^{38}\,\text{erg}\,\text{s}^{-1}$ as estimated by H.E.S.S. [8].
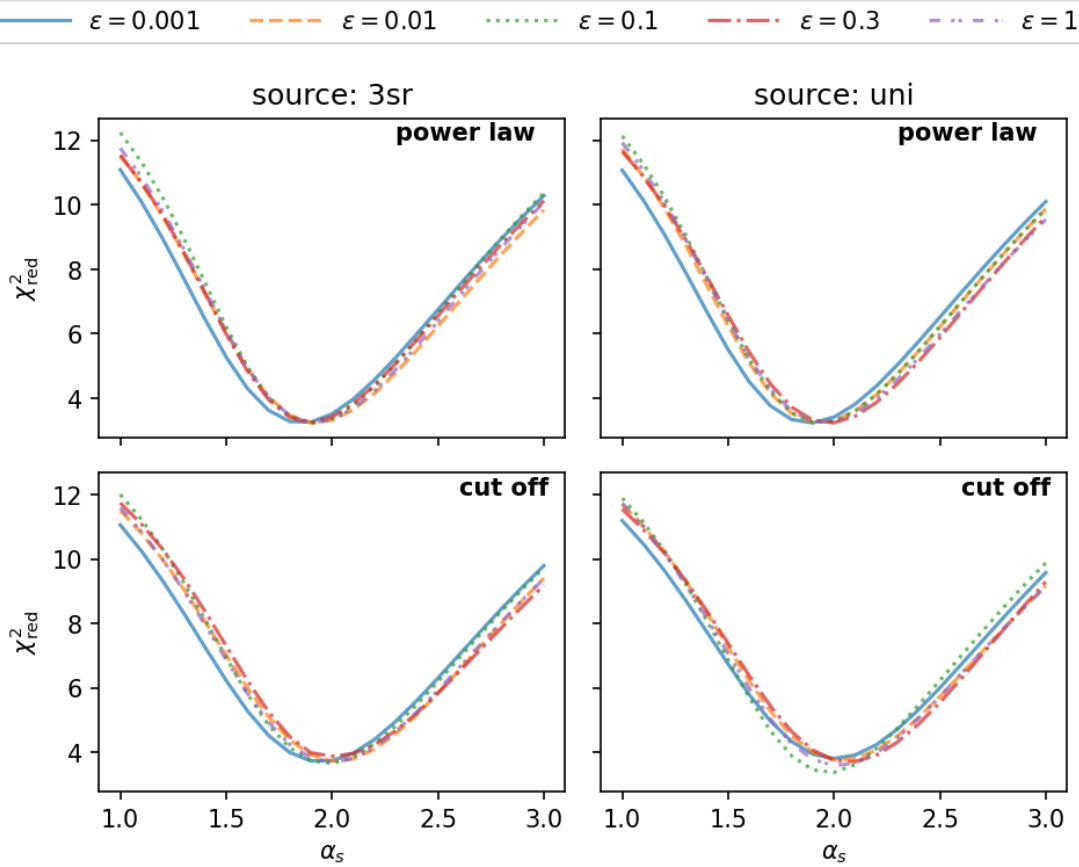
Figure 4.6. Agreement of the simulated SED to the observation, depending on the source injection index. The column denotes the different spatial source models and the row describes the fitting procedure. The position of the minimum is summarized in table 4.3.

4.4.3   Synthetic Gamma Ray Count Maps

Besides the spectral information of the gamma-ray emission also the spatial distribution can be analyzed. Taking the 3D histograms introduced before we can calculate synthetic energy integrated count maps. A source injection index $\alpha_s = 2.0$, consistent with the DSA and the results from section 4.4.1, is assumed in the results shown here. In Figure 4.8 the raw maps are shown. These maps show a significant statistical fluctuation and can not be easily compared to observation. Therefore, a smearing with the resolution of the observing instrument is needed. In the first step, the simulation will be compared to the results from H.E.S.S. The observations have a resolution of $\sigma = 0.077°$, which is the 68 % containment radius of the point spread function [5]. The smeared count map is shown in Figure 4.9.

The strong parallel diffusion ($\epsilon = 10^{-3}$) in the top panel of figures 4.8 and 4.9 shows a strong confinement of CRs in the small-scale magnetic structures. Consequently, the gamma-ray production around SgrA* and Sgr B2 is enhanced. The two source scenarios differ in the relative contribution of the two excesses. In the point source injection, the emission around SgrA* is stronger, as two of the three sources are close by and emitting over 75% of the total CRs. Whereas, the uniform source
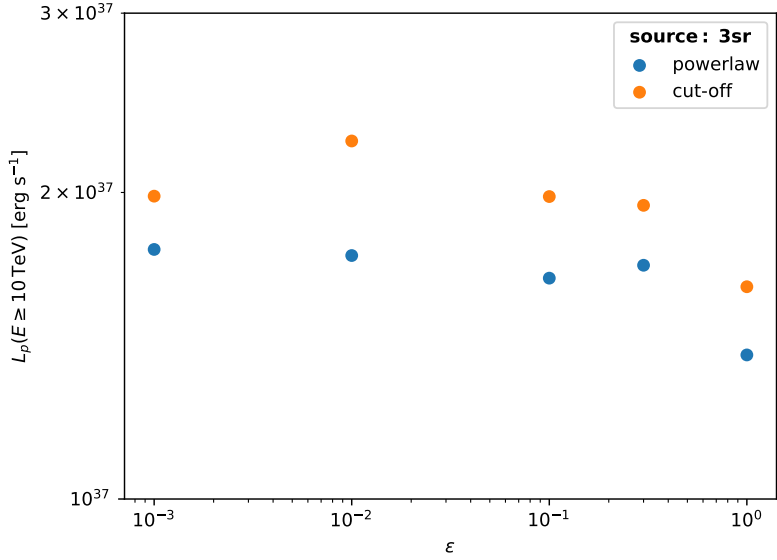
Figure 4.7. Required source luminosity for the **3sr** source scenario.

distribution shows only a small excess close to SgrA*, while the region around Sgr B2 has a stronger peak.

By increasing perpendicular diffusion the point-like emission is smeared out and the diffuse inter-cloud contribution becomes more relevant. In the case of the isotropic diffusion with point source injection, the contribution from G0.9 is barely visible. In the case of the uniform injection, no substructure is visible at all.

The synthetic gamma-ray maps also allow predictions for future generation IACTs. The upcoming Cherenkov Telescope Array (CTA) is aiming for an angular resolution of $\sigma = 0.03°$ [123]. In Figure 4.10 the prediction for CTA is shown. Especially in the strong parallel diffusion case, CTA will be able to differentiate between substructures in the magnetic field configuration. For future observations, a dedicated look at the non-thermal filament structures could help to identify the transport properties.

4.4.4 Longitudinal and Latitudinal Profiles

A more quantitative comparison of the synthetic gamma-ray maps is done with the longitudinal and latitudinal profiles measured by H.E.S.S. (see Figure 4 in [5]). To account for the H.E.S.S. resolution a Gaussian smearing with $\sigma = 0.077°$ has been performed. The integration over the latitudinal (longitudinal) window of $|b| \leq 0.3°$ ($|l| \leq 0.5°$) is done analog to the H.E.S.S. analysis. The normalization of the simulation data is chosen, so that the maximum counts in the latitudinal profile match the middle of the observed peak at $b = -0.054°$. The normalization for the longitudinal profile follows automatically.

The resulting profiles are displayed in Figure 4.11. Similar to the 2D profiles a strong anisotropy ($\epsilon = 0.001$ and $\epsilon = 0.01$) results in a strong peaking distribution around the magnetic structures (SgrA* and Sgr B2). For the latitudinal distribution, the thickness of the disk is too small compared to the data, regardless of the source
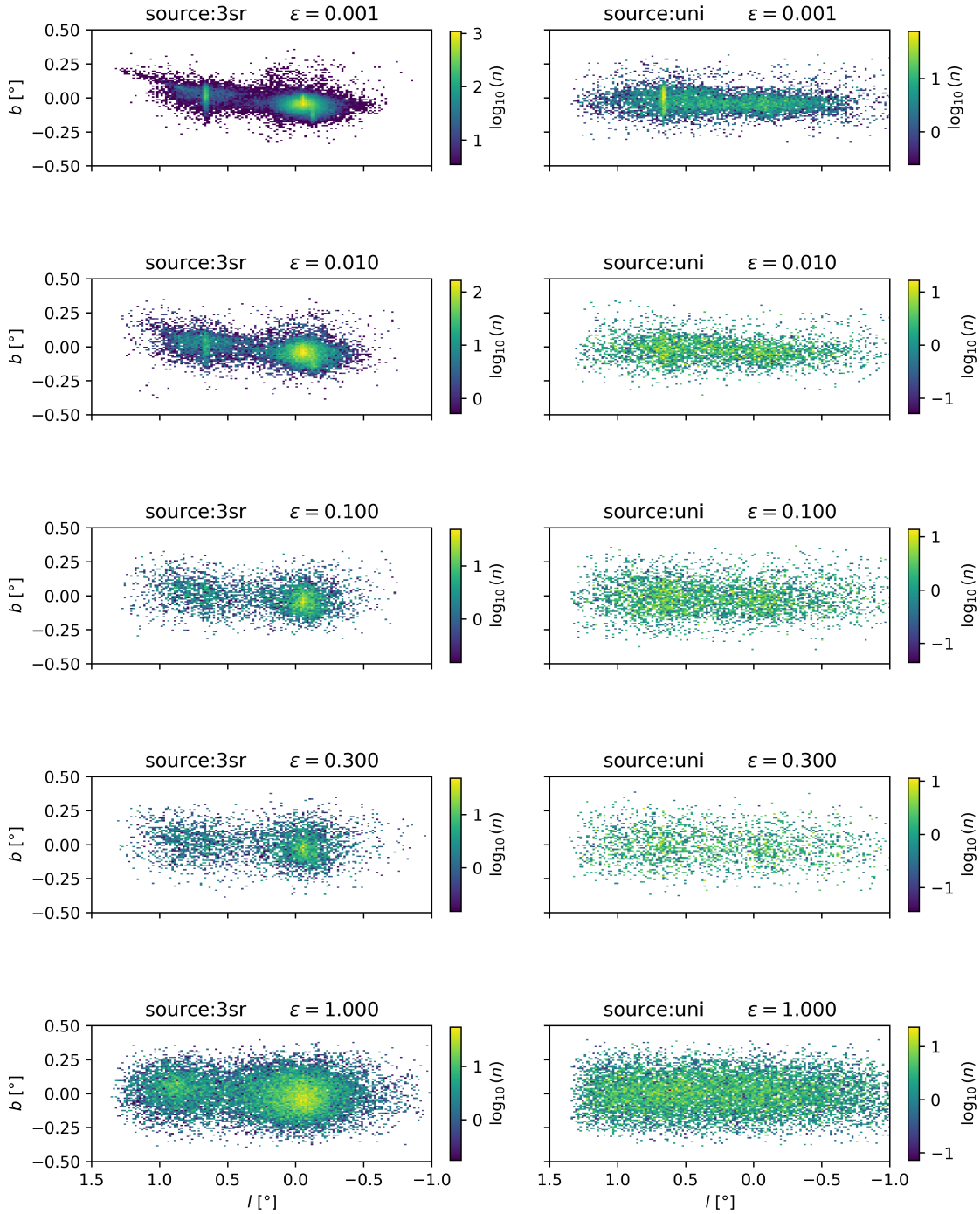
Figure 4.8. Synthetic count maps for the energy integrated gamma-ray flux. Here, no additional smearing was applied. The left column shows the point source injection and the right column shows the uniform source distribution. The row denotes the anisotropy parameter from strongly anisotropic (top) to isotropic diffusion (bottom). All color scales are normalized to the maximum value of the map.
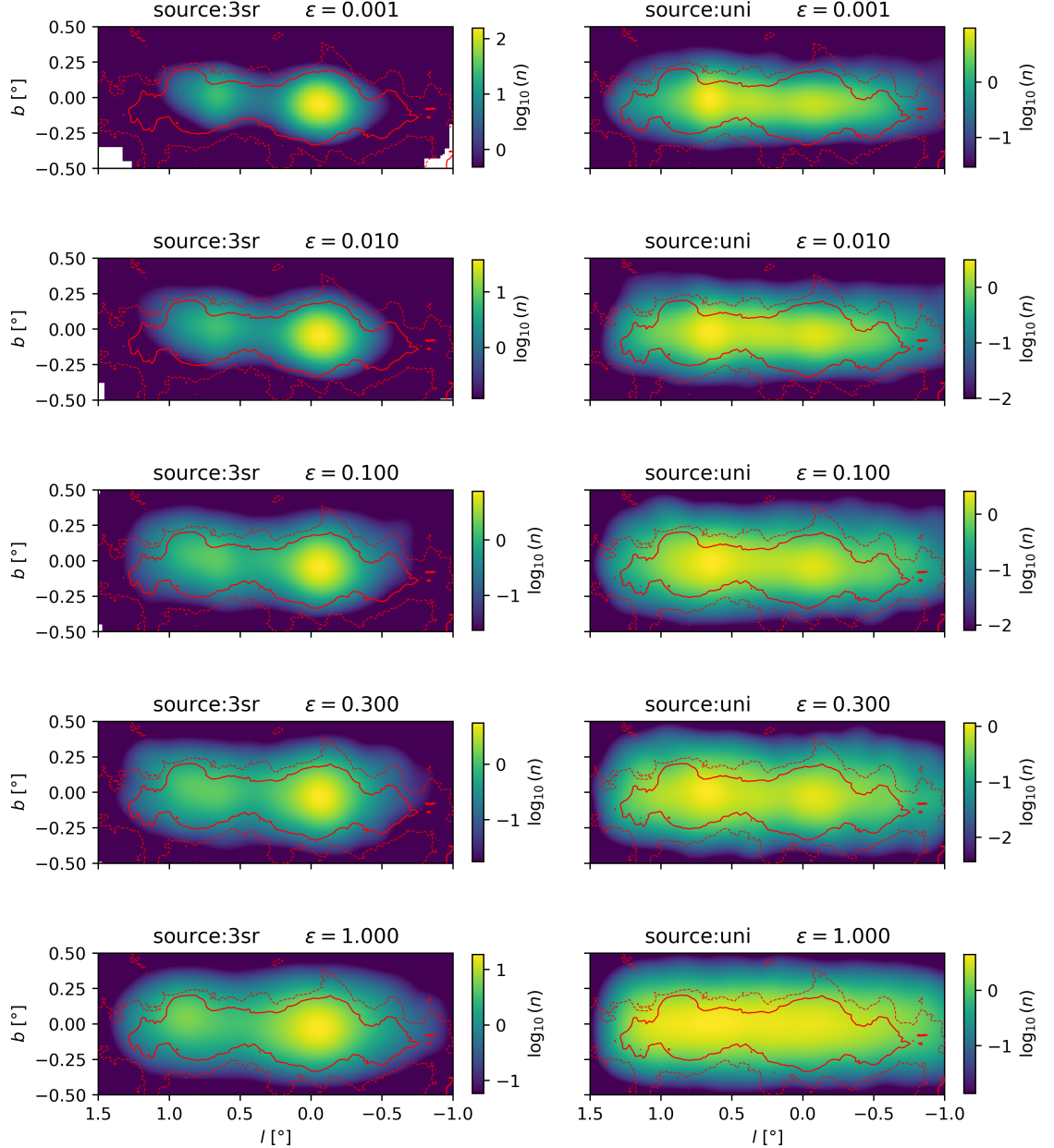
Figure 4.9. Same as Figure 4.8 but smeared with the H.E.S.S. resolution. The red lines show the contours of the observed flux by H.E.S.S. [5] for $\Phi = 5 \times 10^{-14}\,\mathrm{cm}^{-2}\,\mathrm{s}^{-1}$ (dashed) and $\Phi = 10^{-13}\,\mathrm{cm}^{-2}\,\mathrm{s}^{-1}$ (solid).
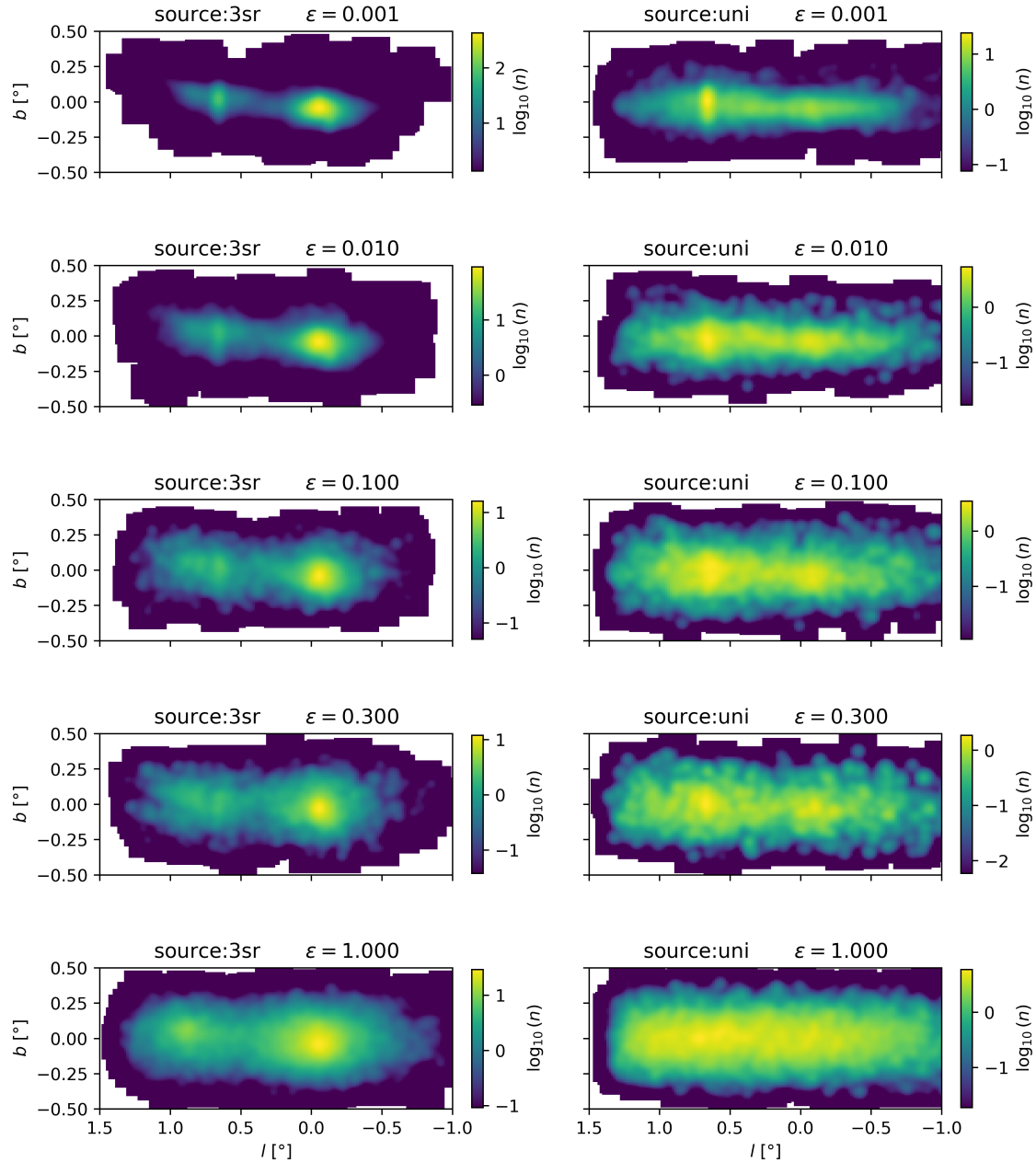
Figure 4.10. Same as Figure 4.8 but smeared with the aimed CTA resolution $(\sigma = 0.03°)$ [123].
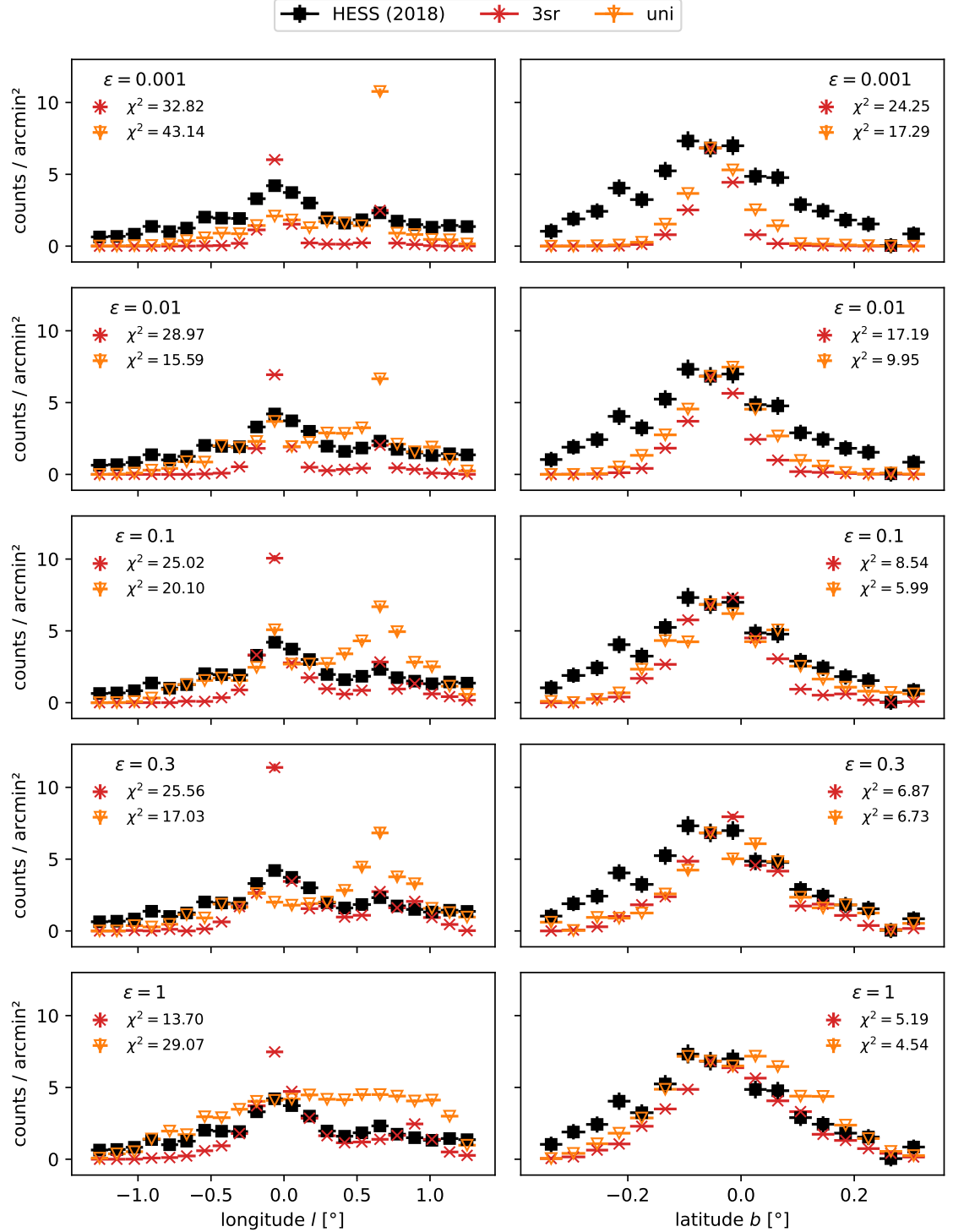
Figure 4.11. Longitudinal (left) and latitudinal (right) profile of the gamma-ray distribution. The row denotes the anisotropy parameter.

configuration. In the longitudinal profiles, sharp peaks around SgrA* and Sgr B2 are visible. For the uniform source distribution, the maximum is given around the peak at Sgr B2 and overshoots the data. For the point source injection, the ratio between the peaks is more compatible with the data, although the excess at SgrA* is too strong.

To get a more quantitative comparison, the reduced χ^2 following equation 4.10 has been calculated for all source/anisotropy combinations. In Figure 4.12 the χ^2 values are shown depending on the anisotropy parameter ϵ. The optimum in the latitudinal distribution is given for the uniform source distribution with isotropic diffusion, but the difference to the point source distribution is not significant. In the longitudinal profile, a clear preference for the point source in the isotropic diffusion case can be seen.
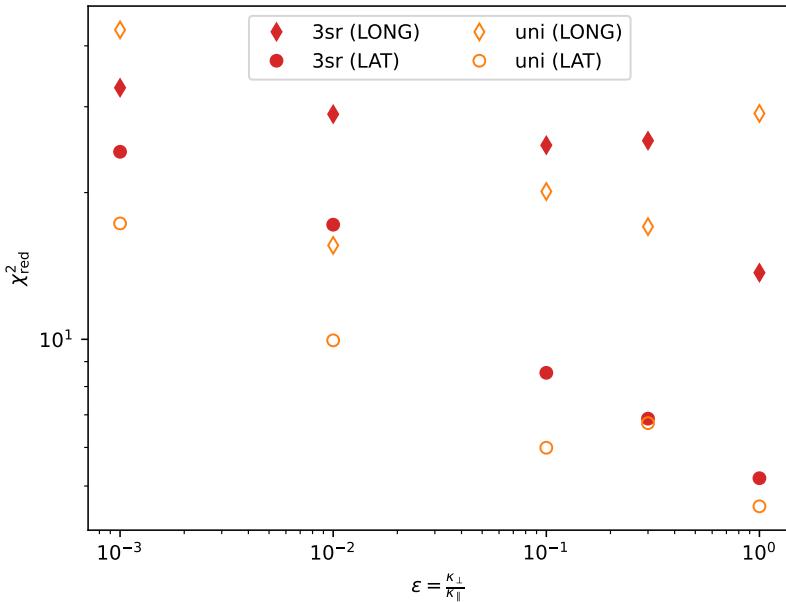
Figure 4.12. Reduced χ^2 values for the consistency of the longitudinal and latitudinal profiles to the data.

The uniform source distribution with isotropic diffusion does not show any peaks. This is expected as the gamma-ray distribution is independent of the magnetic field configuration and the gas distribution does not have individual peaks. Here, also the maximal extent of the dense gas in the CMZ can be seen, which determines the maximal extent of the diffuse emission. To match the observed data in the outer regions a more extended CMZ or a second thinner gas contribution would be needed.

4.5   Summary and Discussion

The prediction of the gamma-ray emission presented in this chapter is based on a 3D magnetic field configuration and a 3D gas distribution. To properly model the

underlying CR distribution detailed knowledge of the CR sources and the transport properties is needed. Here, the usage of gamma-ray observation of compact regions to constrain the transport properties, especially the ratio of the diffusion coefficient perpendicular and parallel to the local magnetic field line $\epsilon = \kappa_\perp/\kappa_\parallel$, is demonstrated.

This work is based on the 3D magnetic field from [62] and the gas distribution from [54]. To match the observed thickness of the disk in gamma-ray observations, the exponential scale height has been adapted to $H_c = 30\,\mathrm{pc}$. The gas distribution determines the maximal extent of the possible gamma-ray emission, independently of the transport model.

The model is based on three free parameters, (a) the class of the CR sources, (b) the anisotropy of the diffusion tensor ϵ, and (c) the power-law index of the injection spectrum α_s. To estimate these parameters two different observables have been used: (i) the overall spectral energy distribution (SED) from a ring centered in SgrA*, and (ii) the spatial profiles along the longitudinal and latitudinal axes.

From the SED a constraint on the source injection index α_s can be derived. Independently on the source distribution and the anisotropy of the diffusion tensor, the best agreement to the data can be achieved for $\alpha_s \approx 2$, which is expected from diffusive shock acceleration. If one assumes that the CR sources are point sources in the CMZ, the required energy budget is in the range of $10^{37} - 3 \times 10^{37}$ erg/s and nearly independent of the chosen anisotropy. This value is compatible with the values derived by the H.E.S.S. collaboration [5].

Based on the spatial distribution of the gamma rays, constraints on the source distribution and the anisotropy of the diffusion tensor can be derived. In the latitudinal profile, a weak preference for isotropic diffusion can be found, but small anisotropies can not be excluded. In the longitudinal profiles a clear preference for the point source injection, rather than the uniform source distribution coming from a Galactic CR sea, is observed. The fully isotropic case ($\epsilon = 1$) leads to the best agreement with the data. Nevertheless, the position of the peak around the source G0.9+0.1 is not in spatial agreement with the measurements from H.E.S.S., which predicts the maximum at the position from SgrB2. All models with an anisotropy ($\epsilon < 1$) have the peak at the right position. Therefore, one can see that a limited impact of the magnetic field structure is still expected.

In this work, a detailed magnetic field structure has been used. For all of the small-scale elements in the field, the absolute position along the line of sight (LOS) is not clear. Changes here could imply strong differences in the resulting gamma-ray distribution, especially in the strongly anisotropic scenarios. At the moment it is not clear whether the proposed changes in the scale height of the gas distribution would also imply changes in the inter-cloud magnetic field model. This would weaken the constraint on the anisotropy from the latitudinal profile. Besides the uncertainties in the magnetic field model, one has to keep in mind that the used gas distribution is quite simplistic. While the magnetic field has a lot of substructures there are no corresponding structures included in the density. For a more realistic investigation, those density fluctuations would have to be taken into account. If the density is locally increased, one would expect that the gamma-ray production is even more enhanced at this position. Therefore the problem of the excess of the longitudinal

profile in the simulation compared to the data would become even stronger. This might imply problems in the derivation of the field strength in the clouds or their position along the LOS.

This model neglects the advection in the CMZ. Observations of emission lines at the foot-point of the Fermi-Bubbles have shown outflows from the CMZ [40]. The effect of the advection on the CR dynamics has been included in the model by Scherer *et al.* [111], but no clear impact on the gamma-ray emission structure has been found. In general an advection pointing away from the disk can help to extend the emission to higher latitudes and break the strong confinement in the magnetic field structures in the strongly anisotropic simulations. Therefore, this effect has to be incorporated in future work, although it is complicated to derive a fully three-dimensional model for the advection velocities.

Further observations of the CMZ will help to improve our knowledge of this complex region. The combination of different observation techniques and wavelengths will be crucial in the future to improve the modeling. Measurements of masers will help to constrain the LOS position for the clouds [108]. This will not only have an imprint on the magnetic field configuration but also improve the density estimations of the clouds.

Chapter 5

Galactic diffuse emission

This chapter discusses the diffuse emission from Galactic Cosmic Rays (GCRs) within the Milky Way. Those GCRs are accelerated at local sources in the Galaxy, travel through interstellar space, and interact with the ambient matter and photon fields leading to non-thermal emission. For a realistic description of the diffuse gamma-ray emission a detailed knowledge of the underlying CR transport process is needed.

The chapter starts with a summary of the state-of-the-art observations of the non-thermal emission in section 5.1 including the observations from the Galactic plane in gamma-ray and neutrinos. Section 5.2 discusses different models for the Galactic magnetic Field (GMF), which can influence the CR propagation. In section 5.3 the diffusion process of CRs within the Milky Way is summarized. Within this section, a realistic diffusion coefficient for the CRs is derived. First a CR transport model including wave-particle interactions and the excitation of waves by the CRs themselves is introduced (section 5.3.1). This model is then fitted to the CR observations at Earth (section 5.3.2) and the derived diffusion coefficient is applied to the escape of CRs from the Milky Way (section 5.3.3) demonstrating the influence of the GMF. Afterward in section 5.4 the Galactic diffuse emission is estimated based on the diffusion parameters inferred before and the influence of the anisotropy in the CR diffusion is shown. The results' final summary and critical discussion are presented in section 5.5.

5.1   Observation

Diffuse emissions originating from non-thermal particles in the Galaxy can be observed in multiple wavelengths and even with different messengers like neutrinos. Observation in the radio wavelength mainly traces the distribution of GCR electrons, while the X-ray and gamma-ray observations do not allow an easy association with a primary species. In these higher energies, electrons can contribute via Inverse Compton Scattering and relativistic bremsstrahlung while protons and higher nuclei undergo inelastic interactions leading to the production of neutral pions, which subsequently decay into gamma rays. A clear indication of the hadronic origin of the non-thermal emission is the observation of neutrinos originating from the decay
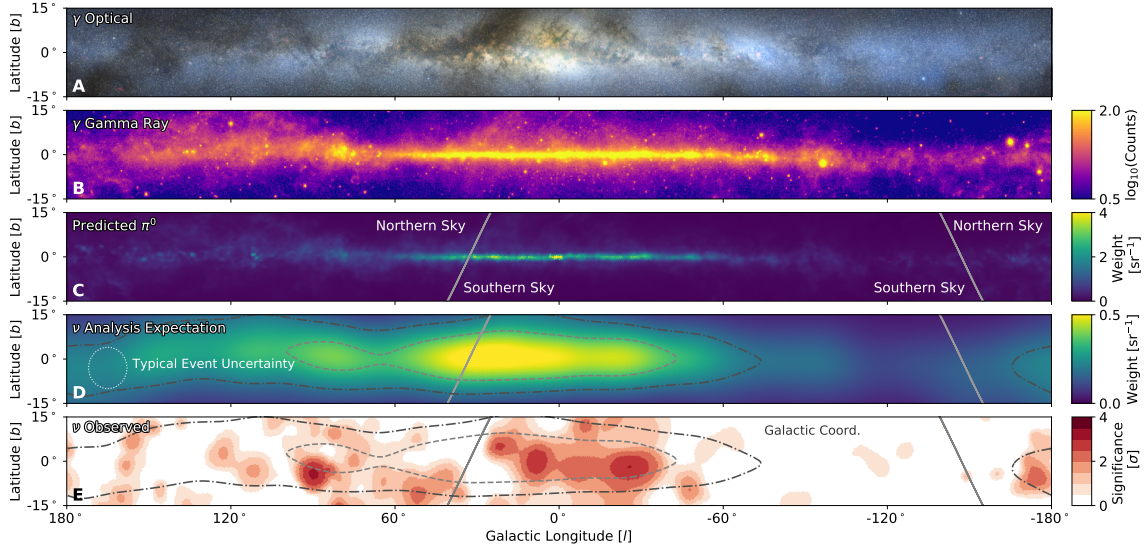
Figure 5.1. Multi-messenger view on the Galactic plane. (A) Optical light, which is partly absorbed from gas clouds. (B) Integrated gamma-ray flux observed with the Fermi-LAT using 12 years of data. (C) Predicted gamma-ray emission from π^0 decays. (D) Expected neutrino emission based on the gamma-ray template and the angular resolution of IceCube. (E) Significance map for neutrino observations with IceCube. Figure taken from [4].

of charged pions produced in the inelastic interactions[1].

Figure 5.1 shows the observations of the Galactic plane in optical light (panel A), integrated gamma ray counts (panel B), and neutrinos (panel E), where the total flux consists of the point sources and the diffuse component. Observation in the gamma-ray regime allows for discrimination between the diffuse interstellar component and the contribution from point sources or extended source regions. The *Large Area Telescope* onboard the *Fermi* satellite scans the full sky every three hours in a wide energy range (20 MeV – > 300 GeV) [29]. Observations of the Galactic plane have also been performed with imaging air Cherenkov telescopes. A major survey is done by the H.E.S.S. telescopes [6] covering energies between 0.2 and 100 TeV. At the highest energies ($> 100\,\mathrm{TeV}$) the *Large High Altitude Air Shower Observatory* (LHASSO) has reported diffuse emission from the inner ($15° \leq l \leq 125°, |b| \leq 5°$) and outer ($125° \leq l \leq 235°, |b| \leq 5°$) Galactic plane [42].

5.2   Galactic magnetic field

Spiral galaxies like our Milky Way often have a magnetic field that can affect the evolution of the galaxy and the dynamics of the low-energy Galactic cosmic rays (see [32] for a review). It can be decomposed into a large-scale coherent component,

---

[1]In principle also leptonic scenarios can produce neutrinos. In this scenario a very high-energy synchrotron photon scatters on an X-ray photon from a target photon field producing a muon antimuon pair ($\gamma + \gamma_{\mathrm{bgr}} \rightarrow \mu + \mu^-$). This interaction is discussed in the context of Active Galactic Nuclei [66], but the Milky Way does not provide a high-energy photon target, that would be required for such a process.

the so-called Galactic magnetic Field (GMF), and the turbulent component. Determining the structure of the GMF in the Milky Way is particularly complex as the only available observing position lies within the Galaxy.

Several attempts have been made to develop a model for the GMF. One of the first realistic models is the one by Jansson & Farrar [69] (hereafter JF12), which is widely used in cosmic-ray physics. It uses the *WMAP* measurements of the Galactic synchrotron emission as well as extragalactic rotation measures. The JF12 model consists of a Galactic disc, a toroidal halo, and an X-shaped out-of-plane component for the regular GMF. Besides this regular component, the JF12 model also covers the turbulent one. The central kiloparsec of the Milky Way has been excluded in the JF12 model.

After the original publication of the JF12 model, several attempts have been made to improve it. In [12] it has been refitted to the polarized synchrotron and dust emission measurements by the *Planck* satellite. In this updated version the turbulent component is reduced and the field strength in some spiral arms has been changed. The other components have only minor differences to the original model.

The poloidal X-shape and the spiral disc component of the original JF12 model contain regions in which the divergence constraint is violated. The authors of [77] propose a smoothing for the X-shape poloidal field within the Galactic disc to address this problem. Here one has to note, that this fully solenoidal improved model has not been refitted to the observational data. The authors tried to keep all changes as minimal as possible, but a readjustment of the parameters would be needed [77].

A new fit of the divergence-free parametric functions to the available data from *WMAP* and the *Planck* satellite has been presented in [125] (hereafter UF23). The authors account for the uncertainty in the density of thermal and CR electrons leading to a suite of models for the GMF. They derive eight models in which different functional forms, data products, and input models have been used. All of these eight models are compatible with the available radio data.

In Figure 5.2 a set of field lines for the original JF12 field, all UF23 models, and the superposition of the magnetic field in the Central Molecular Zone (see section 4.2 for a detailed discussion) with the solenoidal improved JF12 field are shown. The superposition is needed to fill the missing central component in the JF12 model.

Besides the different structural features, two main differences between the fields based on the JF12 model and the UF23 models can be seen. First, the JF12 model has a strong asymmetry between the northern and southern hemispheres originating from the toroidal halo component, while the UF23 models are nearly symmetric. Second, the average strength of the disc component in the inner Galaxy is much stronger in the UF23 models compared to the JF12.

5.3 Diffusion of Cosmic Rays in the Milky Way

5.3.1 Cosmic Ray scattering on self-excited waves

The diffusion of CRs is typically based on scattering with magnetic field fluctuation of external turbulence, driven e.g. by supernova explosions. CRs can excite additional waves by the so-called streaming instability if a spatial gradient in the CR
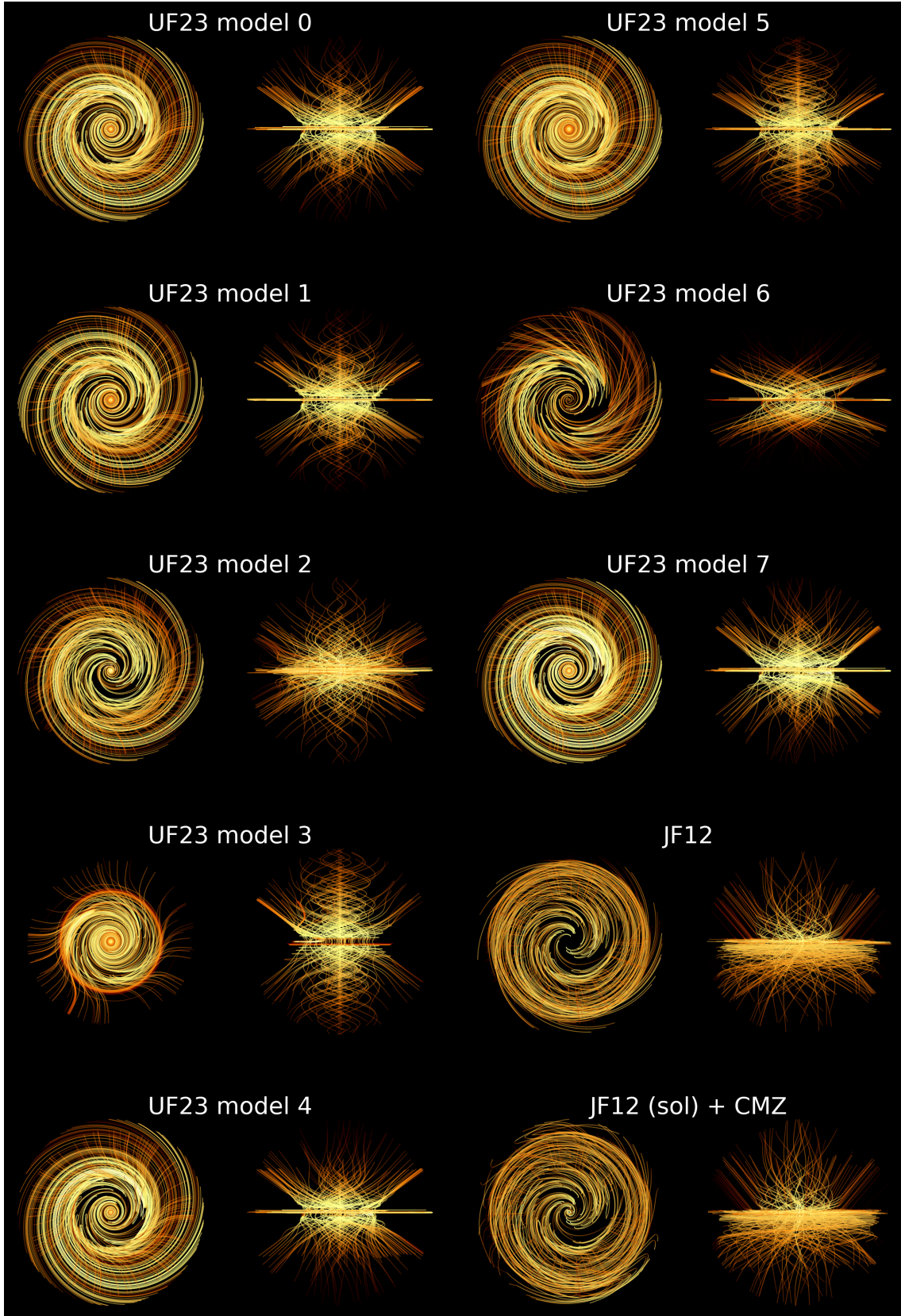
Figure 5.2. Field lines in different magnetic field models of the Milky Way. All field lines are shown in the same color scaling in a logarithmic scale. The counting of the models by Unger & Farrar [125] is based on the implementation in CRPropa. JF12 is the model by Jansson & Farrar [69]. The magnetic field in the lower right corner is the superposition of the solenoidal improved JF12 field by [77] and the magnetic field in the Central Molecular Zone by [62].

distribution is present. In the following, a realistic diffusion coefficient for the Milky Way is estimated by extending the work from [21, 38]. The derivation is based on the one-dimensional flux-tube approximation, in which the diffusion perpendicular to the magnetic field line is neglected, and only the CR diffusion perpendicular to the Galactic plane is considered. In this case, the steady-state transport equation for the phase-space density $f = f(p, z)$, normalized to the total number of particles $N = \int f(p, z) \, dp \, dz$, reads as

$$-\frac{\partial}{\partial z}\left[D\frac{\partial f}{\partial z}\right] + v_\mathrm{A}\frac{\partial f}{\partial z} - \frac{dv_\mathrm{A}}{dz}\frac{p}{3}\frac{\partial f}{\partial p} = q_\mathrm{CR}(p, z) = q_0(p)\delta(z) \quad . \tag{5.1}$$

Here it is assumed that all particles are injected with a power-law spectrum $q_0(p) = \mathcal{A}\left(p/m_p c^2\right)^{-\alpha}$ at the position $z = 0$. The normalization $\mathcal{A}$ of the source spectrum depends on the assumption of the source class and includes several free parameters. Blasi et al. [38] assume the acceleration of CRs to happen in supernova (SN) remnants. In this case, the normalization depends on the average total kinetic energy of an SN, E_SN, the fraction of energy transferred into accelerated particles, ξ_CR, the SN rate $\mathcal{R}_\mathrm{SN}$ and the physical extent of the SN remnant, R_d. These parameters are strongly correlated and can not be constrained independently within this model. Therefore the absolute normalization $\mathcal{A}$ is kept as a single free parameter. This allows us to interpret the results also in the case of other acceleration mechanisms, like pulsar wind nebula, compact star clusters, or magnetic reconnection events, as long as they are leading to a power law in momentum space.

For simplicity, we assume the spatial diffusion coefficient $D(p)$ to be independent of the position z and the Alfvén wave speed to be constant above and below the disc but directed away from it. In this case, the gradient in the Alfvén speed follows as $dv_A/dz = 2v_A\delta(z)$. This simplification, is chosen to allow an analytical solution of this equation. Armillotta *et al.* [28] have shown, that the Alfvén speed strongly varies in different gas phases and the CR transport for mildly realativistic particles ($E \lesssim 1\,\mathrm{GeV}$) will be different in different places within the Milky Way. In this work the focus lies on the transport of strongly relativistic particles ($E \gtrsim 10\,\mathrm{GeV}$) which are unaffected from the advection [34].

Introducing a free escape boundary condition $f(z = \pm H) = 0$ offers the analytical solution

$$f(z, p) = f_0(p)\frac{1 - e^{-\zeta(1-|z|/H)}}{1 - e^{-\zeta}}, \quad \text{with} \quad \zeta(p) \equiv \frac{v_\mathrm{A} H}{D(p)} \quad . \tag{5.2}$$

The full solution, including the momentum dependence $f_0(p)$ can be found after integrating Eq. (5.1) in the range $0^- \leq z \leq 0^+$. The implicit solution at the position $z = 0$ follows as

$$f(p, z = 0) = \frac{3}{2v_A}\int_p^\infty \frac{dp'' \, q_0(p'')}{p''}\exp\left[\int_p^{p''}\frac{3\,dp'}{p'\left(1 - \exp\left[\zeta(p)\right]\right)}\right] \quad . \tag{5.3}$$

The diffusion coefficient $D(p)$ can be derived from the wave power spectrum $W(k)$ of the turbulent fluctuations. The absolute normalization of the wave spectrum is given by the turbulence level

$$\eta = \frac{\delta B^2}{B_0^2} = \int_{k_0}^\infty dk \, W(k) \quad . \tag{5.4}$$

Here, δB is the turbulent part and B_0 is the regular part of the Galactic magnetic field, and $k_0 = 1/l_{\mathrm{max}} = 1/(50\,\mathrm{pc})$ is the injection scale of the turbulence. Assuming a small turbulence level $\eta \ll 1$ and resonant interactions at $k = 1/r_L$ the parallel diffusion coefficient can be followed as

$$D(p) = \frac{r_L\, v}{3\, k\, W(k)} \quad, \tag{5.5}$$

where r_L denotes the gyro radius of the particles and $v = v(p)$ is their speed [115]. To calculate the growth rate of the streaming instability Γ_{CR} we average the expression given by [118] over the pitch-angle. It reads as

$$\Gamma_{\mathrm{CR}}(k) = \frac{16\pi^2}{3} \frac{v_A}{kW(k)B_0^2} \left[p^4 v(p) \frac{\partial f}{\partial z} \right]_{p=qB_0/kc} \quad. \tag{5.6}$$

The excited waves undergo wave-wave interactions leading to diffusion in k-space [83, 131] and the evolution of the wave spectrum is described by

$$-\frac{\partial}{\partial k}\left[D_{kk} \frac{\partial W}{\partial k} \right] + \Gamma_{\mathrm{CR}}W = q_W(k) \quad. \tag{5.7}$$

The wave diffusion coefficient can be written as [91, 131]:

$$D_{kk} = C_k v_A k^{\alpha_1} W(k)^{\alpha_2} \tag{5.8}$$

where $C_K \approx 5.2 \cdot 10^{-2}$ is the Kolmogorov constant [21] and $(\alpha_1, \alpha_2) = (7/2, 1/2)$ corresponds to a *Kolmogorov*-like turbulence. Assuming a mono-chromatic injection of the external turbulence $q_W(k) \propto \eta \delta(k - k_0)$ at the injection scale k_0 one can derive the implicit solution

$$W(k) = \left[\left(-\frac{1+\alpha_2}{C_K v_A} \int_k^\infty \frac{\mathrm{d}k'}{k'^{\alpha_1}} \int_{k_0}^{k'} \mathrm{d}k'' \Gamma_{\mathrm{CR}}(k'')W(k'') \right) + \left(c_3 k^{1-\alpha_1} \right) \right]^{\frac{1}{1+\alpha_2}} \quad. \tag{5.9}$$

The integration constant c_3 is determined by the turbulence level η of the external turbulence by $c_3 = W_0^{1+\alpha_2} k_0^s$ with $W_0 = (s-1)\eta/k_0$ and $s = (\alpha_1 - 1)/(\alpha_2 + 1) = 5/3$ for the *Kolmogorov*-like turbulence.

To solve the coupled system of the CR distribution in Eq. (5.3) and the wave spectrum in Eq. (5.9) an iterative approach is used. The starting conditions are given by the external turbulence $W_{i=0}(k) = W_0\,(k/k_0)^{-s}$ and the distribution function $f_{i=0}(p) = q_0(p)\,H/(2D(p))$. This process is continued until convergence is reached and the maximal relative change in the distribution function $\Delta f = \max_p \{f_i(p)/f_{i-1}(p)\}$ and the wave spectrum $\Delta W = \max_k \{W_i(k)/W_{i-1}(k)\}$ is less than 0.5 %.

5.3.2 Fitting the Cosmic Ray spectrum

A power law well describes the CR spectrum observed at Earth, but it reveals several breaks in the spectral slope (see [34] for a review). For most of these breaks, it is unclear whether they are already present in the emitted source spectrum or if a transport effect between the source region and the observer causes them. For the

break at several hundred GV rigidity, called the *cosmic-ray hip*, there are clear hints from the ratio between primary and secondary CR species, that it is caused by a transport effect. A possible explanation is the streaming instability discussed before.

To estimate the effective diffusion coefficient causing this break we tune the free parameters within the previously introduced model to match the CR proton data observed by CALET [14]. In the highest energies ($E > 1\,\mathrm{TeV}$) the data show an energy scaling $dN/dE \propto E^{-\Gamma}$ with $\Gamma = 2.56$. Assuming a *Kolmogorov*-like diffusion coefficient with $D \propto E^{1/3}$ the injection slope for the phase-space density should be $\alpha = 2 + \Gamma + 1/3 \approx 4.25$, based on a *leaky-box approximation* (see [34] for more details). In the fitting procedure this value is fixed together with the halo height $H = 4\,\mathrm{kpc}$ and the injection scale $k_0^{-1} = 50\,\mathrm{pc}$ of the external turbulence. In Tab. 5.1 the final results for the fitting parameters and fixed values are summarized.

Parameter	unit	value
Alfvén speed v_A	$\mathrm{cm\,s^{-1}}$	$2.45 \cdot 10^6$
Halo height H	kpc	**4***
Turbulence level η	–	0.027
Injection scale k_0^{-1}	pc	**50***
Background field B_0	$\mu\mathrm{G}$	1.58
Injection norm $\mathcal{A}$	$\mathrm{cm^{-5}\,g^{-3}\,s^2}$	$9.3 \cdot 10^{35}$
Injection slope α	–	**4.25***

Table 5.1

Fitting parameter for the streaming instability model. Parameters marked in **bold*** are fixed in the fit.

In Figure 5.3 the resulting spectrum of the CRs at Earth is shown and compared to the measurements by AMS-02 [16], PAMELA [15], DAMPE [26], CALET [14] and ISS-CREAM [44]. Although the model has only been fitted to the data from CALET, which are in the energy range $E > 50\,\mathrm{GeV}$, it is in reasonable agreement with the data from AMS and PAMELA at lower energies and DAMPE and ISS-CREAM at higher energies. The total hardening in the CALET data is not fully reproduced within the model, but all differences are within the observational uncertainty of the measurement.

Along with the resulting CR distribution function, the wave power spectrum $W(k)$ is estimated in the streaming instability model. Using the optimal fitting parameters as listed in table 5.1 the diffusion coefficient can be calculated following Eq. (5.5). In Figure 5.4 this diffusion coefficient is plotted as a function of the kinetic energy of the proton. In the highest energies, it follows the expected $D \propto E^{1/3}$ scaling for *Kolmogorov*-like turbulence. In the energies below 1 TeV, the streaming instability leads to a stronger energy dependence. At the lowest energies, the break due to a transition from relativistic to non-relativistic energies can be seen.

For the non-thermal gamma-ray emission in the Milky Way, the energies $E > 10$
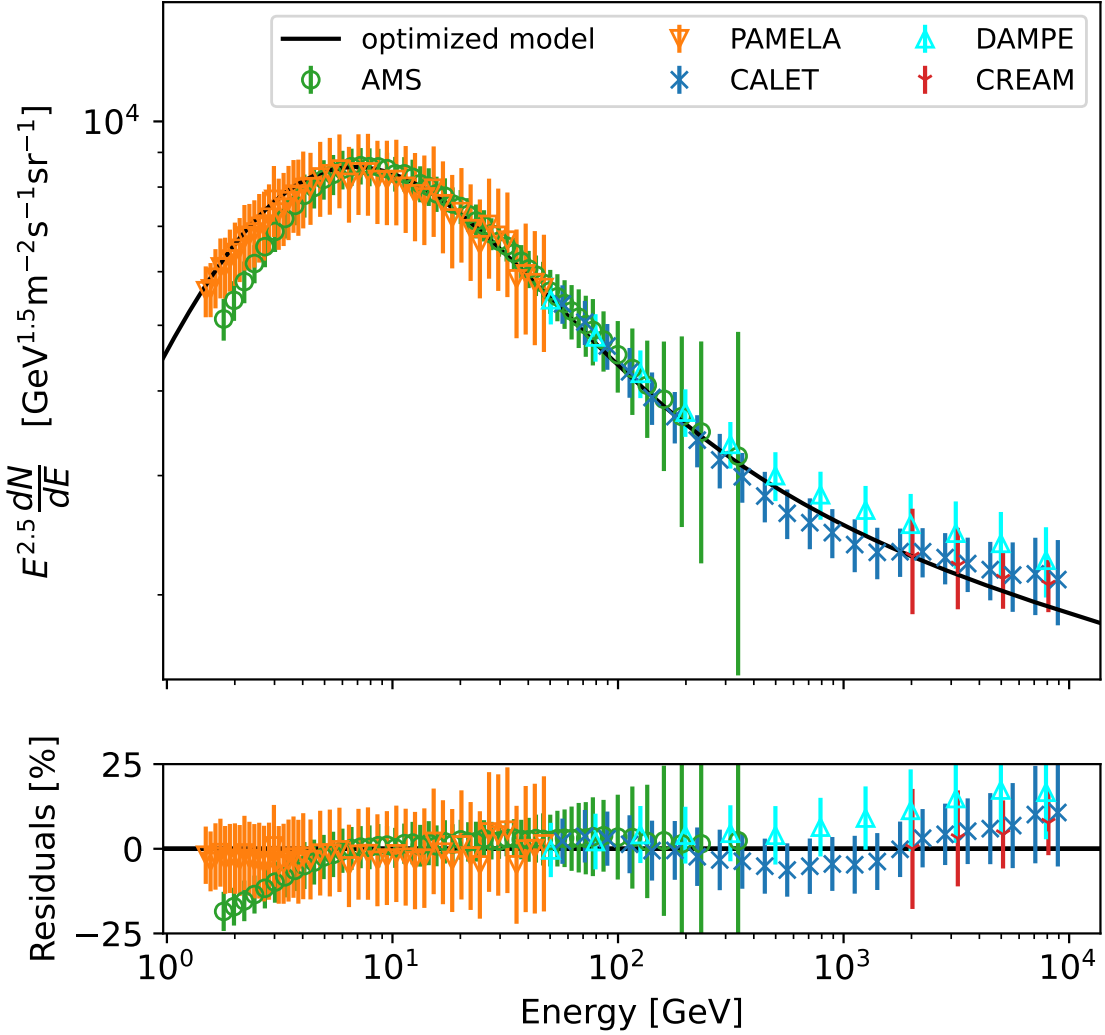
Figure 5.3. Particle spectrum from the streaming instability model fitted to the dataset from CALET [14]. Additionally the data from AMS-02 [16], PAMELA [15], DAMPE [26] and CREAM [44] are shown. The datasets from AMS-02 and PAMELA have been corrected for the Solar modulation with a force field approximation using the potential given in the corresponding reference. All error bars show the sum of the statistical and the systematic uncertainty.
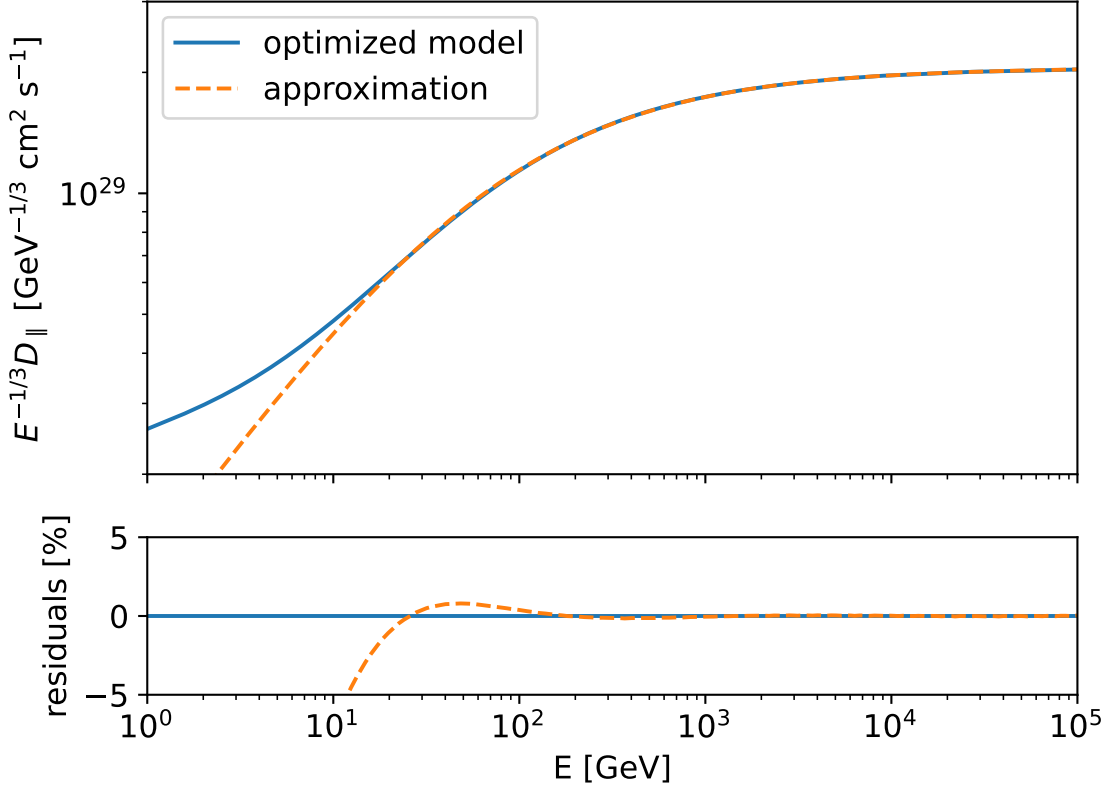
Figure 5.4. Energy weighted diffusion coefficient corresponding to the optimized model of the streaming instability as shown in Figure 5.3. The fit follows Eq. (5.10) and the parameters are listed in table 5.2.

GeV are of particular interest. To incorporate the effect of the streaming instability into a more advanced three-dimensional model based on CRPropa, we approximate the diffusion coefficient in the high energy regime ($E > 10\,$GeV) with a smoothly broken power-law given by

$$D(E) = D_0 \left(\frac{E}{E_{br}} \right)^{\gamma_1} \cdot \left(1 + \left(\frac{E}{E_{br}} \right)^{\gamma_2 - \gamma_1} \right)^{-1} \quad , \tag{5.10}$$

with a break energy E_{br}. The parameters for the approximation are summarized in table 5.2.

5.3.3 Escape of Cosmic Rays from the Milky Way

The model of the streaming instability discussed before only refers to the parallel diffusion coefficient in a one-dimensional flux-tube approximation. To include the perpendicular transport a scaling relation between the parallel diffusion $\kappa_\parallel = D$ and perpendicular diffusion $\kappa_\perp$ is assumed. Here, a constant scaling factor $\epsilon = \kappa_\perp / \kappa_\parallel$ is tested. As a baseline scenario the superposition of the solenoidal improved version of the JF12 magnetic field [77] and the intercloud component from the field of the Central Molecular Zone [62] is used.

parameter	$D_0/(10^{29}\,\mathrm{cm^2\,s^{-1}})$	E_{br}/GeV	γ_1	γ_2
value	8.091 ± 0.008	64.38 ± 0.11	0.33529 ± 0.00007	-0.3209 ± 0.0007

Table 5.2

Parameters for the approximation of the diffusion coefficient in Figure 5.4 with
the smoothly broken power-law following Eq. (5.10).

Parameter	unit	low	medium	high
minimum energy $E_{\min}$	GeV	0.1	10^2	10^5
maximum energy $E_{\max}$	GeV	10^2	10^5	10^7
time step ΔT	kpc/c	2000	10	1
maximal time $T_{\max}$	Gpc/c	50	1	1

Table 5.3

Simulation parameter for the low, medium, and high energy run of the escape
time estimation. The other parameters are the same in all runs (see text).

To quantify the effect of the perpendicular diffusion the escape times for CRs
from the Milky Way are analysed. Therefore, we simulate 10^6 particles for each
anisotropy $\epsilon \in \{10^{-3}, 10^{-2}, 10^{-1}, 10^0\}$ in three energy ranges. The energy distribu-
tion of the particles is uniform in $\log(E)$ between minimum and maximum energy
(see table 5.3). The starting position of each particle is sampled from the pulsar dis-
tribution [37]. The outer boundary of the simulation volume is defined by a cylinder
with a half height $H = 4\,\mathrm{kpc}$ and a radius $R = 20\,\mathrm{kpc}$. All particles reaching the
boundary are lost into the intergalactic medium. After a fixed time step ΔT the
positions of all particles within the simulation volume are stored until the maximum
simulation time $T_{\max}$ is reached. The values for the time step and the maximum
simulation time differ between the low, medium, and high energy simulation and are
summarized in table 5.3. In all simulations the effect of energy losses is neglected as
the loss timescale is typically much longer than the CR escape. Assuming a particle
density of $n = 1\,\mathrm{cm^{-3}}$ for the Galactic disc the loss timescale exceeds $\tau_{\mathrm{loss}} \gtrsim 10^2\,\mathrm{Myr}$.
As the CRs spend most of the time within the Galactic halo the effective average
particle density will be reduced by several orders of magnitude. The final simula-
tion results of the escape times indicates that this assumption of a thin target in the
Milky Way is valid for particles with $E > 10\,\mathrm{GeV}$ or $\epsilon > 10^{-2}$. In the case of the
lowest energies additional escape via advection might become dominant, that is not
included in the model, and the assumption of a thin target might stay valid as well.

After the simulation the particles are divided into 80 logarithmic energy bins
between $0.1\,\mathrm{GeV}$ and $10\,\mathrm{PeV}$. In each energy bin and time step, the number of
particles inside the simulation volume is calculated. Figure 5.5 shows an example
for the escape of particles with an energy $E \approx 6\,\mathrm{GeV}$. Here, the two most extreme
values for the anisotropy of the diffusion $\epsilon = 10^{-3}$ and $\epsilon = 1$ are shown. After a short
initial phase, an exponential decrease in the number of particles inside the Galaxy
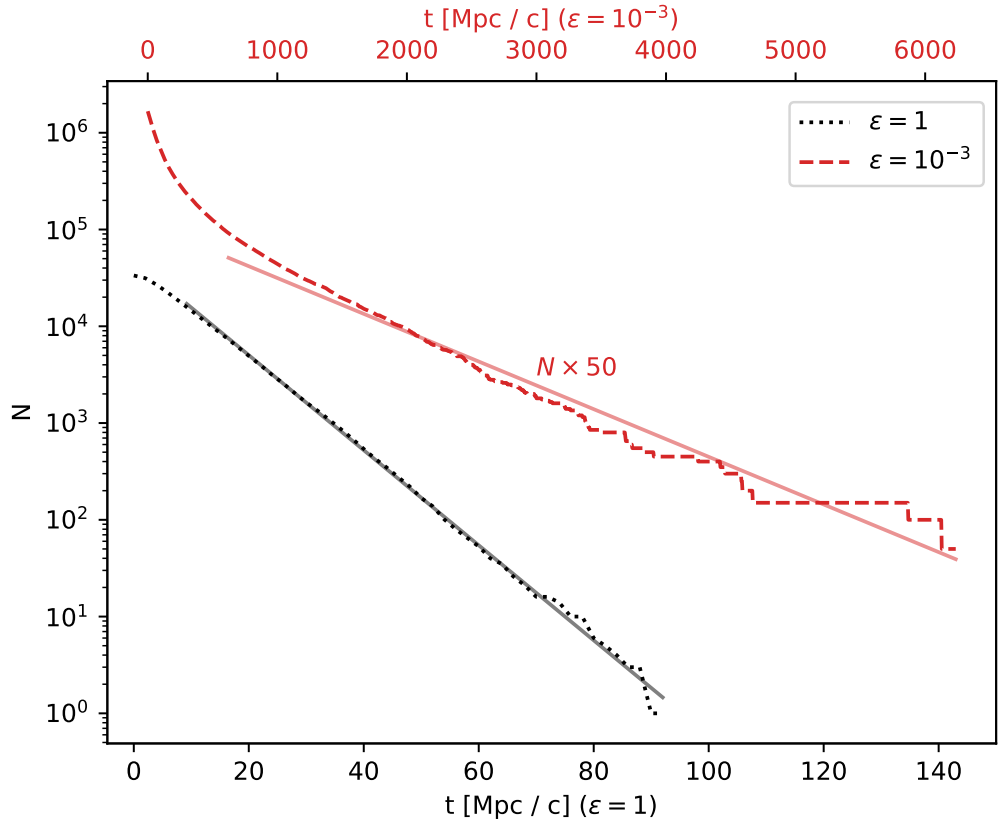
Figure 5.5.   Number of particles left in the simulation volume for different anisotropies of the diffusion tensor. In the anisotropic case ($\epsilon = 10^{-3}$) the perpendicular diffusion is reduced compared to the isotropic case ($\epsilon = 1$). Here, the data for GCRs with $E \approx 6\,\mathrm{GeV}$ in the combined magnetic field of [77] and [62] are shown. The solid lines indicate the fitted exponential decrease. Note, that the escape for the simulation is plotted with different time axes ($\epsilon = 1$ at the bottom, $\epsilon = 10^{-3}$ at the top). For better visibility the red lines are scaled up by a factor 50.

can be seen ($N \propto \exp\{-t/\tau\}$). To estimate the escape time τ the slope of the linear tail in the log-linear plot is fitted (solid lines). In the fit all times $T \leq 0.1\,T_{\mathrm{max,sim}}$, where $T_{\mathrm{max,sim}}$ is the maximum time of the simulation at which a particle is still in the simulation volume, are excluded. The solid lines in Figure 5.5 show the fitted exponential decrease in the allowed fitting range.

Figure 5.6 shows the simulated escape time of GCRs from the Milky Way as a function of the particle energy. The simulated values are compared with the analytical prediction for a one-dimensional escape $\tau_{\mathrm{esc}} = H^2/D(E)$. In the left panel of Figure 5.6 the prediction lines are calculated with the halo height of $H = 4\,\mathrm{kpc}$ and the perpendicular diffusion coefficient $D_\perp = \epsilon D_\parallel$. In the case of isotropic diffusion ($\epsilon = 1$), the simulated escape time is in good agreement with the prediction. For all cases of anisotropic transport ($\epsilon < 1$), the predicted escape time from the perpendicular diffusion is longer than the simulated. This shows that the escape of the particles is not only due to the perpendicular transport. If the escape would
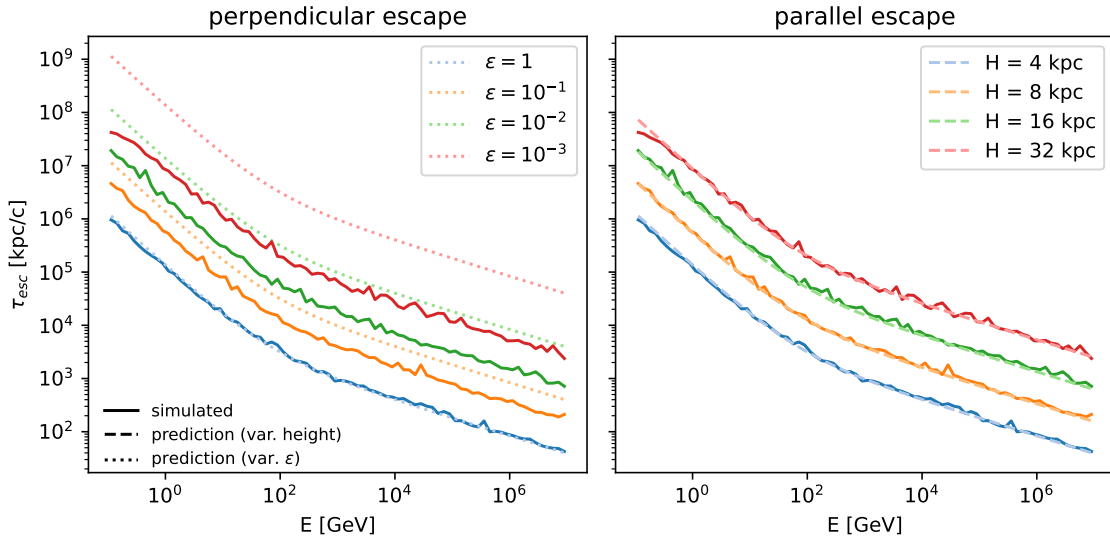
Figure 5.6. Simulated escape time of GCRs from the Milky Way for different anisotropies (solid lines) compared with the expectation from the purely perpendicular escape (left panel) and the purely parallel escape with larger scale height (right panel). The simulated lines in both panels are the same.

only be dominated by the parallel diffusion, no difference between the anisotropies would be expected, which is not the case. Therefore a mixture of parallel and perpendicular transport leads to the escape of CRs from the Milky Way. For a complex, realistic model of the GMF, it is not possible to quantify the impact of the transport directions beforehand. The escape times shown here are a galactic average over the magnetic field structure and the importance of the parallel and the perpendicular diffusion is influenced by the angle between the local magnetic field line and the Galactic plane. Additionally, in the case of strong parallel diffusion and magnetic field lines, which are mainly in the Galactic plane, the escape through the radial boundary of the Milky Way is also possible.

In order to understand the effect of the anisotropy parameter in a given magnetic field configuration on the escape time of CRs, one can compare the effective halo height H'. The effective halo height corresponds to a Galactic halo in the isotropic diffusion, which would lead to the same escape time. The right panel of Figure 5.6 shows this comparison of the simulated escape times, and the prediction from a larger effective halo. This comparison can be used to interpret results from isotropic simulations with larger halos in the case of anisotropic diffusion. Here one has to note, that this comparison is only possible on the Galactic average like the CR spectrum observed at Earth, but is not valid for small-scale structures in the CR distribution and the corresponding non-thermal emission signatures. For the baseline magnetic field configuration, the effective halo height can be approximated as

$$H' = H\epsilon^{-0.3} \propto \tau_{\text{esc}}^{0.5} \quad . \tag{5.11}$$

This scaling of the effective halo height and the anisotropy depends on the magnetic field configuration. Figure 5.7 shows the escape time at different energies and anisotropies of the diffusion tensor in different GMF models. In the case of the

isotropic diffusion ($\epsilon = 1$), the escape times are the same for all GMF models at a given energy, as it is expected. With stronger anisotropy ($\epsilon < 1$) the escape times start to deviate between the GMF models. In the intermediate anisotropies ($\epsilon = 10^{-1}$ or $\epsilon = 10^{-2}$) the baseline JF12 model results in the shortest escape times. For the anisotropies $\epsilon \leq 10^{-2}$ the spread between the GMF models reaches up to one order of magnitude. In the case of nearly parallel diffusion ($\epsilon = 10^{-3}$), some GMF models from [125] lead to escape times even shorter than the baseline GMF model. In general, the different models presented by [125] can be grouped in two cases depending on the escape time. From the scaling of the escape time with the anisotropy parameter and its deviation from a power-law towards the strongest anisotropy one can see the effect of the escape at the radial boundary via the parallel transport on field lines within the Galactic plane. This transport defines the saturation limit for $\kappa_\perp \to 0$.

Differences in the average escape time of Galactic CRs imply the possibility of identifying transport properties with the produced secondary non-thermal emission. Furthermore, it highlights the opportunity to use gamma-ray measurements to further constrain the GMF models.

5.4 The Gamma Ray and Neutrino Sky

Modeling the all-sky gamma-ray and neutrino emission requires a detailed description of the underlying CR distribution. Using CRPropa to model the Galactic CR distribution would in principle allow a direct sample of the secondary gamma rays and neutrinos as described in the hadronic interaction module (see section 3.2) and done for the Central Molecular Zone (see chapter 4), but this would require an intense amount of computation power. Assuming a 1 TeV CR, that would stay about $\tau = 5 \cdot 10^2$ Myr in the Galaxy (see Figure 5.7 with an anisotropy of $\epsilon = 10^{-3}$) we can calculate the average number of interactions for this particle as

$$N_{\text{int}} \approx c\,\tau\,n_{\text{H}}\,\sigma_{pp} \quad . \tag{5.12}$$

For the propagation of a GCR in the galactic halo we can assume an average target density of $n_{\text{H}} = 0.01\,\text{cm}^{-3}$ and a cross section of the order of $\sigma_{pp} \sim 10^{-26}\,\text{cm}^2$. This results in $N_{\text{int}} \sim 0.05$ interaction per primary cosmic ray. To achieve a reasonable resolution on the sky in total $N_{\text{pix,sky}} \sim 2 \cdot 10^5$ pixel would be needed. Together with an energy resolution of $N_{\text{pix,E}} = 80$ a total amount of $N_{\text{primary}} \gtrsim 3 \cdot 10^8$ would be required. If one takes the shorter escape times for isotropic diffusion or higher energetic particles into account, the total number of particles that would be needed to simulate can go up to $\gtrsim 10^{10}$, which is not feasible. Therefore alternative methods using a line-of-sight (LOS) integration are needed.

5.4.1 Line-of-sight Integration Method

Calculating the high-energy non-thermal emission in the Galaxy from a given CR distribution can be done by the LOS integration. One useful tool to solve this is the HERMES package [50], in which the differential intensity for any direction (l, b) is
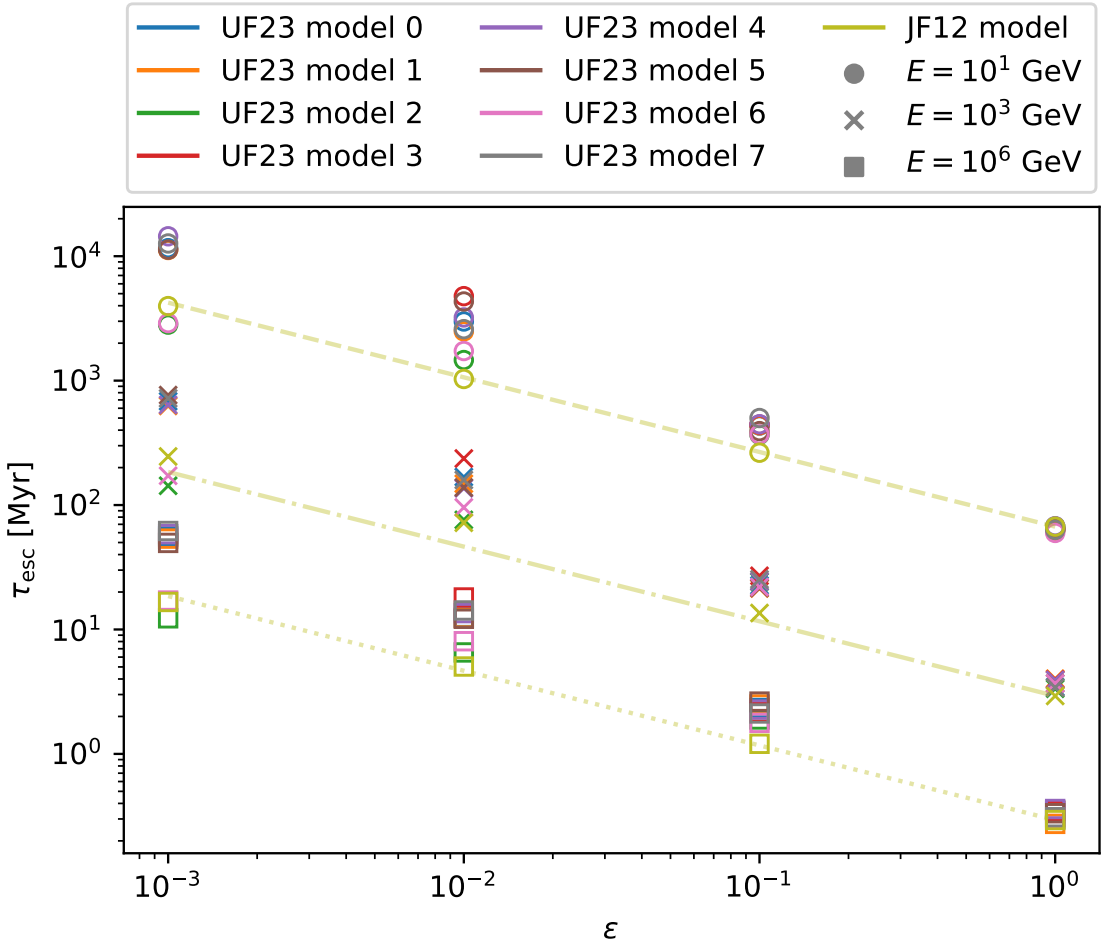
Figure 5.7. Escape time of CRs in the Milky Way in different models of the GMF with anisotropic diffusion. The marker denotes the energy of the CR while the color shows the GMF model. Here UF23 refers to the models from [125] and JF12 is the baseline magnetic field as described in the text. The lines show the expected scaling in the baseline GMF model as defined in relation (5.11).

calculated as

$$I_x(E_j, l, b) = \frac{1}{4\pi} \int\limits_0^\infty \mathrm{d}s \, \epsilon_x(E_j, \vec{r}) \quad . \tag{5.13}$$

Here, the direction (l, b) is the galactic longitude and latitude, respectively, $\epsilon_x(\vec{r})$ is the local emissivity of a process x, and s denotes the distance along the LOS. The intensity can be calculated for all gamma-ray $(j = \gamma)$ or neutrino $(j = \nu)$ energies.

The sky positions (l, b) are given in a spherical coordinate system centered on the Sun. It can be converted to the cartesian coordinate system centered at the galactic center $\vec{r} = (x, y, z)$ by

$$x = s \cos l \cos b - r_\odot \quad ; \quad y = s \sin l \cos b \quad ; \quad z = s \sin b \quad , \tag{5.14}$$

where $r_\odot$ is the distance between the Sun and the Galactic Center. The calculation of sky-maps is done with a Hierarchical Equal Area isoLatitude Pixelization (`HEALPIX`)

[61], which can be accessed in Python via the `healpy` package [132]. `HEALPIX` divides the sky into $N_{\text{pix}} = 12\,n_{\text{side}}^2$ pixels, where the resolution n_{side} is usually given in powers of two. In the context of this work, a resolution of $n_{\text{side}} = 128$ leading to an angular resolution of roughly $0.45°$ is used.

The `HERMES` package comes along with a set of implemented physical processes like Faraday rotation, free-free and synchrotron emission, inverse Compton scattering, relativistic bremsstrahlung, and dark matter annihilations. For this work, the gamma-ray and neutrino emission from the decay of neutral and charged pions (called `PiZeroIntegrator` in the code) is used. The emissivity of the pion channels is calculated as

$$\epsilon_\pi(E_\gamma, \vec{r}) = 4\pi\, n_H(\vec{r}) \int \mathrm{d}E_p\, \Phi_p(E_p, \vec{r}) \left(\frac{\mathrm{d}\sigma_{pp}}{\mathrm{d}E_\gamma} + f_{He} \frac{\mathrm{d}\sigma_{pHe}}{\mathrm{d}E_\gamma} \right) \quad . \tag{5.15}$$

Here, $n_H = n_{H_I} + 2\,n_{H_2}$ is the total nucleon number density, Φ_p is the differential flux of CR protons as a function of kinetic energy E_p and $\mathrm{d}\sigma_{p-i}$ is the differential cross section for the interaction of a proton with a target proton ($i = p$) or helium ($i = He$) leading to a gamma ray. The scaling factor $f_{He} = 0.1$ assumes a constant mixture of protons and helium within the ISM of the Galaxy. The cross-section for the gamma-ray production can be exchanged with the neutrino cross-section to calculate the neutrino emission.

The public version of the `HERMES` code relies on the measured gas column density N_H within several rings. The total gamma-ray emission from all rings can then be calculated as

$$I_\gamma(l, b, E_\gamma) = \frac{1}{4\pi} \sum_k N_H^k(l, b) \langle \epsilon_\pi(\vec{r}, E_\gamma) \rangle^k \quad , \tag{5.16}$$

where the average emissivity of the k-th ring

$$\langle \epsilon_\pi(\vec{r}, E_\gamma) \rangle^k = \frac{\int\limits_0^\infty \mathrm{d}s\, \epsilon_\pi(\vec{r}, E_\gamma)\, \rho_{HI}(\vec{r})\, H^k(\vec{r})}{\int\limits_0^\infty \mathrm{d}s\, \rho_{HI}(\vec{r})\, H^k(\vec{r})} \tag{5.17}$$

is used. The average is based on a smooth gas profile ρ_{HI} taken from the analytical fit of the model by [94] and H^k is the step-function, which is 1 inside the k-th ring and 0 outside.

In the context of this work, the code has been extended to directly solve eq. (5.15) with a fully three-dimensional gas distribution n_H, together with an interface to use the gas models implemented in CRPropa. Those cover simple test cases like a uniform gas and the analytical models by Nakanishi *et al.* [93, 94] and Ferriere *et al.* [53, 54] as well as a grid-based interface to use the distributions from Pohl *et al.* [102] or Mertsch *et al.* [89, 90].

5.4.2 Model of the Cosmic Ray Distribution in the Milky Way

The model of the three-dimensional distribution of CRs within the Milky Way follows the same setup as discussed for the escape of CRs in section 5.3.3. It is based on the

approximated diffusion coefficient from the streaming instability model and splits the simulated energy range into a low, medium, and high energy range (compare table 5.3). For the Galactic CR distribution, higher statistics are required. Therefore we ran in each energy regime a set of 30 simulations with $N_{\mathrm{sim}} = 10^7$ candidates each.

As a starting point the results in the base-line GMF model with the anisotropy parameters $\epsilon = 10^{-2}$ and $\epsilon = 1$ are used. Those setups can give a first hint on the prospects identifying the influence of the anisotropy in transport and the GMF configuration. A detailed set of simulations with all magnetic field models and more values for the anisotropy will be done in future work.

After the simulation, the particles are binned in $80 \times 80 \times 40$ spatial bins covering a range $-20\,\mathrm{kpc} \leq x, y \leq 20\,\mathrm{kpc}$ and $-4\,\mathrm{kpc} \leq z \leq 4\,\mathrm{kpc}$ and 80 energy bins with 10 bins per decade. The simulated source distribution

$$\left.\frac{\mathrm{d}N}{\mathrm{d}E}\right|_{\mathrm{sim}} = \frac{N_{\mathrm{sim}}}{E\,\log(E_{\mathrm{max}}/E_{\mathrm{min}})} \tag{5.18}$$

is reweighted to an injection spectrum

$$\left.\frac{\mathrm{d}N}{\mathrm{d}E}\right|_{\mathrm{s}} = \mathcal{A}\left(\frac{p}{m_p\,c^2}\right)^{-\alpha} \quad, \tag{5.19}$$

by assigning a weight

$$w_i = \frac{\mathrm{d}N/\mathrm{d}E|_{\mathrm{s}}}{\mathrm{d}N/\mathrm{d}E|_{\mathrm{sim}}} \cdot \Delta T \tag{5.20}$$

where p is the particle momentum and $\alpha = 2.25$ is the injection slope as used in the streaming instability model and ΔT is the simulation time step. The absolute normalization of the injection spectrum $\mathcal{A}$ is kept free to match the SED as observed at Earth. From the differential flux $J_{\mathrm{cr}}(E, \vec{r})$ at a given position in the Galaxy $\vec{r}$ in units particles per area per time per energy and per solid-angle the differential number density n_{cr} in an isotropic CR flux can be calculated as

$$n_{\mathrm{cr}}(E, \vec{r}) = \frac{4\pi}{c}\,J(E, \vec{r}) \quad. \tag{5.21}$$

This gives the input to the `HERMES` code to calculate the diffuse gamma-ray emission. The target gas distribution is the default H_I and H_2 ring model provided by Q. Remy (a detailed description is provided in the `HERMES` paper [50]). The cross section for the gamma-ray production is taken from the AAfrag model [71].

5.4.3   Results

Figure 5.8 shows the modeled CR-flux arriving at the outer heliosphere in the isotropic ($\epsilon = 1$) and anisotropic ($\epsilon = 10^{-2}$) diffusion model. The model for the diffusion coefficient is fitted to explain the CR-flux measurements by CALET [14] in the energy range between 50 GeV and 10 TeV (see section 5.3.2). In this energy range, a good agreement between the simulated CR flux and the observational data can be observed. At lower and higher energies the difference between the model
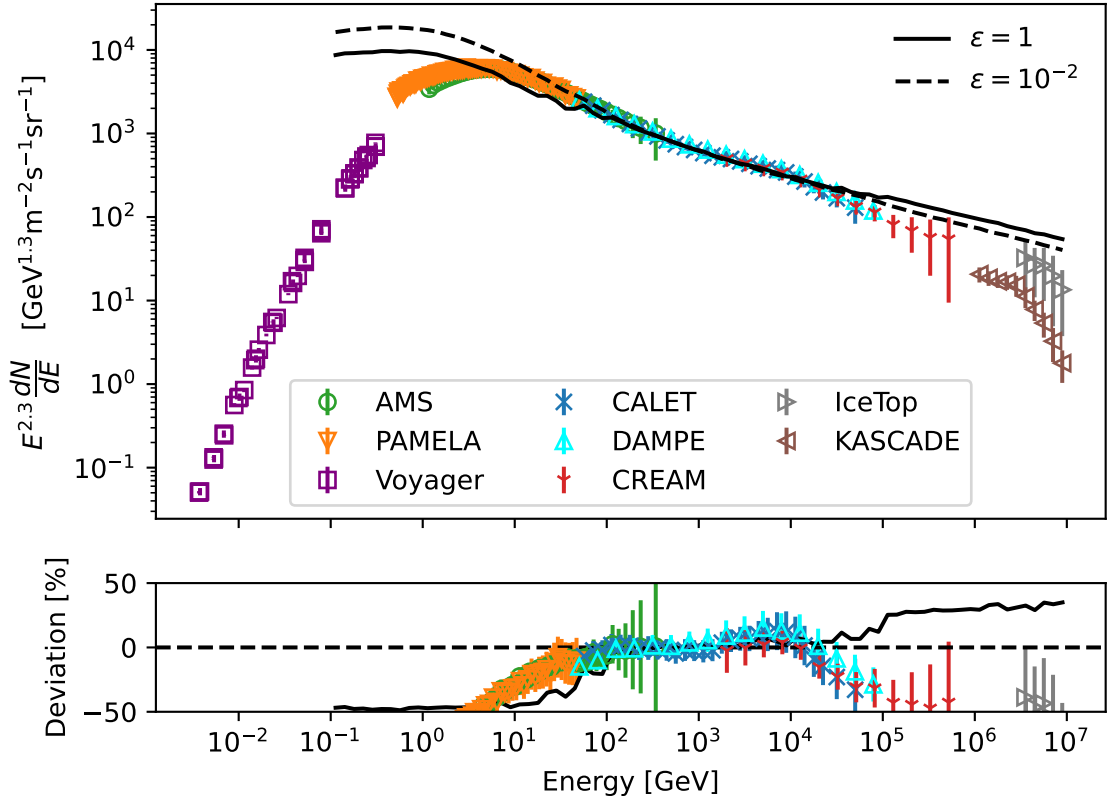
Figure 5.8. Cosmic Ray flux at the outer heliosphere. Additionally the data from the Voyager spacecrafts [45, 119, 120], AMS-02 [16], PAMELA [15], CALET [14], DAMPE [26], CREAM [44], IceTop [2] and KASKADE [27] are shown. The data from AMS and PAMELA are corrected for the heliospheric modulation. In the lower panel, the deviation of the data from the anisotropic model ($\epsilon = 10^{-2}$) is shown. The total deviation is limited to 50 % for better visibility.

prediction and the observations exceeds the shown deviation range of 50 %. This effect is somehow expected, as the source spectrum assumed here is a simple power law in momentum space, but several breaks would be expected. The most prominent feature in the injection spectrum is the CR-knee at several PeV, but it is not clear whether it is a break in the power-law slope or the beginning of an exponential cut-off. Regardless of the explanation of the knee, an extrapolation of the power-law injection to these highest energies without a modification in the injection slope leads to an over-prediction of CRs at these energies. As pointed out in [103] additional breaks in the source spectrum at ~ 5 GeV and $\sim 10^4$ GeV are expected. Incorporating those breaks into the source spectrum would allow a better fitting to the observed CR data. Changes in the source spectrum can be included in the post-processing of a CRPropa simulation and therefore it is possible to include this in the future without re-computing the full propagation. At the lowest energies, the choice of the fitting function for the diffusion coefficient leads to an additional offset to the observed data. Nevertheless, the demonstration of the impact of anisotropic transport and the gamma-ray signatures of the magnetic field structure can be shown with this CR model.
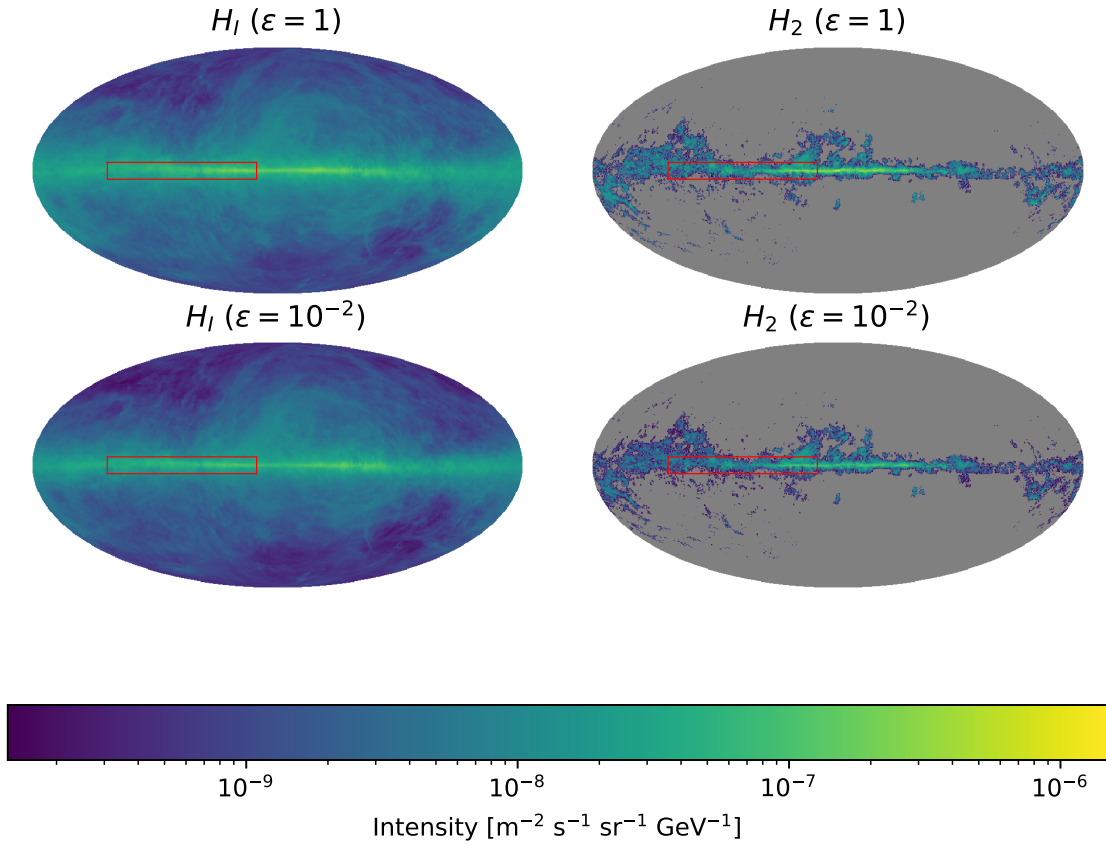
Figure 5.9. Intensity of the gamma-ray with $E_\gamma = 100\,\text{GeV}$. The top row shows the isotropic diffusion model ($\epsilon = 1$) and the lower row the anisotropic diffusion ($\epsilon = 10^{-2}$). The left column denotes the interaction with atomic hydrogen and the right column the interaction with molecular hydrogen. The red box denotes the sky region of the inner Galactic plane from the LHASSO analysis [42].

The gamma-ray maps derived from this CR distributions are shown in Figure 5.9 for the gamma-ray energy $E_\gamma = 100\,\text{GeV}$. These maps test the CR distribution at 1 TeV, assuming an average energy transfer of 10 % of the primary CR energy into the produced gamma-ray. As the local CR spectrum at 1 TeV is normalized to the observational data in both models, no differences due to the absolute normalization are expected. Therefore, all differences in the gamma-ray skymaps are originating from the differences in the underlying CR transport. Figure 5.10 shows the relative differences $(\Phi_{\epsilon=1} - \Phi_{\epsilon=10^{-2}})/\Phi_{\epsilon=1}$. A positive value (colored in red) corresponds to a higher gamma ray flux in the isotropic diffusion, while negative values (colored in blue) imply more gamma rays in the anisotropic region.

Strong differences in the interaction with the atomic hydrogen (H_I) can be seen. In the outer part of the Galactic plane the anisotropic diffusion leads to higher gamma-ray intensities. Here, the magnetic field lines are mainly oriented in the plane, and the reduction of the perpendicular diffusion leads to a stronger confinement of the CRs in the plane. The effect in the inner part of the Galactic plane is the opposite. Here, many field lines are pointing out of the plane and the parallel diffusion leads to a quicker escape of the CRs. Therefore the isotropic diffusion
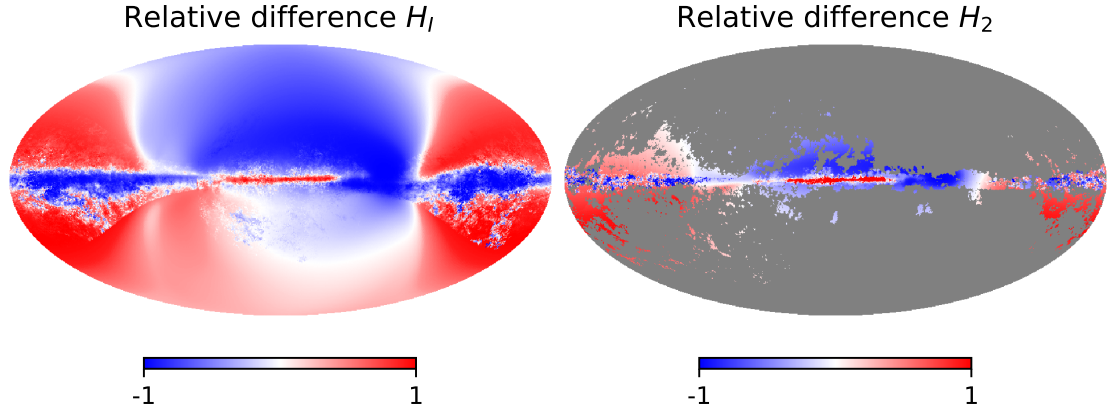
Figure 5.10. Relative differences in the skymaps from Figure 5.9. The differences are calculated as $(\Phi_{\epsilon=1} - \Phi_{\epsilon=0.01})/\Phi_{\epsilon=1}$.

offers the chance for CRs to propagate back into this region, which increases the gamma-ray flux for the isotropic diffusion. The same arguments can be applied to the galactic halo. The gamma ray production far away from the outer Galactic plane is higher in the isotropic diffusion. To produce gamma-rays there, it is needed that the CRs can reach it. This is more likely in the isotropic diffusion scenario, as there are no (or not many) field lines directly connected to the source regions. In the halo above or below the inner Galactic plane the gamma-ray production is higher in the anisotropic diffusion scenario. Here, the particles quickly follow the outward going field lines from the sources in the Galactic plane to the halo and subsequently produce the gamma rays more further from it. Also the difference between the northern and the southern region can be seen. This effect directly translates from the differences in the field line geometry (see Figure 5.2 for comparison). In the southern hemisphere, the field lines are more twisted. This implies the need of perpendicular diffusion of the CRs to reach the lowest latitudes and subsequently the gamma-ray production in the isotropic diffusion is enhanced.

The structure of the differences in the interaction with the molecular hydrogen is nearly the same, although large regions of the sky are not covered, due to the missing target material. The denser H_2 gas is expected to be stronger bound to the Galactic plane.

In addition to the physically explicable differences in the gamma-ray production, also some artifacts can be seen. The averaging of the emissivity in the rings and the multiplication with the ring column density leads to some sharp features in the differences. Especially in the H_I difference map the edge of the local ring, in which the Earth is placed, can be seen. This feature can be avoided if a three dimensional gas distribution would be used. But the transition from the observed column density to a realistic three dimensional distribution is not easy and needs several assumptions which can lead to other artifacts [89, 90]. At this point one has also to note, that the magnetic field structure and the distribution of the gas along a given LOS does not resolve the features in the local interstellar medium. The interpretation of differences from the anisotropic transport should therefore only be based on the large-scale differences.

5.5   Summary and Discussion

In this chapter, the diffuse gamma-ray emission from the Galactic plane has been calculated and its dependency on the structure of the Galactic magnetic Field (GMF) model and the anisotropy of the CR diffusion has been demonstrated.

In the first step, a realistic diffusion coefficient is estimated from a one-dimensional model including the CR streaming instability (see section 5.3.1). Here the diffusion along a flux tube is considered as well as the advection with the Alfvén speed pointing away from the Galactic disc and adiabatic energy changes due to the change of the advection direction at the Galactic plane. In this model, the excitation of Alfvén waves by the CRs, due to a gradient in the CR distribution function is included. The excited waves as well as the externally driven turbulence undergo wave-wave interactions leading to diffusion in the k-space, which modifies the CR diffusion. The model used here is quite simplistic compared to the more advanced models of [28, 109, 124], which include small-scale effects in the ISM like the variation in advection speed and changes in the ISM phase. Nevertheless, this simplistic model includes the main aspects of the non-linearity of the process and keeps a reasonable computation time which allows a fitting approach. This fast method is used to fitted to the observations by CALET [14] (see section 5.3.2) to the model and estimate the needed environment parameters. Along with the fitted CR spectrum the diffusion coefficient is calculated.

To incorporate the effect of the streaming instability into a fully three-dimensional transport model the diffusion coefficient is approximated by a smoothly broken power-law, which can be used in the CRPropa framework. The perpendicular diffusion $\kappa_\perp$, which is not considered in the one-dimensional model, is assumed to be a fraction ϵ of the parallel diffusion $\kappa_\parallel$. This parameter for the anisotropy of the diffusion tensor influences the transport and escape of the CRs depending on the structure of the GMF. Analyzing the escape time of CRs from the Galaxy shows the different influences from the applied model of the GMF (see section 5.3.3). In the strongly anisotropic cases ($\epsilon \leq 0.01$) at least two kinds of GMF models can be distinguished. This opens the possibility to use the secondary emission from the CRs like the diffuse gamma-ray emission to further constrain the GMF model.

In a first test of the anisotropic transport and its influence on the diffuse gamma-ray sky the solenoidal improved JF12 field [77] together with the inter-cloud component of the Central Molecular Zone field [62] is used. From a realistic three-dimensional transport model, the CR distribution within the Milky Way is computed (see section 5.4.2). From this, the all-sky gamma-ray emission is derived using a line-of-sight integration (see section 5.4.1). The overall structure of the resulting sky-maps (see Figure 5.9) is similar, which is mainly dominated by the distribution of the target gas. Nevertheless, some differences can be seen in the direct comparison (see Figure 5.10). Here, the sky can be divided into four regions (halo/plane and inner/outer Galaxy), where the anisotropic diffusion leads to different predictions of the gamma-ray emission. Those differences can be tested by all-sky gamma ray observations, which are done for example with the Large Area Telescope onboard the Fermi satellite or ground-based wide-field observatories like LHASSO.

Chapter 6

Cosmic Rays Close to the Sun

Galactic Cosmic Rays (GCRs) propagate from their sources in the Milky Way through the interstellar medium (ISM) before they enter the heliosphere. The particles at the higher energies ($\sim$ TeV) traverse it nearly undisturbed[1], while the lower energetic particles undergo significant modulation on their way in the heliosphere. As these relativistic particles travel through the interplanetary space, they can be used to infer information about the large-scale structure of the heliosphere [101].

The GCRs reaching the innermost part of the heliosphere travel through the Solar magnetic field and get deflected or absorbed. This effect leads to the *cosmic-ray Sun shadow* [1, 33]. When the GCRs reach the atmosphere of the Sun they can interact and create gamma-ray and neutrino emission (see [114] for early works).

In the following, the production of high-energy and very high-energy gamma rays in the solar atmosphere is investigated. First, the Solar Environment is discussed in section 6.1 covering the target density for the GCRs and magnetic field configuration. In section 6.2 the gamma-ray observations from the Sun and its seasonal variation are presented. In the following section 6.3 a simulation setup using CRPropa 3.2 is presented. The final results of the model are given in section 6.4 and critically discussed and summarized in section 6.5.

6.1 The Solar Environment

To investigate the production of gamma rays in the Solar atmosphere it is crucial to have a reliable description of the Solar environment. The presence of the magnetic field leads to deflections of the charged GCRs. Therefore the structure of the fields can influence the distribution of the gamma rays. In the case of the solar CR shadow, Becker Tjus et al. [33] have shown that different field geometries occurring either due to the temporal variation of the Sun or based on different assumptions on the continuation of the fieldlines from the solar surface into the heliosphere lead to differences in the shape and the depth of the shadow.

---

[1]The possible influence on cosmic-ray anisotropies in the TeV range by the heliosphere are presented by [47, 130].

6.1.1   Magnetic Field Models

The quantitative description of the three-dimensional strucutre and the evolution of the magnetic field in the chromosphere of the Sun and its extension into the interplanetary space is a longstanding question [59]. The first models focus on the multipole expansion of the field structure including the dipole and the quadrupole moment, which can be applied in the solar minimum. Later on, the azimuthal current sheet has been added to the model. Banaszkiewicz et al. [31] introduced the analytical dipole plus quadrupole plus current sheet (DQCS) model for the solar chromosphere and added a modified Parker spiral for the expansion into the interplanetary space. Here, the DQCS model is applied as a baseline reference to compare the impact of more structured models. This axisymmetric magnetic field is expressed in cylindrical polar coordinates (ρ, z in units of solar radii) as:

$$\frac{B_\rho}{M} = \frac{3\rho z}{r^5} + \frac{15Q}{8}\frac{\rho z}{r^7}\frac{(4z^2 - 3\rho^2)}{r^2} + \frac{K}{a_1}\frac{\rho}{\left[(|z| + a_1)^2 + \rho^2\right]^{3/2}} \tag{6.1}$$

$$\frac{B_z}{M} = \frac{2z^2 - \rho^2}{r^5} + \frac{3Q}{8}\frac{(8z^4 + 3\rho^4 - 24\rho^2 z^2)}{r^9} + \frac{K}{a_1}\frac{|z| + a_1}{\left[(|z| + a_1)^2 + \rho^2\right]^{3/2}} \quad , \tag{6.2}$$

where $r^2 = \rho^2 + z^2$ is the distance from the center of the Sun and the component of the magnetic field B_ρ, B_z are given in Gauss. The parameter Q controls the quadrupole contribution and is limited to the range $0 \leq Q \leq 1.5$ to ensure that the field lines surrounding the current sheet still connect to the Sun. Observations by the Ulysses spacecraft as well as ultraviolet images of the polar corona and chronograph observation fit best for $Q = 1.5$. For this case the authors to choose $K = 1.0$, $M = 1.789$ and $a_1 = 1.538$ to obtain $B_r \sim 3.1\,\text{nT}$ at 1 au distance [31]. In Figure 6.1 (upper left panel) an illustration of the field lines starting on the solar surface is presented.

While the DQCS model describes the quiescent Sun quite well, extending it to more active solar states is impossible. One way to incorporate this is the potential field source-surface (PFSS) model [22], which can be calculated for each Carrington Rotation based on a measured magnetogram. These maps spatially resolved the strength and polarity of the chromosphere magnetic field at the Sun's surface. The measurement is based on the Zeeman effect [129], which describes the splitting of emission lines from atoms in a magnetic field. The measurements are performed in ground-based facilities as well as on satellites. In this work, the measurements from the *Helioseismic and Magnetic Imager* (HMI) on board the *Solar and Heliospheric Observatory* are used.

The static PFSS model assumes no electric currents ($\vec{j} = \vec{0}$) in the solar corona. Therefore, the magnetic field is curl-free ($\nabla \times \vec{B} = \vec{0}$) and can be described by a gradient of scalar potential Φ as

$$\vec{B} = -\nabla\Phi \quad . \tag{6.3}$$

In addition to the measurements at the inner boundary of the model, a spherical *source surface* is assumed. At this outer boundary, all field lines are supposed to be purely radial. Typically the *source surface* is placed at a distance r_{ss} between 2 and
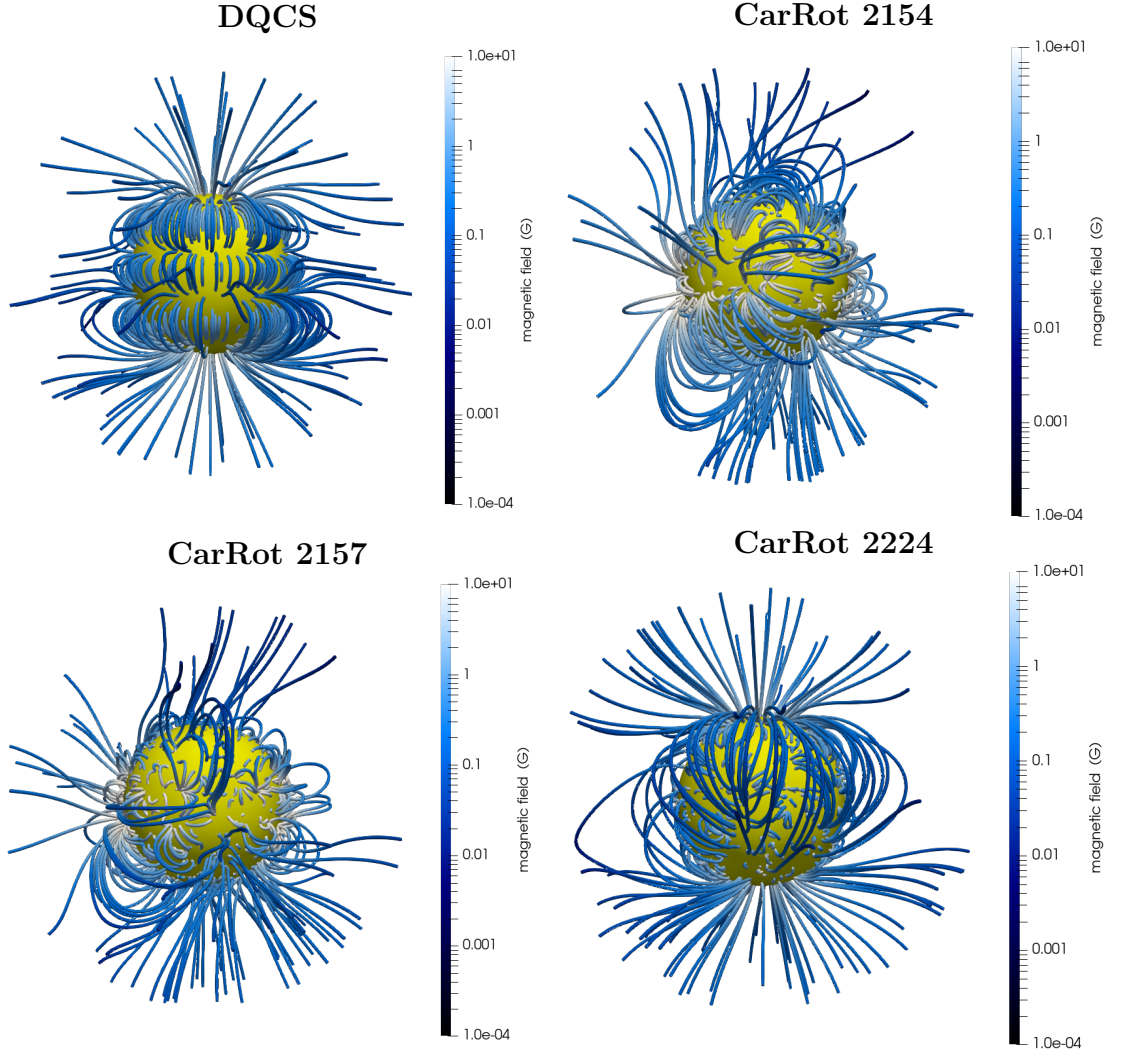
Figure 6.1. Field lines starting on the surface of the Sun for different magnetic field models. The upper left panel corresponds to the DQCS model from [31]. The other panels represent the PFSS model for different Carrington Rotations (CarRot).

3 solar radii. In the context of this work, the value is fixed at $r_{ss} = 2.5R_\odot$ as in [1, 25] and the investigation of the impact of this choice is left for future work.

The calculation of the PFSS model is done by the publicly available *pfss* Python package from Anony Yeates[2] on a spherical grid containing 60 bins in $\log(r)$, 180 bins in $\cos\theta$ and 360 bins in ϕ. Between the grid points, the magnetic field is interpolated linearly. The input, a synoptic magnetogram for a full Carrington Rotation (CarRot), can be downloaded from the HMI data center with this Python package. In the following three different times, Carrington Rotation 2154, 2157, and 2224 are explored. Figure 6.1 shows the magnetic field lines in these models. The first two times describe an active phase of the Sun, and therefore many field lines show loops close to the solar surface. The last time is near the solar minimum and the field lines are more ordered and partly compatible with the DQCS model.

---

[2]https://github.com/antyeats1983/pfss
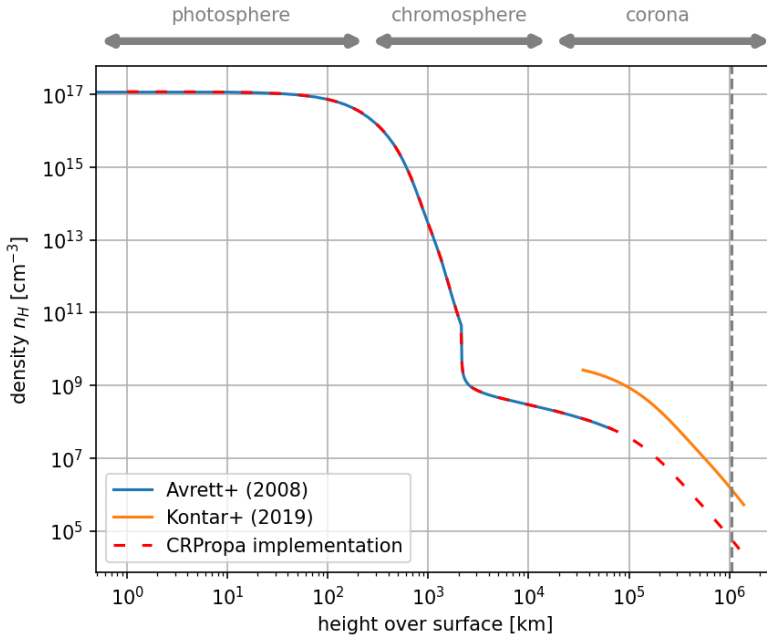
Figure 6.2. Radial density profile in the Chromosphere and Corona. The vertical dashed line indicates the source surface $r_{ss} = 2.5 r_\odot$ from the PFSS model, which is the outer boundary of our region of interest.

6.1.2   Gas Distribution

Besides the magnetic field configuration, which determines the transport properties of the GCRs, the target distribution is a key ingredient to understanding the high-energy emission from GCRs in the solar atmosphere. As the high-energy gamma rays are believed to originate from hadronic interaction [18], the needed target distribution is the plasma density.

The main focus of this work lies on the influence of the magnetic field configurations and the changes in gamma-ray signatures introduced by it. Therefore, the target distribution is kept simple. In the *Chromosphere* the spherically symmetric model from Avrett & Loeser [30] is applied. This region close to the solar surface has the highest atmospheric densities and is therefore expected to contribute significantly to the total gamma ray flux. For the *Corona* above, the radial shape of the density model by Kontar et al. [80] is used. As their coronal model is developed for Type III radio bursts it describes the rather high state of the plasma density. To match the outer part of the chromosphere model the normalization of the coronal model is reduced. Both models and the finally implemented version are shown in Figure 6.2.

6.2   Gamma Ray Observations of the Sun

The idea of hadronic interactions of GCRs with the atmosphere of the Sun was established in the 1990s (see [114] for some first work). In the high-energy range, gamma rays produced by the Sun have been associated with transient events like

solar flares [10]. Those flare-induced gamma rays have been observed with a maximum energy ~ 4 GeV, which is at the lower boundary of the energies discussed here [10].

The steady gamma-ray flux from the Sun covers energies from the GeV to the multi-TeV regime. The first detection has been done with EGRET data [95] and can be divided into two components. The dominant contribution called *disk-component* comes from GCRs following magnetic flux tubes into the solar atmosphere and undergoing inelastic interactions with the ambient plasma. The second subdominant contribution so-called *halo-component* results from cosmic ray electron interactions with the solar photon field via Inverse Compton Scattering (ICS).

Later on, the existence of the two components have been confirmed by the Fermi-LAT collaboration [7]. The data from the Fermi-LAT have been used to investigate the disk component in different time intervals to show the dependency on the solar cycle. The first analysis in 2018 showed a dip at $\sim 30-50$ GeV which differs in strength before and after 2010 [86]. A second analysis in 2018 showed that the dip is strongest during solar minimum [122], and in the average over the full solar cycle the strength of the dip is reduced [85]. Up to now, there is no clear explanation for this dip.

Not only does this feature show a clear time-dependence. In the energy range $1-10$ GeV the variation is anti-correlated with the solar activity and varies with a factor of two to three. This cannot be explained by the modulation of GCRs, which is about $\sim 15\%$ for 10 GeV protons.

At the highest energies (~ 1 TeV) HAWC also reported a detection of gamma rays from the solar disk [18]. Also in this energy range, a variation with solar activity is observed. The energy dependence of the gamma ray fluxes steepens from $\propto E^{-2.2}$ in the high-energy regime ($E \leq 200$ GeV, see [85]) to $E^{-3.6}$ in the ultra-high-energy range ($E \geq 500$ GeV, see [18]). A collection of the available measurements of the solar disk component is compiled in Figure 6.3.

6.3 Simulation Setup

The simulations of the gamma-ray emission from the solar atmosphere are performed with CRPropa 3.2 [23] (see Chapter 3.1 for a detailed discussion). In this application, the equation of motion is solved using the Boris-push method. The background field is either the analytical DQCS model or the PFSS model for the different Carrington rotations described above. The solver has an adaptive step size between $100\,\text{km} \leq \Delta s \leq 0.1 R_{\odot}$ and a tolerance of $P = 10^{-4}$.

To model the gamma-ray emission the *Hadronic Interaction Plugin* (see section 3.2) is added. Here, the cross-section from Orusa et al. [97] is used, as they have the lowest energy threshold, which allows us to interpret the gamma-ray data in the GeV range.

The injection of GCRs is placed at the *source surface* of the PFSS model, a sphere with radius $r = 2.5\,R_{\odot}$. The particles are distributed homogeneously on the surface and have an isotropic and ingoing pitch-angle distribution. A pure proton flux is assumed. This is a reasonable assumption at GeV-TeV energies, as the cosmic-ray spectrum is dominated by protons at these low energies [34] and the
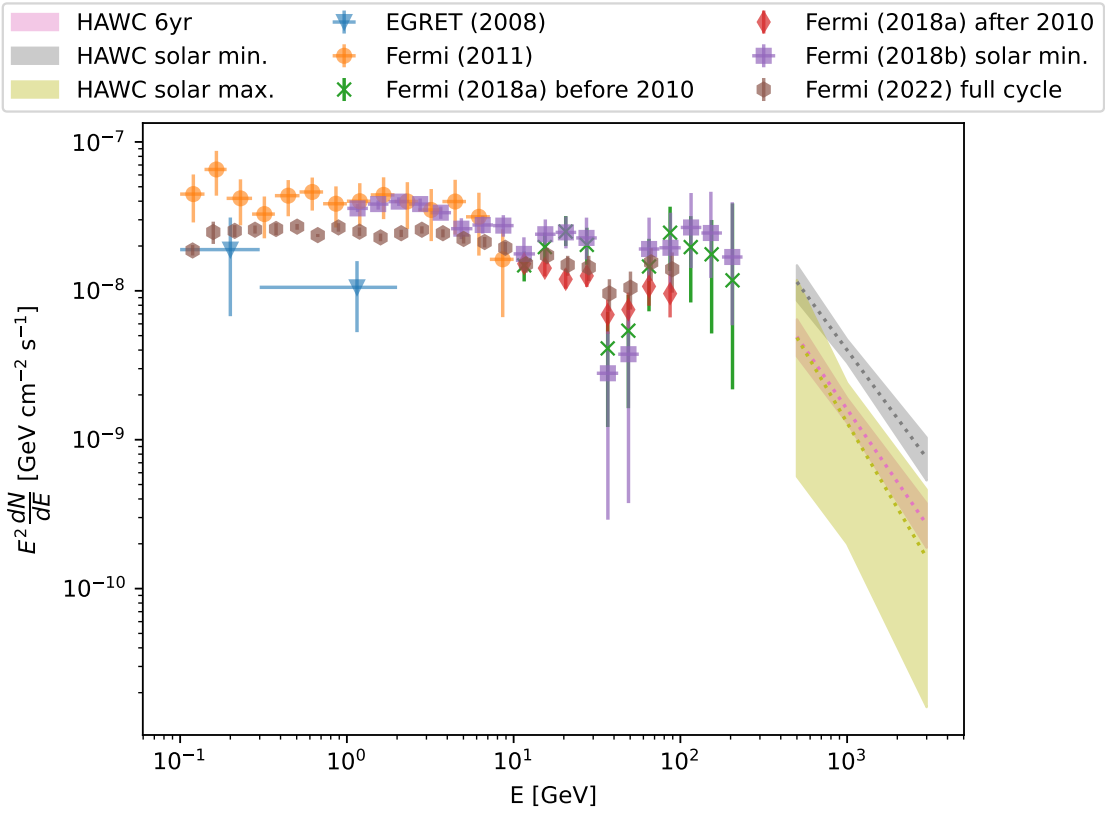
Figure 6.3. Collection of gamma-ray measurements from the solar disk with different instruments: HAWC (2023) [18], EGRET (2008) [95], Fermi-LAT (2011) [7], (2018a) [86], (2018b) [122], (2022) [85].

effect from interactions of heavier nuclei is expected to be of second order. The initial energy of the particles can either be a mono-energetic injection or a power-law distribution. The latter one is done with $\mathrm{d}N/\mathrm{d}E \propto E^{-1}$, which allows equal statistics in each logarithmic energy bin. For a realistic consideration, the energy distribution is reweighted to the local interstellar spectrum (LIS), as it is observed on Earth for sufficient high energies. The reweighting is performed by assigning a weight

$$w_i = \frac{J_{\mathrm{LIS}}(E_0)}{N_{\mathrm{sim}} \log\left(\frac{E_{\mathrm{max}}}{E_{\mathrm{min}}}\right) E_0^{-1}} \tag{6.4}$$

to each candidate. Here, J_{LIS} denotes the local interstellar spectrum, E_0 the initial energy of the particle, N_{sim} the total number of simulated particles, and E_{min} and E_{max} the minimal and maximal simulated energy respectively. To parametrize the local interstellar spectrum we follow the approach by [106], where the LIS reads as

$$J_{\mathrm{LIS}}(E) = 2.7\, E^{1.12} \beta^{-2} \left(\frac{E + 0.67}{1.67}\right)^{-3.92} \frac{\mathrm{particles}}{\mathrm{m^2\, sr\, s\, MeV}} \quad . \tag{6.5}$$

Here, E denotes the proton energy in GeV and $\beta = v/c$ is the speed in units of the speed of light. In Figure 6.4 the parametrization is compared with recent measurements of the GCR proton flux at Earth.
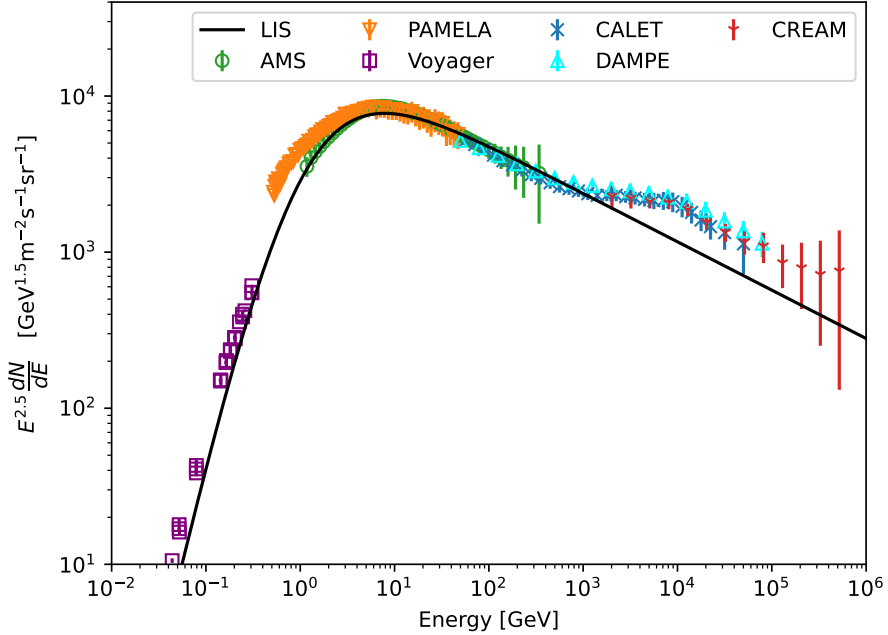
Figure 6.4. Parametrization of the local interstellar spectrum (eq. 6.5) with the measurements from AMS-02 [16], CALET [14], CREAM [44], Pamela [15], Voyager [45, 119, 120] and Dampe [26]. The data from AMS-02 and Pamela have been corrected for the solar modulation following the force field approximation and the modulation potential as given in the corresponding reference.

The simulation volume is restricted by two spheres, both centered in the Sun. The inner boundary is placed at $r = 0.9R_\odot$. This boundary should in principle never be reached by GCRs as they would interact in the solar atmosphere before. The outer boundary at $r = 2.51R_\odot$ is slightly further out than the starting position. All particles that are mirrored in the magnetic field will follow the fieldlines and have no chance to travel back. Therefore, all particles reaching one of the boundaries are removed from the simulation. Additionally, all GCRs with an energy below 1 GeV are removed too.

All gamma rays created in the simulation are stored independently of whether they can be observed from Earth. This differentiation is done in the post-processing. Here, three different, direction-based, selections are discussed:

(1) All produced gamma-rays are collected. This filter is used to show the total production of gamma rays. It can also be applied in those scenarios where spatial dependence is investigated and high statistics are required. The total statistic is typically reduced by more than a factor ~ 10 for other selections.

(2) This selection collects all gamma rays with an outgoing momentum ($p_r > 0$). The radial component of the (unit) momentum can be calculated by $p_r = \vec{p} \cdot \vec{r}/|\vec{r}|$.

(3) In this selection, all outgoing gamma rays and those ingoing ones that do not reach the Sun's surface are collected. Considering a gamma ray produced at position $\vec{r}$ and in direction $\vec{p}$, the closest point to the center of the Sun is reached
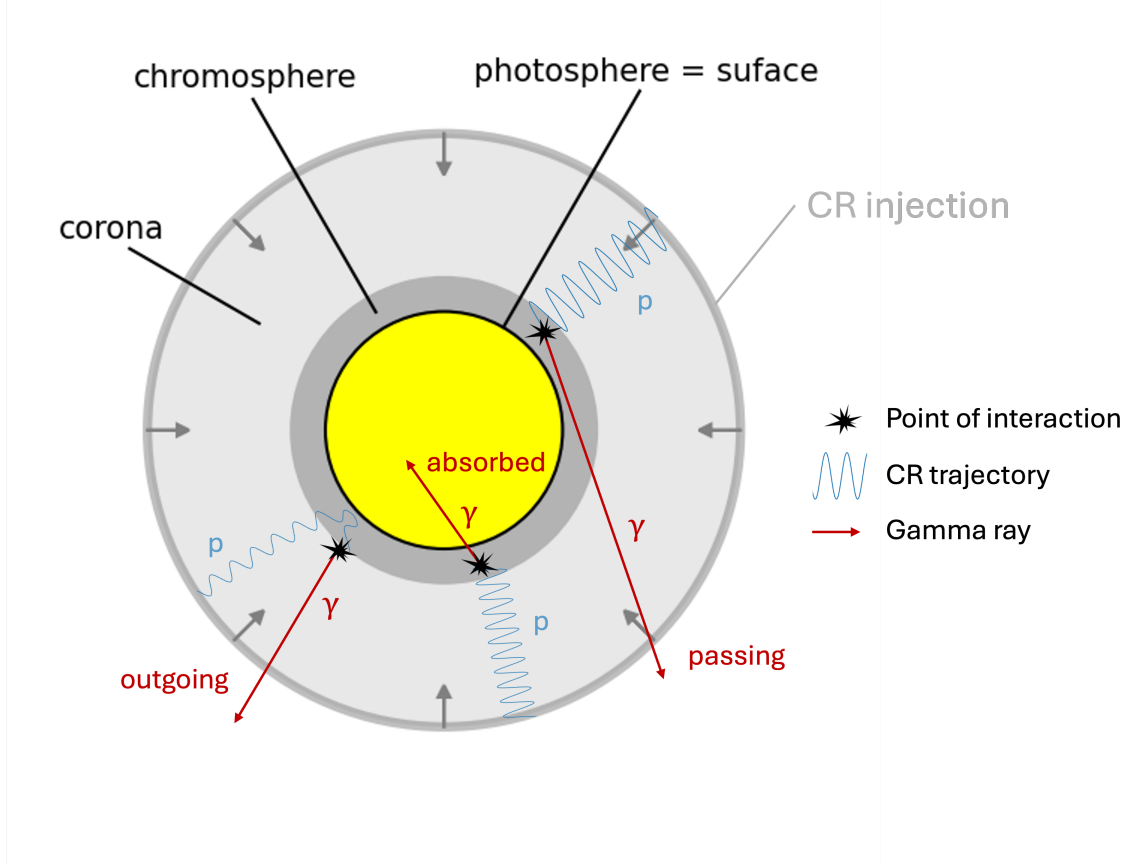
Figure 6.5. Schematic illustration of the simulation setup and the layers of the Solar atmosphere. Three kinds of produced gamma-rays can be distinguished, depending on their emission direction.

at $\vec{x} = \vec{r} + t\,\vec{p}$ with $t = -\vec{r} \cdot \vec{p}/|\vec{p}|^2$. Allowing only propagation in the forward direction requires $t \geq 0$. In this filter, all particles with a minimal distance

$$d^2_{\text{min}} = (x + t\,p_x)^2 + (y + t\,p_y)^2 + (z + t\,p_z)^2 \geq R_\odot \qquad (6.6)$$

or outgoing direction $(t < 0)$ are collected.

A schematic illustration of the simulation setup and the different directions for the gamma-ray production is given in Figure 6.5.

6.4   Model Results

The results from the simulation are presented in two steps. First, the analysis from the monoenergetic injection is summarized in section 6.4.1. This allows easier discrimination of the effects at low (1 GeV), medium (100 GeV), and high (10 TeV) energies. Afterward, the expected gamma-ray flux for a realistic injection of GCRs following the local interstellar spectrum is presented in section 6.4.2

6.4.1 Mono-energetic injection

The first test for the mono-energetic simulations is the production height over the surface. Figure 6.6 shows the differential number

$$\frac{\mathrm{d}N_\gamma}{\mathrm{d}R} \approx \frac{N_\gamma}{\Delta R} \tag{6.7}$$

from the binned radial position of the created gamma rays. Here, N_γ denotes the number of observed particles in the bin $[R; R + \Delta R]$.

In all cases (energy of the primary, magnetic field configuration, type of direction filtering), a sharp increase at $H \approx 10^3\,\mathrm{km}$ towards the solar surface is observed. This effect is caused by the increase of the target density in the chromosphere at this distance (compare Figure 6.2). In the innermost part of the chromosphere, the total production rate (see blue points) saturates, as the density becomes constant there.

The main difference between the distribution of all produced gamma rays and those that can be observed (outward going - orange cross; passing the surface - green square) is the absolute normalization. Differences in the shape are visible for the highest energy $E = 10\,\mathrm{TeV}$ in the DQCS model and for the Carrington rotation 2224. The gamma-ray production is enhanced in the range between 10^2 and 10^3 km above the solar surface. The pileup is stronger in the case of the DQCS field where the enhancement reaches a factor ~ 20, while the PFSS field leads to an increase of a factor ~ 5. Compared to the magnetic field in the other Carrington rotations, the cases of enhancement show a much more regular structure. Due to the gradient in the magnetic field strength, the expected point of the mirroring depends much more on the starting position in the more active solar phase. This averages out the pileup in the Carrington rotations 2154 and 2157.

The effect of the mirroring can also be seen in the distribution of the initial pitch-angle from the GCRs producing the gamma rays as shown in Figure 6.7. The initial pitch-angle distribution is flat in the range $-1 \leq \mu_0 \leq 0$, but only GCRs with a pitch-angle small enough to be in the magnetic mirror's loss cone can produce gamma rays.

Finally, to illustrate the influence of the magnetic field structure the position of the created gamma rays on the solar surface (or projected onto it) is shown in Figure 6.8. The spatial position in longitude ϕ and latitude θ is calculated as

$$\phi = \arctan\left(\frac{Y}{X}\right) \quad ; \quad \theta = \arcsin\left(\frac{Z}{\sqrt{X^2 + Y^2 + Z^2}}\right) \tag{6.8}$$

and binned with the Hierarchical Equal Area isoLatitude Pixelization (HEALPix) scheme [61].

While Figure 6.8 shows the spatial distribution of all produced gamma rays, in Figure 6.9 the filtering for the outgoing particles has been applied. As this filter reduces the total statistics dramatically, a lower resolution with nSide = 64 is shown. In general, both maps show the same structures but may differ in the size and the absolute normalization of these substructures. The following discussion only focuses on the total produced gamma rays as they have a higher statistic and a better resolution.
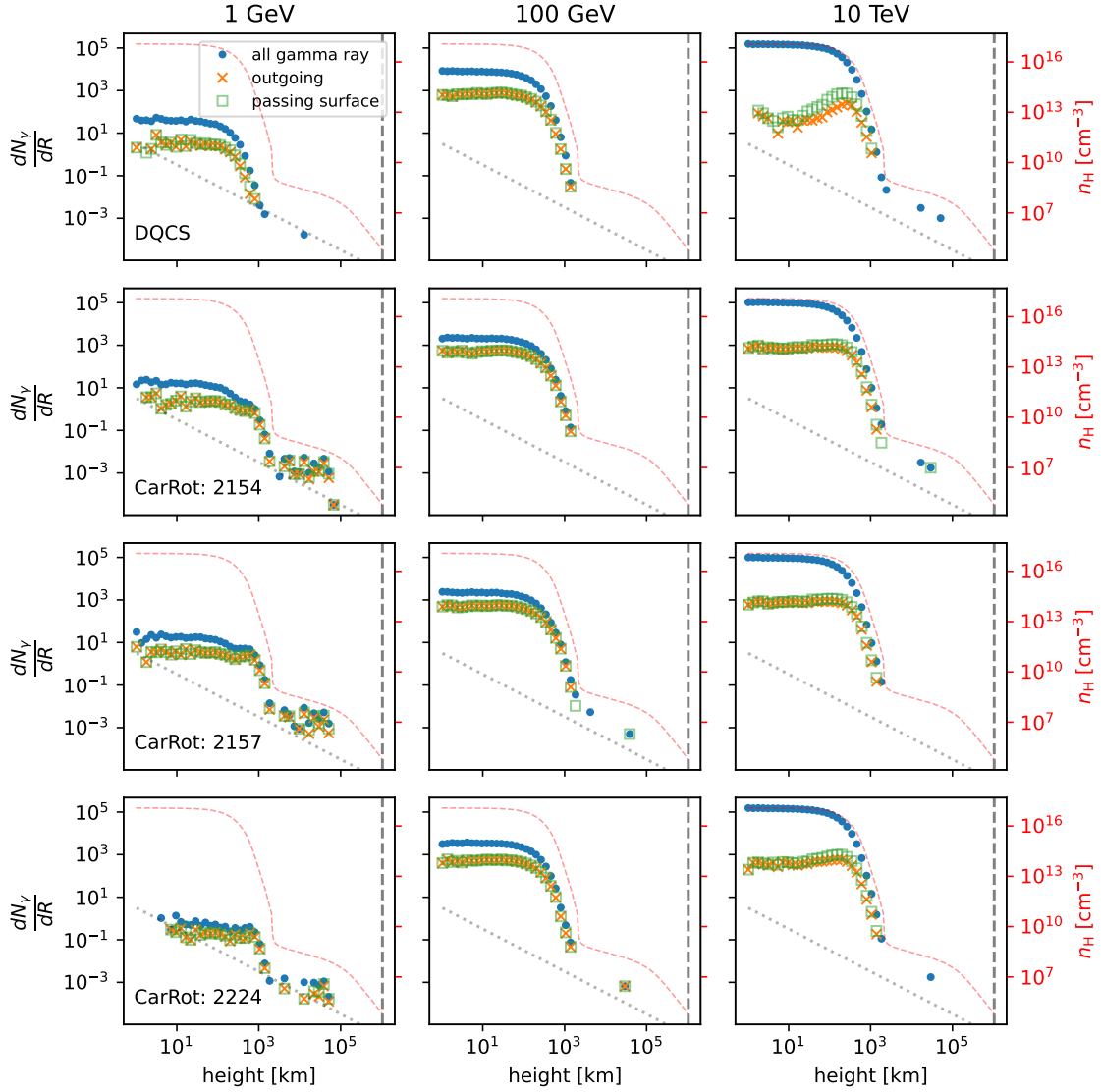
Figure 6.6. Height distribution of the produced gamma-rays in different magnetic field configurations (rows) at different primary energies (columns). The blue points show all produced gamma rays while the orange points are only those gamma rays with an outward momentum direction. The green squares show all gamma rays that do not hit the solar surface. The grey dotted line shows the minimal resolvable statistics, and the vertical dashed line shows the primary GCRs' injection distance. The red dashed line indicates the target density profile as shown in Figure 6.2.
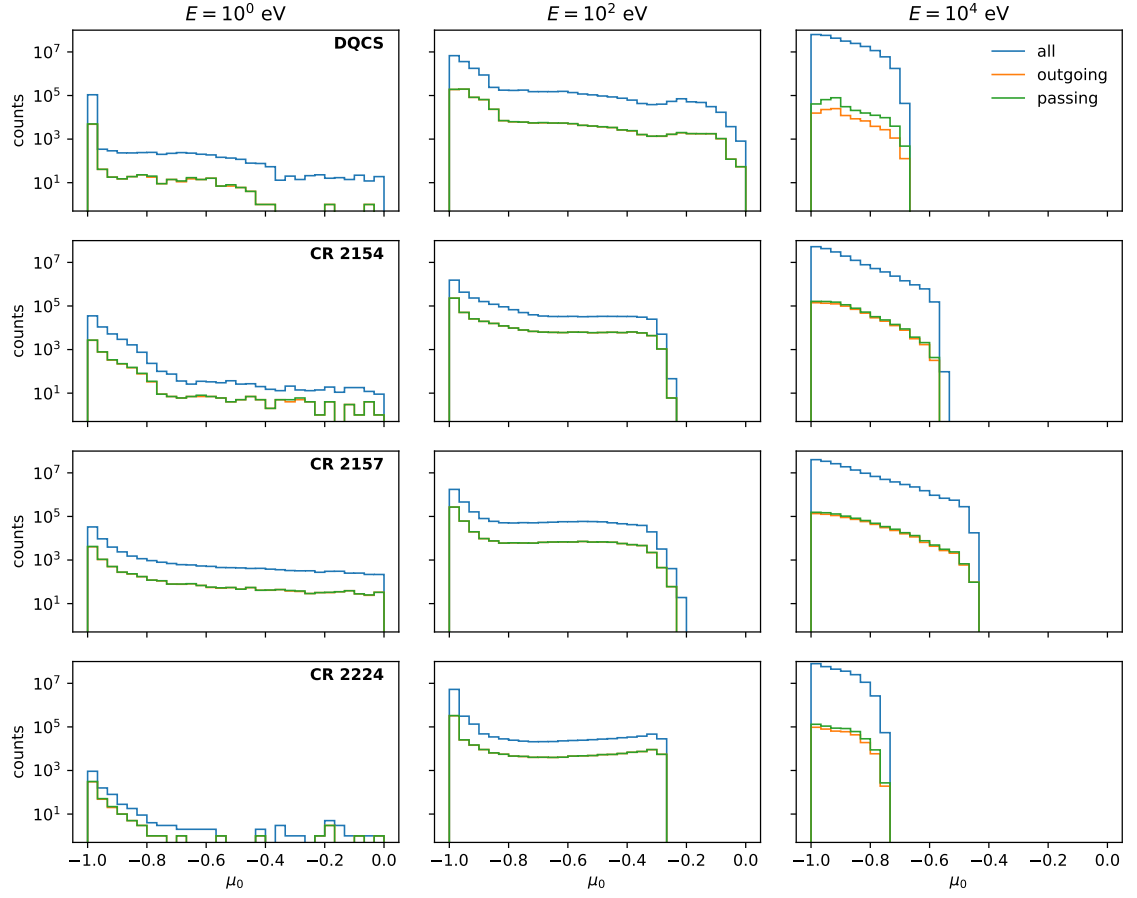
Figure 6.7. Distribution of the initial pitch-angle leading to gamma-ray production. The column denotes the initial energy of the particle and the row denotes the magnetic field configuration.

The DQCS magnetic field model does not show any dependence on the longitudinal position as the magnetic field is symmetric in rotation around the z-axis. In the low and middle energies, the production of gamma rays is not possible everywhere on the solar surface. Only cosmic rays from the polar caps and on the current sheet can reach close enough to the solar surface to undergo interactions. The current sheet leads to a difference in the number of gamma rays between the northern and southern hemispheres. In the highest energy, the full solar disk is filled with gamma-ray production but a latitude dependence from the quadrupole moment of the field structure is visible.

In all PFSS models more substructures can be observed as the field geometry allows for more complexity. In the Carrington Rotation 2224, the low-energetic GCRs can hardly reach the solar atmosphere and are mirrored away before interaction. Therefore, only some random production places show up. GCRs with intermediate energy show more structured gamma-ray emission. The polar caps are dominant and comparable in size with the DQCS magnetic field configuration. Between these caps, some filamentary structures can be observed. The highest energies fill the total solar disk and do not allow to infer any information about the substructures in the magnetic field.

All produced gamma rays
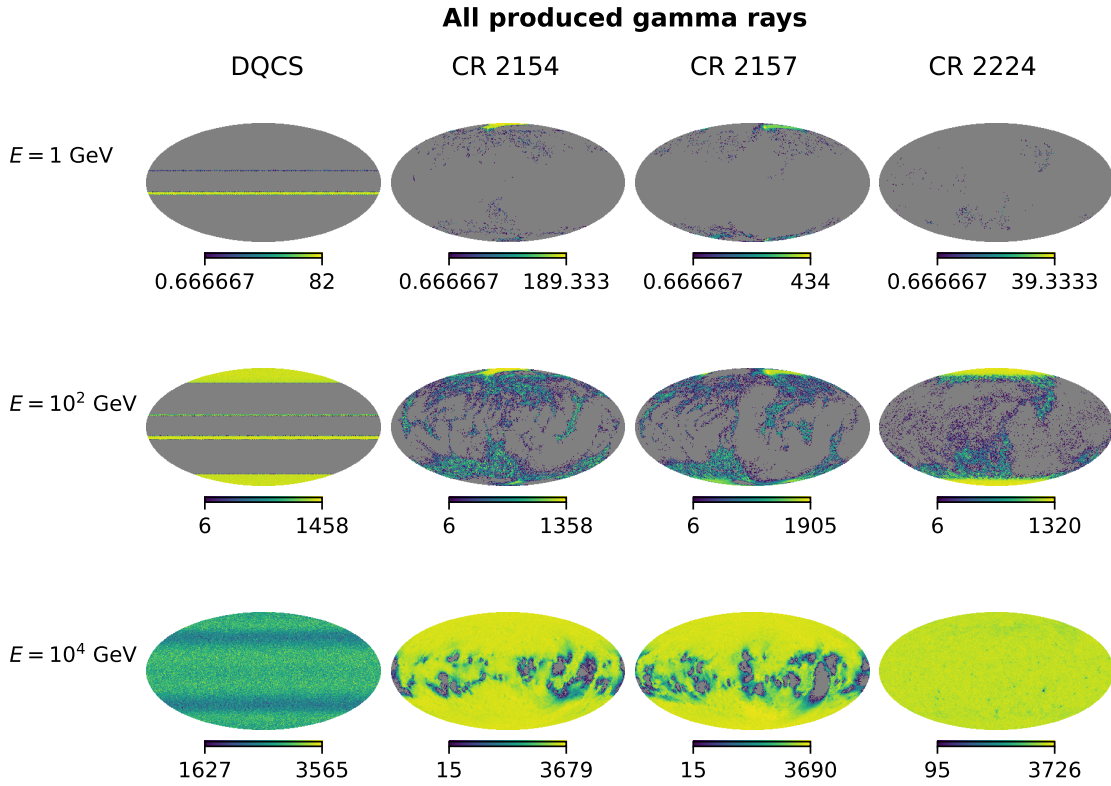
Figure 6.8. Locations of production for the solar gamma rays projected onto the solar surface using a Mollweide projection. All maps show the count histogram of produced gamma rays independently of their energy. Note that the lowest energies ($E = 1\,\mathrm{GeV}$) have been corrected for the larger total statistics in the simulation, and therefore count numbers below 1 are possible. All maps have a HEALPix binning with nSide $= 128$.

The PFSS models around the solar maximum (Carrington rotations 2154 and 2157) show similar behavior in all energy bands, but the local positions of filaments and voids are shifted against each other. In the lowest energies, a coronal hole at the northern pole is observed. This hole is the main source of gamma-ray emission at these energies. In the southern polar region, some small hotspots lead to the production of gamma rays but they are limited in size and total number. Nevertheless, the maximum number of gamma rays per solid angle bin is higher compared to the more ordered configuration from the Carrington rotation 2224 or the DQCS model. In the intermediate energy, the same coronal holes are hotspots of gamma-ray production. Additionally, more filaments covering the region around the solar equator can be observed. For the highest energetic GCRs, the coronal hole does not lead to any significant enhancement of gamma-ray production as nearly the full solar disk is filled. Only some voids, can be observed around the equator. These voids are probably caused by active regions on the solar surface, which have a strong magnetic field and cause a strong mirroring and a deflection of GCRs. This illustrates the capability of high-energy and very high-energy gamma-ray observations to give insights into the activity of the Sun.

outgoing gamma rays
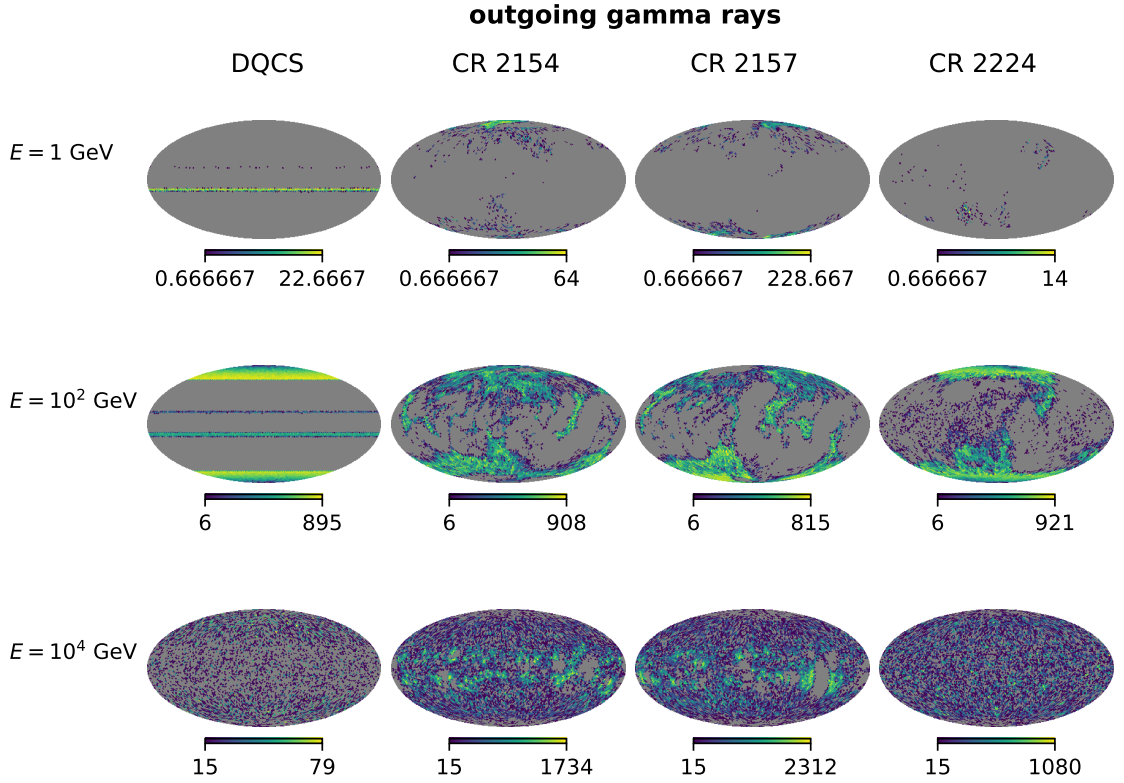
Figure 6.9. Same as Figure 6.8, but only outgoing gamma rays are shown with a lower resolution of nSide = 64.

6.4.2 Realistic injection spectrum

The final exercise is the reproduction of the total gamma-ray spectrum emitted from the Sun. To do this calculation, one has to assume a GCR flux reaching the outer boundary of our simulation at $r = 2.5R_\odot$. As a starting point, we assume the local interstellar spectrum to arrive at this point without any modulation. Although this is a reasonable assumption for the $\sim$ TeV particle energies, the lowest energies would be affected more, and the results from this model can be understood as an upper limit on the expected emission.

In Figure 6.10 the resulting SED for the solar gamma rays in the different magnetic field models is shown. The dotted lines indicate the total flux from all produced gamma rays, without any further filtering. The predictions with the PFSS models show an energy dependence $\sim E^{-2.2}$ for a wide energy range. Only a weak steepening $\Delta\alpha \approx 0.1$ in the TeV range can be observed. This is in contradiction to the observation by HAWC. The total gamma-ray flux without any filtering shows a sessional variation of a factor ~ 2, which is in agreement to the gamma ray measurements. The enhancement in the solar minimum phase vanishes at several TeV. The gamma-ray flux in the DQCS model is significantly steeper than the PFSS results and follows the expectation from the local interstellar spectrum.

A real observation of the gamma rays would require them, to have an outward direction. The solid lines in Figure 6.10 show only those gamma rays. In the PFSS models, the total flux is reduced by a factor ~ 10 in the multiple GeV range
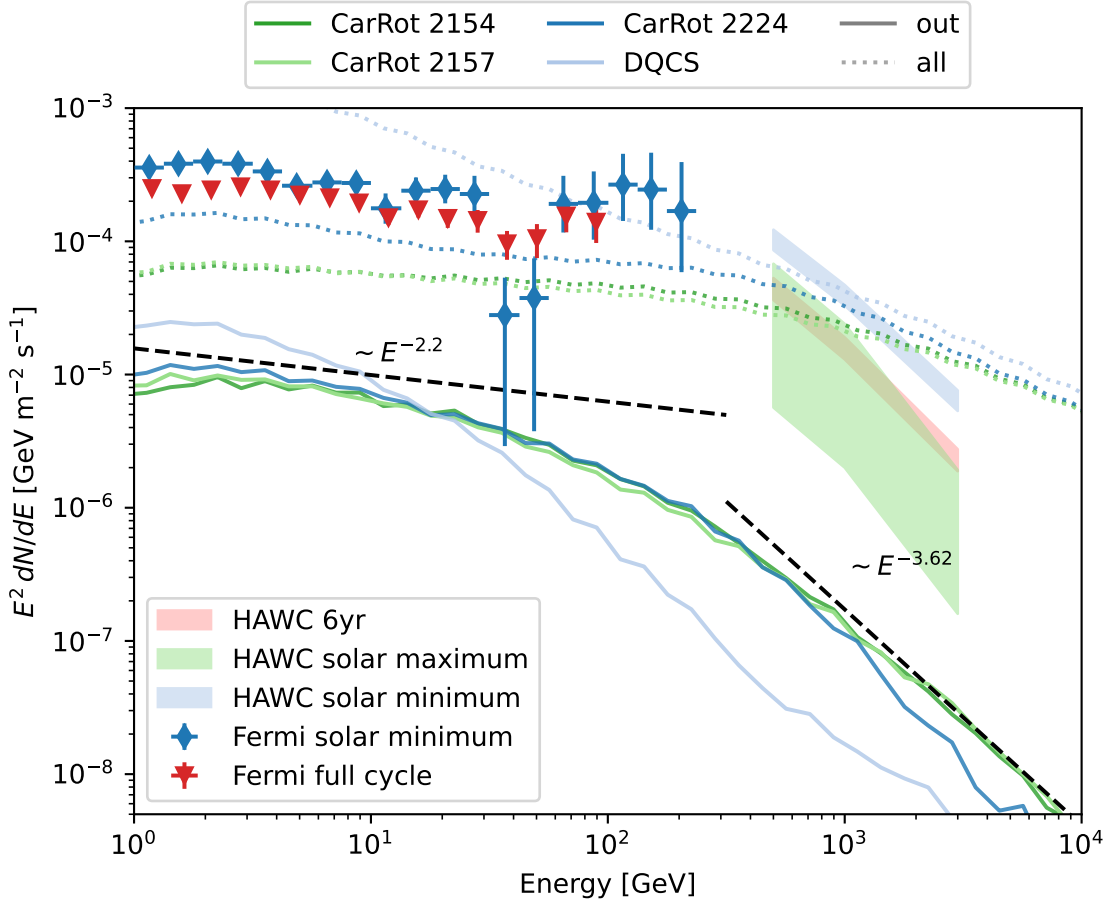
Figure 6.10. Spectrum of the solar gamma-ray emission in different magnetic field configurations. The results are shown for all produced gamma rays (dotted lines) and the outgoing gamma rays (solid lines). The different colors show different magnetic field configurations. The given data points are from the Fermi LAT for the solar minimum [122] and the full solar cycle [85]. Also the errorbands from the HAWC measurements [18] are shown. The dashed black lines indicate different power-law slopes to guide the eye.

compared to the total amount of produced gamma rays. The energy scaling has a break at ~ 200 GeV and steepens toward the higher energy. The spectral slope at the highest energies is comparable to the measurement by HAWC [18]. In the lower energies, the energy scaling does not fully match the observation from the Fermi-LAT. Here one has to note that the energy dependence of the solar modulation has not been taken into account, which could accomplish this. Nevertheless, the total normalization of expected gamma-ray emission is a factor ~ 20 too low in this prediction. Additionally, the variation of the gamma-ray flux with the solar cycle can not be reproduced with the outgoing gamma-rays. Here, higher statistics simulation might help to identify the difference between these Carrington rotations.

In the DQCS magnetic field model, the difference between the expected flux and the measurements is even higher. In the very high-energy part, the energy scaling is roughly in agreement with the data, but the observable flux is lower by more than

two orders of magnitude. In the high-energy regime, the energy scaling follows more the local interstellar spectrum ($\sim E^{-2.7}$) than the observed $\sim E^{-2.2}$. Overall one can follow that the DQCS magnetic field configuration is not sufficient to describe the energy-dependent mirroring correctly.

Besides the solar modulation at low energies, another effect on the normalization comes from the initial pitch-angle distribution. The propagation of GCRs in the interplanetary magnetic field might affect the pitch-angle distribution. The arrival direction detected on Earth shows a nearly isotropic distribution, but the magnetic field strength increases towards the Sun and might cause a magnetic mirroring on its own. This has been investigated by Hutchinson et al. [68], who have used a simplistic isotropic scattering of GCRs to describe scattering into the loss cone of the magnetic mirror. In the future, measurements of the GCR distribution function from Parker Solar Probe and Solar Orbiter, which probe regions closer to the Sun, will help to constrain the input for this kind of simulation.

6.5   Summary and Discussion

In this chapter, the intricate dynamics of GCRs as they interact with the solar atmosphere have been explored. This study provides a comprehensive analysis of the production of high-energy and very high-energy gamma rays resulting from these interactions. It illustrates how the magnetic field structure influences the gamma-ray production and demonstrates that the CRPropa framework is a suitable tool to study this emission.

The mono-energetic simulations performed here, allow a discrimination of the energy-dependent effects in the low, medium, and high energy regimes. The radial gamma-ray density follows in all energies the gas distribution but only in the highest energies and for the more regular magnetic field configuration (DQCS and Carrington rotation 2224) a pile-up of gamma rays at the sharp density increase in the chromosphere can be observed. Also, the importance of the initial pitch-angle is demonstrated in the mono-energetic simulations. The highest energies show a clear effect of the magnetic mirroring, where only particles with a small pitch-angle can reach the lower layers of the solar atmosphere. This effect becomes smaller in the intermediate energies and is nearly not visible at the lowest energies.

In the simulation covering the full energy range of GCRs, the expected gamma-ray flux has been calculated. For the gamma rays, which leave the solar atmosphere again (outgoing direction), the energy scaling in the VHE regime matches the observation quite well. In the HE regime, only the PFSS magnetic field models can produce a reasonable energy scaling, although additional effects from the solar modulation are expected. In the current models, a reproduction of the total gamma-ray flux is not possible. The flux is roughly a factor ~ 20 too low.

With this work, it has been demonstrated, that the gamma-ray observation of the Sun can be a useful tool to understand the magnetic field configuration in the solar atmosphere and the transport properties of the GCRs. For future work several open points have to be addressed:

- The magnetic field model used here is the PFSS model. This relies on the

input magnetogram and the assumption of the *source surface*. In the future, more systematic tests about the location of this distance would be needed. In principle, it is not necessary to assume that this surface is a sphere or constant in time. Here only one source of the magnetogram has been tested and the results should be compared to different measurements from other observatories. Also, the effect of the interpolation between the spherical grid has to be studied further. Schlegel et al. [112] showed that the interpolation can change the simulated transport properties of cosmic rays. A first step to further improve the simulation can be increasing the grid size, to minimize the interpolation.

- Additionally to the PFSS model other magnetic field models for the Sun can be used. The CRPropa code allows an easy customization of the magnetic field. All models based on a three-dimensional grid can be used directly. Other analytical models can be added to the code.

- The magnetic field had only a regular component. All turbulent parts of the fields are neglected. In the future, the implementation of a turbulent field on top of the background field can be tested. Alternatively an effective description of the GCR transport by assuming a random scattering or the change to a transport equation-based description might be used.

- The input for the initial energy distribution of the GCRs is the isotropic local interstellar spectrum. The effect of modulation close to the Sun has not been evaluated yet. For future work, the changes in the energy spectrum and the pitch-angle distribution can be incorporated in this simulation. When a description of the SED and the pitch-angle distribution is provided by other works the simulation output produced here, can be reweighted to match these initial conditions. This procedure avoids long re-computation of the simulation. In principle, CRPropa can also be used to model the solar modulation directly. In this case, the GCR measurements at the Earth can be used as an input for the simulation.

- The main focus of this work lies on the magnetic field configuration. Therefore, a quite simplistic target density distribution has been chosen. In the future, a more consistent description of the plasma density and the magnetic field structure is needed. It is known that the outbursts of the Sun change the local structure of the target density significantly [70]. One option for a consistent description is the use of MHD results, which model the magnetic field structure and the plasma density at the same time.

- In the literature also the layers below the photosphere have been discussed to have a significant contribution to the VHE gamma rays. Li et al. [84] attempted to identify the magnetic field structures at the solar surface by considering vertical flux tubes. These so-called network elements and vertical flux sheets can be added to the three-dimensional description presented here. This would allow to propagate the GCRs further into the photosphere.

- The hadronic interactions of the GCRs in the solar atmosphere do not only produce gamma rays. Also, secondary neutrinos as well as electrons and positrons are created. In the lowest energies ($\sim$ MeV), the neutrino flux is dominated by the neutrino emission from the fusion processes occurring in the center of the Sun. However, at the higher energies, a contribution from the hadronic interactions might be possible. The electrons and positrons produced in the inelastic interactions can propagate further in the solar magnetic field and create synchrotron radiation and secondary gamma rays via the inverse Compton scattering on the solar photon field. These ICS gamma rays might add to the observed halo component of the solar gamma-ray flux.

Overall, it has been shown that CRPropa is a powerful tool for modeling gamma-ray emission from the Sun. Those gamma rays can help to identify the relevant magnetic field structure. However, a more detailed and consistent description of the field, the target density, and the initial GCR flux is needed.

Chapter 7

Conclusion and Discussion

In this thesis the gamma ray emission from cosmic rays (CRs) undergoing inelastic interactions have been analyzed for different astrophysical applications. The first step for these investigations is an efficient modeling of those interactions. Afterwards the emission from three different astrophysical environments (chapter 4: Galactic Center; chapter 5: Milky Way; chapter 6: Solar atmosphere) has been analyzed to contribute answering the four science questions. In the following the results are summarized and discussed:

How can the interactions of CR protons with the ambient gas be modeled in an efficient way?

CR transport is often modeled with the publicly available framework CRPropa [23]. This package has a modular structure, which allows an easy addition of new physics modules. Within this thesis a new Plug-In for the hadronic interactions of CR protons with the ambient gas was developed (see section 3.2). In this module a set of pre-calculated probability distribution functions (PDFs) for the secondaries is used. Those PDFs are obtained from different single-differential cross section models [71, 72, 75, 96, 97]. The sampling of secondary particles from these tabulated distributions is much faster than the typical Monte-Carlo sampling approach. The Plug-In injects the produced secondaries directly into the simulation and allows to follow the propagation and further interactions. This is of special interest in those astrophysical scenarios where absorption is important and the very-high-energy secondaries induce a cascade. The propagation of the secondary particles can also affect the spatial distribution of the non-thermal emission. This approach has been applied to the Central Molecular Zone (CMZ) of the Milky Way and the CR interactions within the Solar atmosphere.

From the computational point of view, a direct tracing of produced gamma-rays is not reasonable in the context of the Galactic diffuse emission. The Milky Way is optically thin ($\tau \ll 1$) and therefore the total number of interactions per simulated primary is low. This implies immense computation power for particles which are not used in the end. An alternative approach is the calculation of the CR distribution within the Galaxy as a first step and afterwards a calculation of the total gamma-ray emission for a given energy and a line-of-sight from the Earth. In this approach all simulated primaries can be used.

Can we use diffuse gamma-ray observations to constrain the sources of CRs?

The origin of the CRs is a longstanding open question in astroparticle physics. It is assumed that the acceleration process is connected to the emission of gamma-ray sources, where the CRs interact either in the acceleration site itself or in a close-by molecular cloud. In addition to the localized gamma-ray emission from this source regions the large-scale diffuse emission from the CMZ can be used to constrain the CR source within this region. In this analysis the emission from point sources, which are observed in VHE gamma rays, and a global 'sea' of Galactic CRs have been evaluated. Distinguishing those sources requires spatially resolved observations and is not possible from the spectral energy distribution alone. The observations of the CMZ indicate point sources as the origin of the CRs leading to the gamma-ray emission.

This general concept of source identification can be applied to other astrophysical systems and different source assumptions, but the discrimination power is best for strong differences in the source distributions. Also a good resolution of the gamma-ray emission and a clear discrimination of point sources and astrophysical foreground is needed.

Which information of the CR transport properties, like the diffusion coefficient, its energy scaling or the anisotropy, can be inferred from the diffuse gamma-ray observations?

The quantities of the diffusion tensor have been investigated in the context of the CMZ and the Galactic diffuse emission. In both cases, the anisotropy parametrized by the ratio between the perpendicular and the parallel diffusion coefficient $\epsilon = \kappa_\perp / \kappa_\parallel$ has been taken into account.

In the case of the CMZ, the energy scaling is used from the quasi-linear theory in a *Kolmogorov*-like turbulence, with a normalization for the typical Galactic average. The comparison of the spatial gamma-ray distribution with the observations points towards nearly isotropic diffusion ($\epsilon \approx 1$), which is reasonable for a highly turbulent medium. A dedicated test for the energy scaling of the diffusion is not possible in this context as it is degenerated with the spectral index of the source spectrum. Under the assumption of a $\kappa \sim E^{1/3}$ energy scaling, the CR sources need an injection index $\alpha \approx 2.0$ as it is expected from diffusive shock acceleration. The case of *Kraichnan*-like turbulence, where the diffusion coefficient scales with $\kappa \sim E^{1/2}$, a harder injection slope would be required.

For the CRs within the Milky Way, the (parallel) diffusion coefficient $\kappa_\parallel$ is estimated from CR spectrum measured at Earth. In a first step a one-dimensional model including the excitation of waves by gradients in the CR distribution and their diffusion in k-space is applied. This model is fitted to CR data and the resulting diffusion coefficient from this model is approximated for the usage in a realistic three-dimensional model. In the 3D case the additional free parameter of the anisotropy ϵ is added. From the escape time of the CRs one can directly deduce the impact this parameter has on the total CR density. While the resulting skymaps show systematic differences which can be probed by all sky gamma-ray observations, a

comparison to real observations is left for future work as well as the estimation of the gamma-ray SED which should have imprints from the energy scaling of the diffusion coefficient.

What is the influence of the environment (plasma density, magnetic field configuration, etc.) in which the CRs propagate on the gamma-ray signatures? Is it possible to constrain the environment from the gamma-ray observations?

The production of gamma-rays in hadronic interactions strongly depends on the distribution of the target plasma. On Galactic scales the target distribution changes on much shorter length-scales than the CR distribution. Therefore, the atomic and molecular hydrogen distribution is the main driver of local structures within the Galactic diffuse emission. Nevertheless, the CR transport and subsequently the magnetic field configuration impacts the large-scale distribution of the gamma-ray sky. The estimations of the CR escape times show clear hints, that the CR distribution will be different, when the same anisotropy of the diffusion tensor is assumed. This effect will vanish in the case of isotropic diffusion, as there is no preferred direction, and be maximal in the case of purely parallel diffusion. Differences from the underlying Galactic magnetic field (GMF) configuration can be estimated on the same basis like the differences from the anisotropy itself. Future investigations will require more computational power and are expected to show the differences from the GMF and open a new window to constrain it.

The CRs within our heliosphere, which travel to the atmosphere of the Sun and potentially undergo interactions there, carry information about environment they passed. Observations of the seasonal variation in the gamma-ray emission from the Sun indicate changes in the environment like changes in the target distribution or a changed transport within the magnetic field of the Sun. The estimated location of this emission on the solar surface shows a clear impact from the magnetic field configuration. At the moment the spatial scale of these structures is much smaller than the resolution of current generation instruments like Fermi-LAT or HAWC, but future missions might improve on this and a direct probing of the field structure with gamma rays might become possible. Nevertheless, a detailed modeling of the transport in the Solar atmosphere will help to identify the changes in the SED which are induced by temporal variations in the environment.

All in all it has been demonstrated in this thesis, that a detailed modeling of gamma-ray signatures is valuable tool to infer information about various astrophysical systems.

References

[1] M. G. Aartsen, R. Abbasi, M. Ackermann, et al., "Measurements of the time-dependent cosmic-ray Sun shadow with seven years of IceCube data: Comparison with the Solar cycle and magnetic field models", Phys. Rev. D **103**, 042005 (2021).

[2] M. G. Aartsen, M. Ackermann, J. Adams, et al., "Cosmic ray spectrum and composition from PeV to EeV using 3 years of data from IceTop and IceCube", Phys. Rev. D **100**, 082002 (2019).

[3] R. Abbasi, M. Ackermann, J. Adams, et al., "Search for Extended Sources of Neutrino Emission in the Galactic Plane with IceCube", The Astrophysical Journal **956**, 20 (2023).

[4] R. Abbasi, M. Ackermann, J. Adams, et al., "Observation of high-energy neutrinos from the Galactic plane", Sci **380**, 1338–1343 (2023).

[5] H. Abdalla, A. Abramowski, F. Aharonian, et al., "Characterising the VHE diffuse emission in the central 200 parsecs of our Galaxy with H.E.S.S.", Astronomy & Astrophysics **612**, A9 (2018).

[6] H. Abdalla, A. Abramowski, F. Aharonian, et al., "The H.E.S.S. Galactic plane survey", Astronomy & Astrophysics **612**, A1 (2018).

[7] A. A. Abdo, M. Ackermann, M. Ajello, et al., "Fermi Large Area Telescope Observations of Two Gamma-Ray Emission Components from the Quiescent Sun", The Astrophysical Journal **734**, 116 (2011).

[8] A. Abramowski, F. Aharonian, F. A. Benkhali, et al., "Acceleration of petaelectronvolt protons in the Galactic Centre", Nature 2016 531:7595 **531**, 476 (2016).

[9] V. A. Acciari, S. Ansoldi, L. A. Antonelli, et al., "MAGIC observations of the diffuse γ-ray emission in the vicinity of the Galactic Center", Astronomy & Astrophysics **642**, A190 (2020).

[10] M. Ackermann, M. Ajello, A. Albert, et al., "High-energy Gamma-Ray Emission from Solar Flares: Summary of Fermi Large Area Telescope Detections and Analysis of Two M-class Flares", Astrophys. J. **787**, 15 (2014).

[11] M. Ackermann, M. Ajello, A. Albert, et al., "The Fermi Galactic Center GeV Excess and Implications for Dark Matter", The Astrophysical Journal **840**, 43 (2017).

[12] R. Adam, P. A. Ade, M. I. Alves, et al., "Planck intermediate results - XLII. Large-scale Galactic magnetic fields", Astronomy & Astrophysics **596**, A103 (2016).

[13] C. B. Adams, W. Benbow, A. Brill, et al., "VERITAS Observations of the Galactic Center Region at Multi-TeV Gamma-Ray Energies", The Astrophysical Journal **913**, 115 (2021).

[14] O. Adriani, Y. Akaike, K. Asano, et al., "Observation of Spectral Structures in the Flux of Cosmic-Ray Protons from 50 GeV to 60 TeV with the Calorimetric Electron Telescope on the International Space Station", Physical Review Letters **129**, 101102 (2022).

[15] O. Adriani, G. C. Barbarino, G. A. Bazilevskaya, et al., "Time Dependence of the Proton Flux Measured by PAMELA during the 2006 July-2009 December Solar Minimum", The Astrophysical Journal **765**, 91 (2013).

[16] M. Aguilar, L. Ali Cavasonza, B. Alpat, et al., "Antiproton Flux, Antiproton-to-Proton Flux Ratio, and Properties of Elementary Particle Fluxes in Primary Cosmic Rays Measured with the Alpha Magnetic Spectrometer on the International Space Station", Physical Review Letters **117**, 091103 (2016).

[17] F. Aharonian, A. G. Akhperjanian, G. Anton, et al., "Spectrum and variability of the Galactic center VHE γ-ray source HESS J1745–290", Astronomy & Astrophysics **503**, 817–825 (2009).

[18] A. Albert, R. Alfaro, C. Alvarez, et al., "Discovery of Gamma Rays from the Quiescent Sun with HAWC", Physical Review Letters **131**, `10.1103/PhysRevLett.131.051201` (2023).

[19] A. Albert, R. Alfaro, C. Alvarez, et al., "Observation of the Galactic Center PeVatron beyond 100 TeV with HAWC", The Astrophysical Journal Letters **973**, L34 (2024).

[20] J. Allison, K. Amako, J. Apostolakis, et al., "Geant4 developments and applications", IEEE Transactions on Nuclear Science **53**, 270–278 (2006).

[21] R. Aloisio and P. Blasi, "Propagation of galactic cosmic rays in the presence of self-generated turbulence", Journal of Cosmology and Astroparticle Physics **2013**, 001 (2013).

[22] M. D. Altschuler and G. Newkirk, "Magnetic Fields and the Structure of the Solar Corona. I: Methods of Calculating Coronal Fields", Solar Physics **9**, 131–149 (1969).

[23] R. Alves Batista, J. Becker Tjus, J. Dörner, et al., "CRPropa 3.2 – an advanced framework for high-energy particle propagation in extragalactic and galactic spaces", Journal of Cosmology and Astroparticle Physics **9**, 035 (2022).

[24] R. Alves Batista, A. Dundovic, M. Erdmann, et al., "CRPropa 3—a public astrophysical simulation framework for propagating extraterrestrial ultra-high energy particles", Journal of Cosmology and Astroparticle Physics **05**, 038 (2016).

[25] M. Amenomori, X. J. Bi, D. Chen, et al., "Probe of the solar magnetic field using the "cosmic-ray shadow" of the sun", Phys. Rev. Lett. **111**, 011101 (2013).

[26] Q. An, R. Asfandiyarov, P. Azzarello, et al., "Measurement of the cosmic ray proton spectrum from 40 GeV to 100 TeV with the DAMPE satellite", Science Advances **5**, eaax3793 (2019).

[27]T. Antoni, W. D. Apel, A. F. Badea, et al., "KASCADE measurements of energy spectra for elemental groups of cosmic rays: Results and open problems", Astroparticle Physics **24**, 1–25 (2005).

[28]L. Armillotta, E. C. Ostriker, and Y.-F. Jiang, "Cosmic-Ray Transport in Varying Galactic Environments", The Astrophysical Journal **929**, 170 (2022).

[29]W. B. Atwood, A. A. Abdo, M. Ackermann, et al., "The Large Area Telescope on the Fermi Gamma-Ray Space Telescope Mission", The Astrophysical Journal **697**, 1071–1102 (2009).

[30]E. H. Avrett and R. Loeser, "Models of the Solar Chromosphere and Transition Region from SUMER and HRTS Observations: Formation of the Extreme-Ultraviolet Spectrum of Hydrogen, Carbon, and Oxygen", The Astrophysical Journal Supplement Series **175**, 229–276 (2008).

[31]M. Banaszkiewicz, W. I. Axford, and J. F. Mckenzie, "An analytic solar magnetic field model", Astronomy & Astrophysics **337**, 940–944 (1998).

[32]R. Beck, "Magnetic fields in spiral galaxies", Astronomy and Astrophysics Review **24**, 1–57 (2016).

[33]J. Becker Tjus, P. Desiati, N. Döpper, et al., "Cosmic-ray propagation around the Sun: investigating the influence of the solar magnetic field on the cosmic-ray Sun shadow", Astronomy & Astrophysics **633**, A83 (2020).

[34]J. Becker Tjus and L. Merten, "Closing in on the origin of Galactic cosmic rays using multimessenger information", Physics Reports **872**, 1–98 (2020).

[35]V. S. Berezinskii, S. V. Bulanov, V. A. Dogiel, et al., *Astrophysics of Cosmic Rays*, edited by V. L. Ginzburg (Elsevier Science Publishers B. V., Amsterdam: North-Holland, 1990).

[36]H. Bethe, "Quantenmechanik der ein- und zwei-elektronenprobleme", in *Quantentheorie*, edited by H. Bethe, F. Hund, N. F. Mott, et al. (Springer Berlin Heidelberg, Berlin, Heidelberg, 1933), pp. 273–560.

[37]P. Blasi and E. Amato, "Diffusive propagation of cosmic rays from supernova remnants in the Galaxy. I: spectrum and chemical composition", Journal of Cosmology and Astroparticle Physics **2012**, 010–010 (2012).

[38]P. Blasi, E. Amato, and P. D. Serpico, "Spectral Breaks as a Signature of Cosmic Ray Induced Turbulence in the Galaxy", Physical Review Letters **109**, 061101 (2012).

[39]G. R. Blumenthal and R. J. Gould, "Bremsstrahlung, Synchrotron Radiation, and Compton Scattering of High-Energy Electrons Traversing Dilute Gases", Review of Modern Physics **42** (1970).

[40]R. Bordoloi, A. J. Fox, F. J. Lockman, et al., "Mapping the Nuclear Outflow of the Milky Way: Studying the Kinematics and Spatial Extent of the Northern Fermi Bubble", The Astrophysical Journal **834**, 191 (2017).

[41]J. Boris, "Relativistic plasma simulation", in Proceedings of the Conference on Numerical Simulation of Plasmas (4th), held at the NAVAL Research Laboratory, Washington, D. C. (1970), p. 3.

[42] Z. Cao, F. Aharonian, Q. An, et al., "Measurement of Ultra-High-Energy Diffuse Gamma-Ray Emission of the Galactic Plane from 10 TeV to 1 PeV with LHAASO-KM2A", Physical Review Letters **131**, 151001 (2023).

[43] J. R. Cash and A. H. Karp, "A variable order Runge-Kutta method for initial value problems with rapidly varying right-hand sides", ACM Transactions on Mathematical Software (TOMS) **16**, 201–222 (1990).

[44] G. H. Choi, E. S. Seo, S. Aggarwal, et al., "Measurement of High-energy Cosmic-Ray Proton Spectrum from the ISS-CREAM Experiment", The Astrophysical Journal **940**, 107 (2022).

[45] A. C. Cummings, E. C. Stone, B. C. Heikkila, et al., "Galactic Cosmic Rays in the Local Interstellar Medium: Voyager 1 Observations and Model Results", The Astrophysical Journal **831**, 18 (2016).

[46] T. Daylan, D. P. Finkbeiner, D. Hooper, et al., "The characterization of the gamma-ray signal from the central Milky Way: A case for annihilating dark matter", Physics of the Dark Universe **12**, 1–23 (2016).

[47] P. Desiati and A. Lazarian, "Anisotropy of TeV Cosmic Rays and Outer Heliospheric Boundaries", The Astrophysical Journal **762**, 44 (2013).

[48] J. Dörner, J. Becker Tjus, P. S. Blomenkamp, et al., "Impact of Anisotropic Cosmic-Ray Transport on the Gamma-Ray Signatures in the Galactic Center", The Astrophysical Journal **965**, 180 (2024).

[49] J. Dörner, L. Morejon, K.-H. Kampert, et al., *Uncertainties in astrophysical gamma-ray and neutrino fluxes from proton-proton cross-sections in the gev to pev range*, 2025.

[50] A. Dundovic, C. Evoli, D. Gaggero, et al., "Simulating the Galactic multi-messenger emissions with HERMES", Astronomy & Astrophysics **653**, A18 (2021).

[51] B. Eichmann and M. Kachelrieß, "Impact of the finite life-time of UHECR sources", Journal of Cosmology and Astroparticle Physics **2023**, 053 (2023).

[52] C. Evoli, D. Gaggero, A. Vittino, et al., "Cosmic-ray propagation with DRAGON2: I. numerical solver and astrophysical ingredients", Journal of Cosmology and Astroparticle Physics **2017**, 015–015 (2017).

[53] K. Ferriere, "Global Model of the Interstellar Medium in our Galaxy with New Constraints on the Hot Gas Component", The Astrophysical Journal **497**, 759–776 (1998).

[54] K. Ferriere, W. Gillard, and P. Jean, "Spatial distribution of interstellar gas in the innermost 3 kpc of our Galaxy", Astronomy and Astrophysics **467**, 611–627 (2007).

[55] K. Ferrière, "Interstellar gas within 10 pc of Sagittarius A*", Astronomy & Astrophysics **540**, A50 (2012).

[56] K. Ferrière and P. Terral, "Analytical models of X-shape magnetic fields in galactic halos", Astronomy and Astrophysics **561**, A100 (2014).

[57] R. S. Fletcher, T. K. Gaisser, P. Lipari, et al., "sibyll: An event generator for simulation of high energy cosmic ray cascades", Phys. Rev. D **50**, 5710–5731 (1994).

[58] D. Foreman-Mackey, D. W. Hogg, D. Lang, et al., "<tt>emcee</tt>: the mcmc hammer", Publications of the Astronomical Society of the Pacific **125**, 306–312 (2013).

[59] L. J. Gleeson and W. I. Axford, "An analytic model illustrating the effects of rotation on a magnetosphere containing low-energy plasma", J. Geophys. Res. **81**, 3403 (1976).

[60] L. Goodenough and D. Hooper, "Possible Evidence For Dark Matter Annihilation In The Inner Milky Way From The Fermi Gamma Ray Space Telescope", arXiv **0910.2998** (2009).

[61] K. M. Gorski, E. Hivon, A. J. Banday, et al., "HEALPix: A Framework for High-Resolution Discretization and Fast Analysis of Data Distributed on the Sphere", The Astrophysical Journal **622**, 759–771 (2005).

[62] M. Guenduez, J. Becker Tjus, K. Ferrière, et al., "A novel analytical model of the magnetic field configuration in the Galactic center", Astronomy & Astrophysics **644**, A71 (2020).

[63] S. Hackstein, F. Vazza, M. Brüggen, et al., "Simulations of ultra-high energy cosmic rays in the local Universe and the origin of cosmic magnetic fields", MNRAS **475**, 2519–2529 (2018).

[64] C. R. Harris, K. J. Millman, S. J. van der Walt, et al., "Array programming with NumPy", Nature **585**, 357–362 (2020).

[65] J. D. Henshaw, A. T. Barnes, C. Battersby, et al., "Star Formation in the Central Molecular Zone of the Milky Way", Protostarts and Planets VII, ASP Conference Series **534** (2023).

[66] D. Hooper and K. Plant, "Leptonic Model for Neutrino Emission from Active Galactic Nuclei", Physical Review Letters **131**, 231001 (2023).

[67] J. D. Hunter, "Matplotlib: a 2d graphics environment", Computing in Science & Engineering **9**, 90–95 (2007).

[68] A. Hutchinson, S. Dalla, T. Laitinen, et al., "Energetic proton back-precipitation onto the solar atmosphere in relation to long-duration gamma-ray flares", Astronomy & Astrophysics **658**, A23 (2022).

[69] R. Jansson and G. R. Farrar, "A new model of the galactic magnetic field", Astrophysical Journal **757**, 14 (2012).

[70] M. Jin, V. Petrosian, W. Liu, et al., "Probing the Puzzle of Behind-the-limb γ-Ray Flares: Data-driven Simulations of Magnetic Connectivity and CME-driven Shock Evolution", The Astrophysical Journal **867**, 122 (2018).

[71] M. Kachelrieß, I. V. Moskalenko, and S. Ostapchenko, "AAfrag: Interpolation routines for Monte Carlo results on secondary production in proton–proton, proton–nucleus and nucleus–nucleus interactions", Computer Physics Communications **245**, `10.1016/J.CPC.2019.08.001` (2019).

[72]E. Kafexhiu, F. Aharonian, A. M. Taylor, et al., "Parametrization of gamma-ray production cross sections for pp interactions in a broad proton energy range from the kinematic threshold to PeV energies", Physical Review D **90**, 123014 (2014).

[73]T. Kamae, N. Karlsson, T. Mizuno, et al., "Parameterization of γ, e$\pm$, and Neutrino Spectra Production by p-p Interaction in Astronomical Environments", The Astrophysical Journal **647**, 692–708 (2006).

[74]K.-H. Kampert, J. Kulbartz, L. Maccione, et al., "CRPropa 2.0 – A public framework for propagating high energy nuclei, secondary gamma rays and neutrinos", Astroparticle Physics **42**, 41–51 (2013).

[75]S. R. Kelner, F. A. Aharonian, and V. V. Bugayov, "Energy spectra of gamma rays, electrons, and neutrinos produced at proton-proton interactions in the very high energy regime", Physical Review D **74**, 034018 (2006).

[76]R. Kissmann, "PICARD: A novel code for the Galactic Cosmic Ray propagation problem", Astroparticle Physics **55**, 37–50 (2014).

[77]J. Kleimann, T. Schorlepp, L. Merten, et al., "Solenoidal Improvements for the JF12 Galactic Magnetic Field Model", The Astrophysical Journal **877**, 76 (2019).

[78]M. Kline, *Calculus an intuitive and physical approach*, eng, 2. ed. (Wiley, New York, 1977).

[79]A. Kolmogorov, "The Local Structure of Turbulence in Incompressible Viscous Fluid for Very Large Reynolds' Numbers", Doklady Akademiia Nauk SSSR, vol.30, p.301-305 **30**, 301 (1941).

[80]E. P. Kontar, X. Chen, N. Chrysaphi, et al., "Anisotropic Radio-wave Scattering and the Interpretation of Solar Radio Emission Observations", The Astrophysical Journal **884**, 122 (2019).

[81]R. H. Kraichnan, "Inertial-Range Spectrum of Hydromagnetic Turbulence", The Physics of Fluids **8**, 1385–1387 (1965).

[82]S. Krakau and R. Schlickeiser, "Pion Production Momentum Loss of Cosmic Ray Hadrons", The Astrophysical Journal **802**, 114 (2015).

[83]C. E. Leith, "Diffusion approximation to inertial energy transfer in isotropic turbulence", The Physics of Fluids **10**, 1409–1416 (1967).

[84]J.-T. Li, J. F. Beacom, S. Griffith, et al., "Small-scale Magnetic Fields Are Critical to Shaping Solar Gamma-Ray Emission", The Astrophysical Journal **961**, 167 (2024).

[85]T. Linden, J. F. Beacom, A. H. G. Peter, et al., "First observations of solar disk gamma rays over a full solar cycle", Phys. Rev. D **105**, 063013 (2022).

[86]T. Linden, B. Zhou, J. F. Beacom, et al., "Evidence for a New Component of High-Energy Solar Gamma-Ray Production", Physical Review Letters **121**, 131103 (2018).

[87]W. McKinney, "Data Structures for Statistical Computing in Python", in Proceedings of the 9th Python in Science Conference, edited by S. van der Walt and J. Millman (2010), pp. 56–61.

[88] L. Merten, J. Becker Tjus, H. Fichtner, et al., "CRPropa 3.1—a low energy extension based on stochastic differential equations", Journal of Cosmology and Astroparticle Physics **2017**, 046 (2017).

[89] P. Mertsch and V. H. Phan, "Bayesian inference of three-dimensional gas maps: II. Galactic HI", Astronomy and Astrophysics **671**, A54 (2023).

[90] P. Mertsch and A. Vittino, "Bayesian inference of three-dimensional gas maps: I. Galactic CO", Astronomy & Astrophysics **655**, A64 (2021).

[91] J. A. Miller and D. A. Roberts, "Stochastic Proton Acceleration by Cascading Alfven Waves in Impulsive Solar Flares", The Astrophysical Journal **452**, 912 (1995).

[92] C. Muena, M. Riquelme, A. Reisenegger, et al., "HESS J1745290 spectrum explained by a transition in the diffusion regime of PeV cosmic rays in the Sgr A* accretion flow", (2024).

[93] H. Nakanishi and Y. Sofue, "Three-Dimensional Distribution of the ISM in the Milky Way Galaxy: I. The HI Disk", Publ. Astron. Soc. Japan **55**, 191–202 (2003).

[94] H. Nakanishi and Y. Sofue, "Three-Dimensional Distribution of the ISM in the Milky Way Galaxy: II. The Molecular Gas Disk", Publ. Astron. Soc. Japan **58**, 847–860 (2006).

[95] E. Orlando and A. W. Strong, "Gamma-ray emission from the solar halo and disk: a study with EGRET data", Astronomy & Astrophysics **480**, 847–857 (2008).

[96] L. Orusa, M. Di Mauro, F. Donato, et al., "New determination of the production cross section for secondary positrons and electrons in the Galaxy", Physical Review D **105**, 123021 (2022).

[97] L. Orusa, M. Di Mauro, F. Donato, et al., "New determination of the production cross section for γ rays in the Galaxy", Physical Review D **107**, 083031 (2023).

[98] S. Ostapchenko, "Monte Carlo treatment of hadronic interactions in enhanced Pomeron scheme: QGSJET-II model", Phys. Rev. D **83**, 014018 (2011).

[99] M. Padovani, D. Galli, and A. E. Glassgold, "Cosmic-ray ionization of molecular clouds", Astronomy & Astrophysics **501**, 619–631 (2009).

[100] F. Pérez and B. E. Granger, "IPython: a system for interactive scientific computing", Computing in Science and Engineering **9**, 21–29 (2007).

[101] N. V. Pogorelov, H. Fichtner, A. Czechowski, et al., "Heliosheath Processes and the Structure of the Heliopause: Modeling Energetic Particles, Cosmic Rays, and Magnetic Fields", Space Sci. Rev. **212**, 193–248 (2017).

[102] M. Pohl, P. Englmaier, and N. Bissantz, "3D Distribution of Molecular Gas in the Barred Milky Way", The Astrophysical Journal **677**, 283–291 (2008).

[103] T. A. Porter, G. Jóhannesson, and I. V. Moskalenko, "The GALPROP Cosmic-ray Propagation and Nonthermal Emissions Framework: Release v57", The Astrophysical Journal Supplement Series **262**, 30 (2022).

[104] P. Reichherzer, J. Becker Tjus, E. G. Zweibel, et al., "Anisotropic cosmic ray diffusion in isotropic Kolmogorov turbulence", Monthly Notices of the Royal Astronomical Society **514**, 2658–2666 (2022).

[105] M. Rocklin, "Dask: parallel computation with blocked algorithms and task scheduling", in Proceedings of the 14th python in science conference, edited by K. Huff and J. Bergstra (2015), pp. 130–136.

[106] A. Roy, J. C. Joshi, M. Cardillo, et al., "Interpreting the GeV-TeV gamma-ray spectra of local giant molecular clouds using GEANT4 simulation", Journal of Cosmology and Astroparticle Physics **2023**, 047 (2023).

[107] D. Sakai, T. Oyama, H. Kobayashi, et al., "Astrometric observations of water maser sources toward the Galactic Center with VLBI", in Cosmic masers: proper motion toward the next-generation large projects, Vol. 380, edited by T. Hirota, H. Imai, K. Menten, et al. (Jan. 2024), pp. 122–124.

[108] D. Sakai, T. Oyama, T. Nagayama, et al., "Water maser distributions and their internal motions in the Sagittarius B2 complex", PASJ **75**, 937–950 (2023).

[109] M. L. Sampson, J. R. Beattie, M. R. Krumholz, et al., "Turbulent diffusion of streaming cosmic rays in compressible, partially ionized plasma", MNRAS **519**, 1503–1525 (2023).

[110] A. Scherer, J. Cuadra, and F. E. Bauer, "Galactic center gamma-ray production by cosmic rays from stellar winds and Sgr A East", Astronomy & Astrophysics **659**, A105 (2022).

[111] A. Scherer, J. Cuadra, and F. E. Bauer, "Modeling the Galactic center gamma-ray emission with more realistic cosmic-ray dynamics", Astronomy & Astrophysics **679**, A114 (2023).

[112] L. Schlegel, A. Frie, B. Eichmann, et al., "Interpolation of Turbulent Magnetic Fields and Its Consequences on Cosmic Ray Propagation", The Astrophysical Journal **889**, 123 (2020).

[113] R. Schlickeiser, *Cosmic Ray Astrophysics*, Astronomy and Astrophysics Library (Springer Berlin Heidelberg, Berlin, Heidelberg, 2002).

[114] D. Seckel, T. Stanev, and T. K. Gaisser, "Signatures of cosmic-ray interactions on the solar surface", Astrophys. J. **382**, 652–666 (1991).

[115] A. Shalchi, T. Škoda, R. C. Tautz, et al., "Analytical description of nonlinear cosmic ray scattering: Isotropic and quasilinear regimes of pitch-angle diffusion", Astronomy and Astrophysics **507**, 589–597 (2009).

[116] A. Shalchi, *Nonlinear Cosmic Ray Diffusion Theories*, Vol. 362, Astrophysics and Space Science Library July (Springer Berlin Heidelberg, Berlin, Heidelberg, 2009), pp. 1–23.

[117] T. Sjöstrand, S. Mrenna, and P. Skands, "A brief introduction to PYTHIA 8.1", Computer Physics Communications **178**, 852–867 (2008).

[118] J. Skilling, "Cosmic Rays in the Galaxy: Convection or Diffusion?", The Astrophysical Journal **170**, 265 (1971).

[119] E. C. Stone, A. C. Cummings, F. B. McDonald, et al., "Voyager 1 Observes Low-Energy Galactic Cosmic Rays in a Region Depleted of Heliospheric Ions", Science **341**, 150–153 (2013).

[120] E. C. Stone, A. C. Cummings, B. C. Heikkila, et al., "Cosmic ray measurements from Voyager 2 as it crossed into interstellar space", Nature Astronomy **3**, 1013–1018 (2019).

[121] A. W. Strong and I. V. Moskalenko, "Propagation of Cosmic-Ray Nucleons in the Galaxy", The Astrophysical Journal **509**, 212–228 (1998).

[122] Q.-W. Tang, K. C. Y. Ng, T. Linden, et al., "Unexpected dip in the solar gamma-ray spectrum", Phys. Rev. D **98**, 063019 (2018).

[123] The CTA Consortium, *Science with the Cherenkov Telescope Array* (WORLD SCIENTIFIC, 2019).

[124] T. Thomas, C. Pfrommer, and R. Pakmor, "Cosmic-ray-driven galactic winds: transport modes of cosmic rays and Alfvén-wave dark regions", MNRAS **521**, 3023–3042 (2023).

[125] M. Unger and G. R. Farrar, "The Coherent Magnetic Field of the Milky Way", The Astrophysical Journal **970**, 95 (2024).

[126] P. Virtanen, R. Gommers, T. E. Oliphant, et al., "SciPy 1.0: Fundamental Algorithms for Scientific Computing in Python", Nature Methods **17**, 261–272 (2020).

[127] M. L. Waskom, "Seaborn: statistical data visualization", Journal of Open Source Software **6**, 3021 (2021).

[128] R. L. Workman et al. (Particle Data Group), "Review of Particle Physics", PTEP **2022**, 083C01 (2022).

[129] P. Zeeman, "The Effect of Magnetisation on the Nature of Light Emitted by a Substance", Nature **55**, 347–347 (1897).

[130] M. Zhang, P. Zuo, and N. Pogorelov, "Heliospheric Influence on the Anisotropy of TeV Cosmic Rays", The Astrophysical Journal **790**, 5 (2014).

[131] Y. Zhou and W. H. Matthaeus, "Models of inertial range spectra of interplanetary magnetohydrodynamic turbulence", Journal of Geophysical Research: Space Physics **95**, 14881–14892 (1990).

[132] A. Zonca, L. Singer, D. Lenz, et al., "healpy: equal area pixelization and spherical harmonics transforms for data on the sphere in Python", The Journal of Open Source Software **4**, 1298 (2019).

Curriculum Vitae

Personal Information

First Name	Julien
Last Name	Dörner
Date of Birth	11 June 1995
Place of Birth	Hagen Stadtteil Hohenlimburg, Germany

Education

School (Abitur)	Kilian Grundschule Iserlohn-Letmathe (2001 - 2005)
	Gymnasium Letmathe der Stadt Iserlohn (2005 - 2013)
Bachelor of Science	Ruhr University Bochum (2013 - 2018)
	Implementierung von beobachtungsbasierten Gasverteilungen der Milchstraße in das Propagationsprogramm CRPropa
Master of Science	Ruhr University Bochum (2018 - 2021)
	Simulationen des Transports der kosmischen Strahlung: Theoretische Untersuchung des Gradientenproblems der kosmischen Strahlung
PhD student	Ruhr University Bochum (2021 - present)